THE UNIVERSITY OF MANITOBA

The *Chandra* and *RXTE* Study of the Galactic Microquasar SS 433 and the Surrounding Nebula W50

by

Alyssa M. Moldowan

A THESIS
SUBMITTED TO THE FACULTY OF GRADUATE STUDIES
IN PARTIAL FULFILLMENT OF THE REQUIREMENTS FOR THE
DEGREE OF MASTER'S OF SCIENCE

DEPARTMENT OF PHYSICS AND ASTRONOMY

WINNIPEG, MANITOBA

June, 2005

THE UNIVERSITY OF MANITOBA

FACULTY OF GRADUATE STUDIES

*****

COPYRIGHT PERMISSION

The *Chandra* and *RXTE* Study of the Galactic Microquasar SS 433 and the Surrounding Nebula W50

BY

Alyssa M. Moldowan

A Thesis/Practicum submitted to the Faculty of Graduate Studies of The University of Manitoba in partial fulfillment of the requirement of the degree

Of

Master of Science

To my parents, my brother and the rest of my family

"In my youth I regarded the universe as an open book,
printed in the language of equations,
whereas now it appears to me as a text written in invisible ink,
of which in our rare moments of grace we are able to decipher a small segment."
- Arthur Koestler

Acknowledgments

First and foremost, I would like to thank my supervisor, Dr. Samar Safi-Harb, for taking a chance on a struggling physics student. Without her confidence in my research abilities I would not be writing this thesis. She gave me the chance to prove to myself and others that I possibly could belong in the academic world, and for this I will always be grateful.

I am also continually in awe of her dedication and passion she shows for her research. Seeing her work through the night and spend tireless hours writing papers and proposals, doing data analysis and still have time to help her graduate students (and go to their concerts!) was a great motivation.

I would also like to thank all of my professors at the University of Calgary. Namely Dr. Dave Knudsen and Dr. Eric Donovan for raking us over the coals in thermodynamics and electromagnetism, Dr. David Fry for having all the time in the world to help with anything, and Dr. Jo-Anne Brown for making me see the light. Also, many thanks to Ian Cameron and Dr. Jayanne English for being there with advice on how to deal with having far to much to do, and no time to do it; and to Dr. Jason Fiege for his help with MATLAB and a new perspective for my research.

Special thanks goes out to all of my friends back home in Calgary who always thought I would be the academic star of our lives. It is their excitement and bewilderment that makes me realize that I am indeed living my dream. I would also like to thank my fellow students in both Calgary and Winnipeg who made my life bearable in those times of crisis. I will never forget the uncontrollable laughter, the tears and the incredibly interesting conversations.

Although this may seem silly, I want to thank my cats for their unconditional love and affection...even when I did not want it. I also want to send out thanks to my brother for always being interested in what I am doing and always knowing how to make me laugh. Even though we are further apart than ever, I feel that we have grown closer over the past two years.

Finally, I would like to give my deepest thanks and gratitude to my parents for giving me endless love, support and encouragement in any situation. I have no words to describe how deeply touched I am daily by their involvement in my life. I would not be the person I am today if it was not for them.

This project encompasses why I initially fell in love with astronomy years ago...the questions, the wonder, the romance, the frustration, and the beauty of nature. It is my great pleasure to be able to share this with my family, friends, and colleagues.

Abstract

The X-ray binary system SS 433/W50 has baffled astrophysicists since its discovery in 1979. W50 has been classified as a Galactic supernova remnant that harbors SS 433, an X-ray binary consisting of a compact object accreting matter from a companion star at a super-Eddington rate. The nature of the compact object is still under debate, but it is expelling relativistic jets that interact with W50, causing it to elongate along the jets axis and forming two X-ray lobes. This system has been studied in depth using *Chandra* (Moldowan et al., 2005), *ROSAT* and *ASCA* (Safi-Harb & Ögelman 1997), *RXTE* (Safi-Harb & Petre 1999, Safi-Harb & Kotani 2002, 2003), and at millimeter wavelengths (Durouchoux et al. 2000).

A 75 ksec *Chandra* observation of the western lobe of W50 is presented in this thesis. This region is of particular interest because it is rich with knots resulting from the interaction of a relativistic jet with a dense medium. The *Chandra* data provide the highest resolution X-ray image obtained to date. The spectroscopic results of this observation are presented and are targeted to 1) determine the nature of the X-ray emission and 2) correlate the X-ray emission with previous observations in the infrared and radio domains. It has been confirmed that at the site of interaction between the western jet and the interstellar gas the emission is non-thermal in nature. The helical pattern seen in radio is also observed with *Chandra*. No correlation was found between the X-ray and infrared emission.

In addition, data from both the *PCA* and *HEXTE* instruments on board *RXTE* is presented, and is used to complete the first spectral analysis of SS 433 up to X-ray energies of 70 keV. This analysis is targeted to 1) determine the hard X-ray emission

mechanism 2) study the variations of the spectral parameters as a function of the orbital phase of the binary system 3) correlate its hard X-ray flux with the radio activity, and 4) test the capabilities of the *HEXTE* instrument. The emission from SS 433 is well described by a bremsstrahlung model or a power-law model, with two Gaussian lines. The best fit model seems to depend on the orientation of the jets. It is found that temperature and flux are at a minimum when the compact object is being eclipsed, while Γ, the photon index, is at a maximum. After a radio flare, it is observed that the flux and temperature decrease while Γ increases (i.e. the spectrum softens). The *HEXTE* instrument proves useful in constraining model parameters and determining the best fit model.

The study of this system demonstrates the power of the *Chandra* observatory, in that its high resolution capabilities allows for the determination of the nature of the emission in the western lobe of W50, which had not yet been confirmed. *Chandra's* imaging capabilities also brought out the helical pattern that confirms the jet interaction at all scales. This study also proves the capability of the *HEXTE* on board *RXTE* to be quite useful in studying the energy range not covered between *Chandra* and *INTEGRAL* (a gamma-ray satellite). Finally, studying SS 433 and its interaction with the surrounding medium can lead to a better understanding on how its larger, more energetic cousin, the active galactic nuclei, evolve.

Table of Contents

List of Tables

List of Figures

Chapter 1

Introduction

Stephenson-Sanduleak 433 (SS 433, also known as V1343 Aquilae) is the first known example of a Galactic relativistic jet source (**microquasar**[1]), and thus the forerunner of modern microquasar astrophysics. In the 27 years since the discovery of the peculiar properties of SS 433 there have been over 250 publications that describe observations in all wavelengths and theoretical models that attempt to explain the nature of the compact object and the companion, the origin of the jets and how they interact with the surrounding medium. Other thesis studies on this system have recently been published by Kotani (1996), Safi-Harb (1997) and Vermeulen (1989). Kotani (1996) focused on a study of SS 433 with *ASCA*[2], while Safi-Harb (1997) did both a *ROSAT* study on SS 433, and a study on W50. Vermeulen (1989) focused on the radio studies of the SS 433 jets. There is no question that SS 433 and the nebula that surrounds it, W50, are associated, but the emission mechanisms for both SS 433 and W50, and the interactions between the jet and the surrounding medium, along with other properties of this system, still remain a mystery.

The project presented in this thesis is divided into two major parts: 1) the *Chandra* study of the western lobe of W50, and 2) the *RXTE* study of the **X-ray binary** SS 433. The main goal of both of these studies is to understand the X-ray emission mechanisms, and to use this information to derive the intrinsic properties of

[1] All words in bold are defined in the glossary in Appendix E

[2] All abbreviations used throughout this thesis are defined in Appendix D

the system (see Abstract). Chapter 2 introduces the multiple components that make up this system and gives an overview of previous studies in different wavelengths. Chapter 3 reviews the capabilities and data analyzing procedures of both *Chandra* and *RXTE*. Chapters 4 and 5 present the analysis and results for the western lobe of W50 and SS 433, respectively. Finally, Chapter 6 summarizes the results presented in these studies, and future observations.

Chapter 2

The SS 433 X-ray Binary System and W50 Nebula

SS 433 was first cataloged in an objective prism survey as one of many emission-line objects with very strong Hα in 1977 (Stephenson & Sanduleak, 1977). W50 was first cataloged in the 1950s. During a radio source survey conducted at the Cambridge 5 km radio telescope, W50 was observed along with a strong point source at the center of the shell. Unfortunately, the coordinates were recorded inaccurately, so the object could not be further observed.

The prominent radio emission as well as the X-ray emission from the star were independently discovered. It was not until 1978, that the first optical spectra of SS 433 were taken by David Clark and Paul Murdin using the Anglo-Australian Telescope (Clark & Murdin, 1978). They drew attention to the connection between the radio, optical and X-ray sources and the possible role of the extended surrounding nebula, W50.

These optical spectra revealed not only stationary, very strong, broad Balmer and He I emission lines, but there were also many prominent emission features at unfamiliar wavelengths. These have been found to be associated with Doppler shifted Balmer and He I lines (Liebert et al., 1979, Margon et al., 1979). Even more interesting is that one set is largely redshifted, while the other set is blueshifted. These features move smoothly back and forth on the spectrum on a period of $\sim$164 days. The variable Doppler shifts have an average magnitude of about 40,000 km/s (about 50,000 km/s maximum and 30,000 km/s minimum in the red and blueshifted fea-

tures, respectively), while the mean velocity of the sum of the red and blueshifted components remains constant at about 12,000 km/s.

Shortly after this discovery, both Fabian & Rees (1979) and Milgrom (1979) independently proposed collimated, oppositely ejected jets, traveling at relativistic speed, as a possible explanation of the simultaneous red and blueshifted features. These jets precess about a common axis with the 164 day period, varying their orientation toward us, therefore producing the observed Doppler velocity modulation. This solution is now widely accepted as the basis for understanding the nature of SS 433, and is known as *the kinematic model*, which is described in section 2.2.

Abell & Margon (1979) derived the velocity of the jets to be 0.26c, which corresponds to a Lorentz factor of

$$\gamma = \frac{1}{(1 - v^2/c^2)^{1/2}} = 1.035. \tag{2.1}$$

This time dilation redshift is present in the velocity data as a zero point, regardless of the phase of the jet axis. This explains the 12,000 km/s symmetry value for the Doppler shifts.

The kinematic model is a simple way to understand and predict the behavior of the jets, but it leaves many other aspects of the system unspecified. This includes the nature of the compact object and companion star, the distance to the system, the mechanisms that eject, collimate and precess the jets and create the Doppler shifted radiation, and the evolutionary sequence that led to the formation of this very peculiar object.

2.1 System Components

Margon (1984) gives an extensive review of SS 433/W50. Here, the major aspects of this system are summarized. SS 433 is located at α (J2000)[1] = $19^h11^m49.56^s$ and δ (J2000) = $+04^o58'57.6''$. The corresponding Galactic coordinates are $l = 39.69^o$ and b = -2.24^o. The distance to the system is still under debate, and has been derived to be anywhere between 2.4-5.5 kpc. However, for this thesis, a distance of 3 kpc is used (see section 2.1.6).

The SS 433 system consists of a compact object in a close binary orbit with a companion star, having a period of about 13 days. The mass donor feeds an enlarged accretion disk surrounding the compact object, which is accreting at the **super-Eddington limit**. A small portion of this inflow is expelled as oppositely aligned relativistic jets, traveling at 0.26c. These jets are precessing in a period of approximately 164 days, creating a cone of half-opening angle of about 20^o. This is observable in the extreme radial velocities of the moving sets of emission lines.

The jets are interacting with the W50 nebula, causing it to elongate along their axis. A shorter period of ~6 days has been observed, caused by the nodding motion, or wobble, of the accretion disk. Figure 2.1 depicts the components of the SS 433 system, while Figure 2.2 shows the elongated W50 nebula. In this section, the SS 433 and W50 components are generally described. For more in depth explanations, see the following sections detailing the kinematic and dynamic models, observations in multiple wavelengths and references therein.

[1]see Appendix E for definition of J2000 coordinates

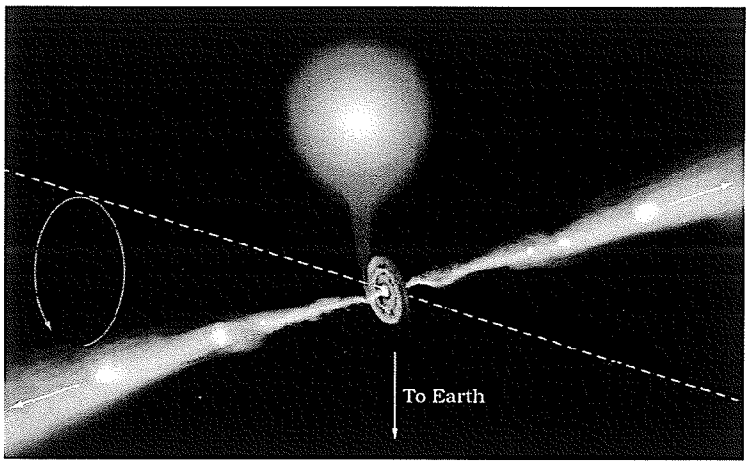

Figure 2.1: An artist's conception of the SS 433 X-ray binary system. Matter is accreted from the companion onto the compact object, creating a disk. The matter is heated to millions of degrees, and is expelled in the form of highly collimated jets, which precess around a fixed axis. Credit: CXC/M. Weiss (available from http://www.chandra.harvard.edu/photo/2002/0214/more.html).

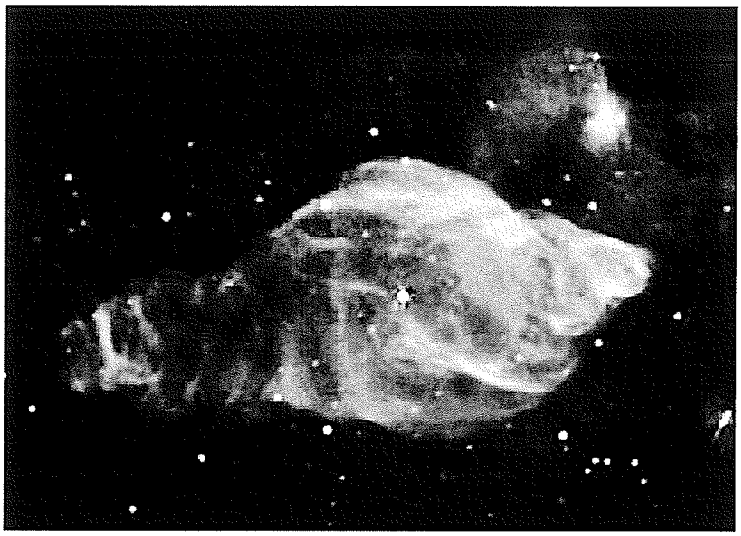

Figure 2.2: A radio image of the W50 nebula. The jets are aligned in the east/west direction, causing the nebula to elongate along their axis. The bright point source at the center of the nebula is SS 433. Credit: G. Dubner.

2.1.1 The Compact Object

The near relativistic of the jets, as well as the X-ray emission from the system, suggests the presence of a collapsed object (either a neutron star or black hole). The choice between which alternative is correct is still unclear, although recent studies by Gies et al. (2002) and H. Marshall (2005, private communication) point to a black hole. Traditional tests to distinguish between these objects include the detection of sustained periodicities (i.e. neutron star pulses), or a mass measurement for the compact object.

2.1.2 The Companion Star

It was Crampton et al. (1980) that first suggested that SS 433 is a binary system after observing the stationary lines in the spectrum (see section 2.3.2). The companion star is the mass donor, and is probably a **Roche-filling evolved star**. Unfortunately, its spectral signature has eluded detection, probably because the binary is embedded in an expanding thick disk that is fed by the wind from the super-Eddington accretion disk. The spectrum of the companion is crucial because, without it, the mass of the compact object is unknown.

2.1.3 The Jets

The kinetic luminosity of the jets, $L_J \sim 10^{39-40}$ erg/s (Margon, 1984; Brinkmann, Kotani & Kawai, 2002), quite possibly exceeds the radiative luminosity of any other star in the Galaxy. The two best predicted mechanisms to supply this demand are either rotation of or accretion onto a compact star. There are no observations to support a rapid rotation of the compact object, thus the accretion mechanism is

favoured in this scenario. In fact, the accretion must be super-Eddington because, unless the compact object is extremely massive (i.e. a mass of $\geq$7-70 $M_{\odot}$ is needed to get a luminosity of $\sim 10^{39-40}$ erg/s, see Appendix E), the Eddington limit must be exceeded to power the jets.

The narrow moving spectral lines of the system reveal a remarkably good collimation of the jets. Observational evidence of the phase difference between the 164 day cycle and the moving lines indicate that the jets are transverse to and follow the cyclically changing orientation of the disk. Since the disk provides a natural symmetry plane, it is reasonable to assume that it plays a large role in the collimation of the jets.

2.1.4 The Disk and Precession Mechanism

Observations by Anderson, Margon & Grandi (1983) indicate that the disk is remarkably thick, having a disk half-thickness to radius ratio of 2/3. This is supported by observations of a periodic 6.3 day nodding motion. The disk must be extremely viscous to rapidly transmit the nodding from the outside to the interior, where the jets originate and are seen to respond to the motion (Margon, 1984). The disk is also quite extended, with dimensions on the order of 10^{12} cm (comparable to the separation of the two stars).

Modeling the precession mechanism has been one of the major complications of this system. At first it was thought that it was due to the relativistic **Lense-Thirring effect** (the dragging of frames), which can now be ruled out because it requires a highly compact disk. The remaining possible mechanisms most often considered are classical, driven precession, where the normal companion exerts a

torque on the disk, and **slaved precession**, where a short residence time for matter in the disk permits it to follow the precessional motion of a misaligned companion.

2.1.5 W50

W50 (G39.7-2.0) is a very bright extended radio structure which has long been studied, and is generally classified as a **supernova remnant (SNR)**. Radio maps show a $2^o \times 1^o$ ellipsoidal shape, elongated in the east-west direction (refer to Figure 2.2). This corresponds to $\sim$100 pc $\times$ 50 pc, assuming a distance of 3 kpc to SS 433. It has a spherical central shape in the north-south direction, but is ellipsoidal in the east-west direction (known as wings or lobes). The eastern wing shows a clear helical pattern, which is thought to have risen from the precession of the SS 433 jets. The western lobe is smaller and brighter, thus appearing to interact with a more dense medium. SS 433 is remarkably centrally located in the elongated remnant, leading to the natural association between the two.

Optical maps of W50 show optical filaments at $\sim 30'$ east and west from SS 433, all of which lie well inside the eastern and western parts of W50, and within the precession cone of the SS 433 jets. This leads to the suggestion that they result from the propagation of shock waves into the pre-existing dense filaments of the SNR along the direction of the jets.

In X-rays, there are two bright diffuse lobes symmetrically displaced east and west of SS 433, and aligned along the axis of W50. Each lobe can be seen from $\sim 15'$-$40'$ from SS 433, with emission peaking at about $35'$. Many studies reveal a non-thermal nature for the lobes. The X-rays are interpreted as synchrotron radiation from the high energy electrons produced by the jet interacting with the interstellar medium

(ISM) (Safi-Harb & Petre, 1999, and references therein).

Different origins have been proposed to explain the nature and shape of the emission from W50. Begelman et al. (1980) characterized W50 as a 'beambag', interpreting the elongated shape and filled-in radio structure as evidence for continuing injection of magnetic fields and high-energy particles from the jets of a compact binary source. The large radio lobes to the east and west would have been blown out by the pressure of the SS 433 jets. Königl (1983), on the other hand, proposed that W50 is an expanding interstellar bubble driven by the stellar wind from the binary companion of SS 433, and that the dynamics of the expansion are controlled by the inertia of evaporated clouds in a three-phase ISM. In any case, it is clear that SS 433 has influenced the W50 remnant, because the energetics of its jets supply a considerable portion of the energy of W50.

There is another variable, unresolved point source embedded in W50, 30′ NE of SS 433. This second object, known to be 1910+052, is probably a chance superposition on the remnant. This is to be expected if observations go to faint flux levels. To confuse the radio picture even more, an H II region, S74, is superposed on the NW portion of W50. Optical studies show this is most definitely an unrelated foreground object. Also overlapping W50 is an extended and prominent molecular cloud that is also in the foreground.

2.1.6 Distance Determinations

As mentioned briefly above, there is a discrepancy in the derived distances to W50 and SS 433. Crampton et al. (1980) derive a lower limit on the distance to SS 433 by taking the distance of S74 (the faint H II region located about 1^{o} from the system)

to be 2.3 kpc. Then, using polarization measurements of the radio emission, they find that S74 must be in front of W50. So, if SS 433 and W50 are related, then the distance of SS 433 is > 2.3 kpc. They also note that the size of the W50 remnant suggests a distance d < 3.5 kpc. Other observations also show that the distance to SS 433 is most likely ~ 3 kpc (Dubner et al., 1998, and references therein).

Hjellming & Johnston (1981) derive the distance to SS 433 in a different manner: since they derived the speed of the jets to be 0.26c, and that the apparent motion of a few linearly polarized features in the jets is $3''.2$/yr, they can determine the distance to SS 433 to be 5.5 kpc.

The distance to W50 has also been derived using different techniques. Geldzahler et al. (1980), for instance, determine flux densities and **spectral index** values and use them with surface brightness-linear diameter (Σ - D) relations to estimate the mean linear diameter of W50 and its distance from the Sun. Using two different models (assuming W50 is elliptical or circular), they suggest that, if W50 obeys the Σ - D relation, the mean diameter should be 40-65 pc, and the distance must be 2-3 kpc.

Elston & Baum (1987) suggest that, if the W50 nebula were at 5.5 kpc, then its large size (shell radius = 50 pc) and its great distance from the Galactic plane (200 pc) would make it seem unlikely that it formed as a result of a supernova. On the other hand, if its distance is 3 kpc, this brings W50 closer to the Galactic plane and decreases the radius of the blast-wave shell to 30 pc. This size for the shell indicates an age of $\sim 10^5$ years, which is close to other age estimates (typically $\sim 10^4$ years). Dubner et al. (1998) are able to derive a distance of 3 kpc for W50, by determining the systemic velocity to be 42 km/s and using a circular rotation model

of the Galaxy.

In this thesis, studies of both SS 433 and W50 are performed, and therefore a consistent value for the distance must be used. Since all estimates of the distance to W50 agree to be $\sim$ 3 kpc, and most of the SS 433 distance determinations agree with this also, this value is chosen to use throughout this thesis.

2.2 The Kinematic and Dynamic Models

The spectrum of SS 433 is peculiar, in that it contains many prominent emission features at unfamiliar wavelengths. Three sets of hydrogen and helium emission lines appear: one is near zero radial velocity, and the other two show large and variable shifts to the blue and red. This phenomenon was later discovered to be caused by the Doppler effect, as multiple lines with constant redshifts, $z=\Delta\lambda/\lambda$, were identified in both the red and blue systems. To add to this complexity, these features change in wavelength and drift through the spectrum on a time scale of days as the velocity of the two systems changes smoothly. The change in wavelength is found to be periodic, and has a time scale of about 164 days.

To explain this strange system, both Fabian & Rees (1979) and Milgrom (1979) proposed what is know known as *the kinematic model.* Shortly after, Abell & Margon (1979) were able to confirm the model with observations. They predicted that the radiation with variable Doppler shift is emitted by hot matter ejected by the central object at high, but nearly constant, velocity in oppositely directed narrow streams (jets). As the matter reaches a critical distance from the central object ($\sim 4 \times 10^{14}$ cm; Gies et al. (2002)), it cools sufficiently to recombine and give rise to the

observed emission. The observed radial velocity variations are achieved by a periodic rotation of the jet axis, which is caused by precession. Abell & Margon (1979) also made the prediction that the moving emission line systems would cross, with the redshift system becoming blueshifted and vice versa. This was in fact observed shortly thereafter.

Abell & Margon (1979) assume that the beam axis rotates with angular velocity ω=$2\pi/164$ d (rad/day). Let the line-of-sight (LOS) lie along a unit vector $\hat{n}$, inclined at an angle i to the beam rotation axis. As the beam axis rotates, the jets of the flowing matter, orientated at an angle θ to the rotation axis, describe a conical motion about this axis, with a 164 day period (see Figure 2.3). Let the matter stream in

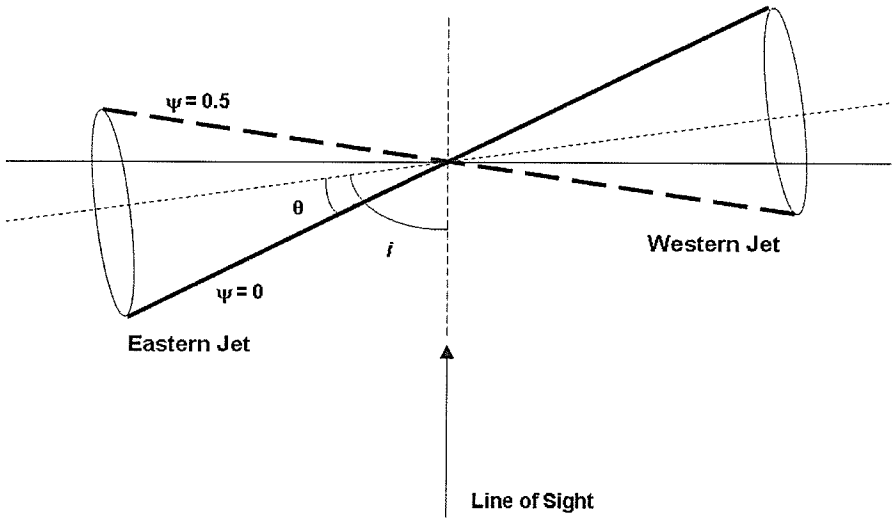

Figure 2.3: The precession geometry of the SS 433 jets. i is the inclination angle of the jet axis measured from the line of sight, while θ is the angle between the jet rotation axis and the jet. The precessional phase, ψ, is defined to be 0 when a maximum separation of the Doppler shifted lines occur (i.e. when eastern jet is toward us (thick line)). $\psi = 0.5$ when the western jet is toward us (thick dotted line).

opposite directions at speed v (in units where c=1) and let $\mathbf{V}$ be the velocity vector of the stream in the same hemisphere as $\hat{n}$. The direction cosine, l, of the angle between $\mathbf{V}$ and $\hat{n}$ is

$$\begin{aligned} l &= \frac{\mathbf{V}}{v} \cdot \hat{n} = sini\ sin\theta\ cos\omega t\ + cosi\ cos\theta \\ &= a\ cos\omega t + b \end{aligned} \tag{2.2}$$

The corresponding direction cosine, l', of the angle between the LOS and the opposite stream is

$$l' = -l = -a\ cos\omega t - b \tag{2.3}$$

From these it is noted that

$$a + b = cos|\theta - i| \tag{2.4}$$

and

$$b - a = cos(\theta + i) \tag{2.5}$$

The angles θ and i were first derived from these equations, but the solution was degenerate, that is $(i,\ \theta) = (78^o,\ 17^o)$ or $(17^o,\ 78^o)$. It was later found, using radio observations, that the inclination angle, i, is indeed 78^o (see below).

From the above equations, the Doppler shift is simply

$$1 + z = \gamma(1 + lv) \tag{2.6}$$

where l is the direction cosine in the frame of the observer, and $\gamma = (1 - v^2)^{-1/2}$ is the Lorentz Factor. Therefore the observed Doppler shifts of the streams are

$$(1 + z) = \gamma(1 + v\ a\ cos\omega t + vb) \tag{2.7}$$

$$(1 + z') = \gamma(1 - v\ a\ cos\omega t - vb). \tag{2.8}$$

This can be written as

$$(1+z) = \gamma(\pm v\ sin\theta\ sini\ cos(2\pi\psi) \pm vcos\theta\ cosi\ +1) \tag{2.9}$$

where

$$\psi = \frac{t - t_{0,p}}{P_p}. \tag{2.10}$$

In this case, ψ is the precessional phase (between 0 and 1), t is the time of observation, $t_{0,p}$ is the initial epoch of P_p, the precessional period (i.e. when $\psi = 0$, see Figure 2.3). Figure 2.4 shows the remarkable accuracy of the kinematic model. It provides a reasonable explanation for an observed velocity variation having an amplitude of 80,000 km/s.

The kinematic model leaves the cause of the jet precession unspecified. Simple rotation can be ruled out, as the inferred kinetic energy in the jets greatly exceeds the rotational energy stored in a compact object with such a long period. Most astronomers turn to precession as the more likely candidate. The need for a precession mechanism, as well as the requirement for a source of matter for accretion to create the jets, led Martin & Rees (1979) to propose a dynamical model involving mass transfer at a super-Eddington rate onto a spinning black hole in a very close binary system.

The high jet-velocity suggests that the acceleration and collimation occur in a **relativistically deep potential well**. The jets escape along the direction of least resistance, being aligned with the rotation axis of a gas cloud or disk close to the compact object. Thus, the precession of the black hole would assure the precession of the jet axis. This concept is also applicable to systems containing a rapidly spinning neutron star. Martin & Rees (1979) also note that the kinetic energy output from

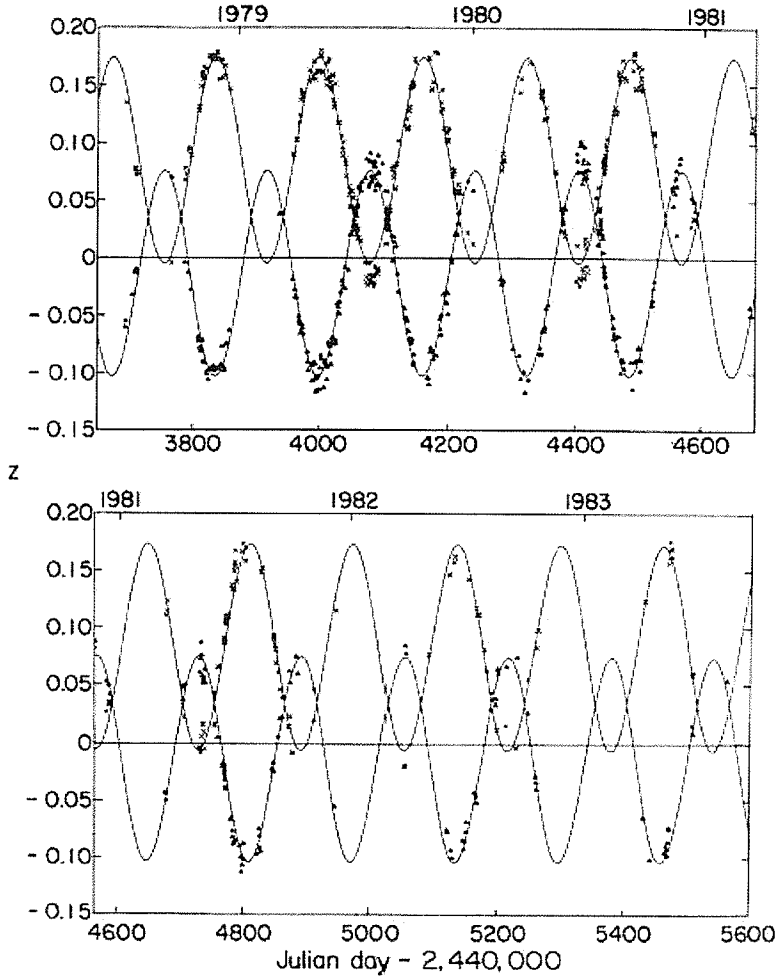

Figure 2.4: Doppler shifts of SS 433 on 450 nights in the period 1978-1983. The solid curve is a least-squares best fit to the kinematic model. The free parameters and their associated 1σ uncertainties for this fit are v/c=0.2601±0.0014, θ=19.80^o±0.18^o, i=78.82^o±0.11^o, $t_{0,p}$=JD 2,443,562.27±0.39, P_p=162.532±0.062 days (Figure 1 in Margon (1984)).

the jet, if maintained for 10^4 years, the derived age of W50 (Safi-Harb & Ögelman, 1997), would suffice to inflate and energize the entire W50 remnant.

From 52 spectroscopic observations, Crampton et al. (1980) measured the radial velocity in the stationary line spectrum of SS 433 which revealed a 13.1 day periodic variation of amplitude of 73 km/s. They also report that both emission and absorption lines show this same variation, and suggest this indicates that the variation is orbital. The appearance and width of the profiles were found to be similar to those originating in accretion disks of **cataclysmic variables**. Thus, it is reasonable to assume that the observed motion is that of a disk around a compact object. Crampton et al. (1980) also note the object would most probably be a neutron star, and suggest that, since the presence of the SNR implies an age of $<10^4$ years, which is much younger than other X-ray binaries, it may be that the extraordinary properties of SS 433 are the result of mass transfer onto a relatively young neutron star. This is also confirmed by observations by Margon et al. (1980).

The binary phase (values between 0 and 1) of the orbit can be found using

$$\phi = \frac{t - t_{0,b}}{P_b} \tag{2.11}$$

where $t_{0,b}$ is the initial epoch of P_b, the binary phase (i.e. when $\phi = 0$). For this thesis, $\phi = 0$ is defined when the compact object is being eclipsed by the companion star. Figure 2.5 shows the geometry of the binary system. Table 2.1 summarizes the best-fit parameters described by the ephemeris of Goranskii et al. (1998), which are adopted for this thesis (the value for $t_{0,p}$ has been modified by 8 cycles for data analysis purposes).

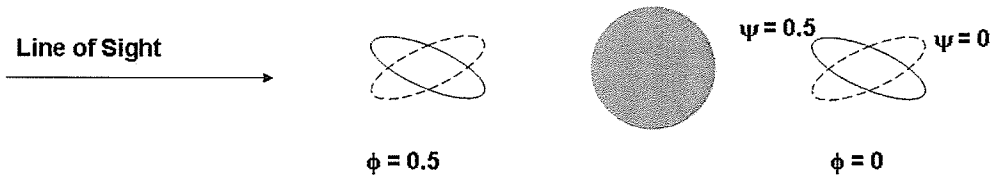

Figure 2.5: The geometry of the binary system. When the compact object is eclipsed by the companion star, the binary phase is $\phi = 0$. The solid and dotted ellipses represent when the western and eastern jet are pointed toward the observer, respectively (i.e. ψ =0.5 and 0).

Table 2.1: Best-fit parameters for the kinematic model used for this thesis using ephemeris of Goranskii et al. (1998).

Parameter	Value
P_p	162.15 days
P_b	13.082 days
$t_{0,p}$	2450160.92 JD
$t_{0,b}$	2450023.62 JD
v	0.2602c
θ	19.85^o
i	78.83^o

2.3 Optical & Infrared Observations

SS 433 is relatively bright in the optical region of the spectrum and can therefore be studied intensively with small instruments. A large fraction of the initial study of SS 433, which revealed the Doppler-shifted spectral lines, was in fact done with a 60 cm telescope. Thus, there have been far too numerous optical and infrared studies to mention them all. Instead, a discussion of the important discoveries of the basic properties of the system will be presented.

2.3.1 The Doppler Shifted Spectral Lines

The majority of the initial spectroscopic observations of the moving lines were reported by two groups. One based at Asiago, Italy, headed by A. Mammano and F. Ciatti, and the other based in the United States and headed by B. Margon and colleagues. The lines observed are Balmer and He I lines. However, with improved infrared instruments, Pashcen and Brackett shifted lines could also be observed. Later, with detailed X-ray observations, Fe XXV and Fe XXVI emission lines also became apparent. Interestingly, He II lines are very faint, giving a crucial constraint on the excitation of the beams.

From the Doppler shifts, the velocity of the emitting material can be derived to be 0.26c. This value is observed to be quite stable: random deviations from the kinematic model on short time scales (jitter) had been previously observed, but since they do not depend on the precessional phase, variation of velocity as an explanation for them can be excluded (Zwitter et al., 1989).

The individual lines are typically several thousand km/s wide at the base, and their profiles range from Gaussian to extremely complex. All H and He lines in the same jet have the same velocity structure at a given time. At times, the red and blueshifted features show mirror-image velocity structures. The precessional phase of the binary system can be determined by these shifts. These lines also show highly variable intensities, increasing and decreasing by a factor of 10 within 24 hours. The disappearance/reappearance episodes are synchronized in both emission line systems to high accuracy.

An extensive study of the spectral components of SS 433 is reported by Gies et al.

(2002). They present new optical and the first far-UV observation of the spectrum, and discuss the relationship of the spectral components to the properties of the binary system. Their study of the moving lines shows the jet components appear as distinct 'bullets' or 'blobs' of emission that appear suddenly at specific wavelengths and then decline on a timescale of a few days.

They also confirm the previously observed drastic intensity variations of the moving lines, reporting an out-of-eclipse variation of 0.60 mag over a precessional cycle. This indicates that changes in the disk orientation cause a modulation of 55% of the total flux, which is only possible if the disk is the dominant source of light in the optical. Even during a primary eclipse, the precessional light curve varies by 0.41 mag.

Gies et al. (2002) report that their derived radial velocity curve displays the well-known 162 day precessional variation, plus a shorter nodding motion with a 6.28 day period. This was first discussed by Katz et al. (1982) who show that a disk inclined to the orbital plane will experience gravitational torques caused by the orbiting star that will vary with the nodding period. Goranskii et al. (1998) also confirm this, reporting that during this period the optical star crosses the nodes in its orbit (the points of intersection of the binary's orbit with the plane that is perpendicular to the relativistic jets).

2.3.2 The Stationary Spectrum

The set of emission and absorption lines that do not have the large Doppler shifts are known as the stationary spectrum. These lines are superposed on an extremely red continuum, the slope of which is probably due to interstellar extinction. This

spectrum is dominated by intense, broad Balmer and He I lines. There are also He II, C III-N III and O I lines. Hα emission is responsible for the inclusion of SS 433 in the SS catalog. These lines do display slight Doppler shifts, which can be used to determine the ~13 day orbital period of the binary system (Crampton et al., 1980). The amplitude of the line variations corresponds to a projected velocity of 73 km/s (Zwitter et al., 1989). If this is adopted as the orbital motion of the compact object, then this implies a value of 0.52 $M_\odot$, as reported by Crampton et al. (1980), for the mass function

$$F = \frac{P_b K^3}{2\pi G sin^3 i} = \frac{M_x}{q(1+q)^2} = \frac{M_*}{(1+q)^2} \tag{2.12}$$

(Kotani, 1996) where M_* and M_x are the masses of the companion and compact stars, respectively, i is the inclination of the system, K is the projected velocity of the binary system, P_b is the binary period, and q is the mass fraction (q = M_x/M_*). P_b and i are known (see Table 2.1), and K and q can be measured. Therefore, F, and consequently M_x and M_*, can be derived.

Gies et al. (2002) report that the Hα profiles are characterized by a central emission core and broad wings that extend to $\pm$2000 km/s. Both the core and wings of the Hα features are variable in time, varying from a strong, rounded-top emission line to a weaker, **P Cygni profile**. It has been suggested that winds from disks can produce both of these variations, depending on the disk orientation. Thus, Gies et al. (2002) determine that the variations seen in the stationary lines of SS 433 are, at least partially, a result from temporal changes in the wind structure.

All of the observations presented by Gies et al. (2002) suggest that the binary is embedded in a large equatorial disk that is formed by the disk wind, and extends far beyond the binary itself. The disk probably widens with distance from the binary

because of changing orientation of the disk wind source with precession.

Optical and infrared observations of SS 433 have been shedding light on the key properties of this system for over 25 years (Abell & Margon, 1979; Katz et al., 1982; Milgrom, 1979, etc.). They have revealed the presence of both moving and stationary lines in the spectra, which led to the discovery of the precessing jets and the binary companion. These observations have also proven the existence of a thick accretion disk that surrounds the binary system. Of course, there are still many unanswered questions that could be unlocked by observations in other wavelengths.

2.4 Radio Observations

2.4.1 SS 433

The radio source associated with SS 433 was first observed ten years prior to the recognition of its unusual properties. However, it was officially discovered by Ryle et al. (1978) and Seaquist et al. (1979). It was realized that a significant fraction of the flux from SS 433 is extended on spatial scales of a few arcseconds, and that the morphology of this extension is variable in time. The observed morphology changes on a time scale of days, and gives the impression of a 'corkscrew' pattern projected onto the plane of the sky.

Radio data are important because the relativistic blobs in the jets can be observed directly, rather than inferring this motion indirectly. This allows for a derivation of other key system parameters. Hjellming & Johnston (1981) presented radio data that show the above mentioned corkscrew morphology, and use it to complete a three-dimensional model of the kinematics of the twin jets moving outward from SS 433.

Since the radio-emitting region has characteristic dimensions 100 times greater than the optically radiating portions of the jets, light travel delays become important, and consistent kinematic solutions are impossible without their inclusion. The corkscrew pattern tracks the proper motions of the jet blobs. Since the linear velocity of the material in the jet is also known, this allows for a determination of the distance to SS 433 (5 kpc). The degeneracy of the system angles (θ and i) is also broken down by radio observations, and it is found that the inclination is 78^o (see below). Even the sense of the jet rotation (retrograde with respect to binary orbital motion) can be found.

The parameters of the radio jets agree with those found with the kinematic model for the optical jets, and also supplement the optical data by determining all of the remaining parameters for a unified kinematic model of material moving outward from the central regions of SS 433. Therefore, the Hjellming & Johnston (1981) study represents an elegant verification that the twin-jet model is in fact correct for the moving spectral lines.

2.4.2 W50

The first high resolution observation of the W50 supernova remnant (SNR) was obtained by Clark, Green & Caswell (1975). Their observations reveal a curved ridge of emission and two unresolved radio point sources, one (1910+052) within the ridge, and the other (1909+048) found below it. Clark & Murdin (1978) determined that 1909+048 was a 14th magnitude star, SS 433, which displayed a very unusual emission-line spectrum. A 2695 MHz map of the SNR by Velusamy & Kundu (1974) suggests that this object is in fact near the center of W50.

Geldzahler et al. (1980) studied W50 in the radio continuum at 2695 MHz, and found the structure of the remnant is exceedingly complicated. Before this study, it was suggested that the two radio "ears" were not associated with the spherical remnant. However, their Figure 1 (seen in Figure 2.6) shows that it is difficult to split it up into distinct components. Also, the similarity of the polarization position angles and the continuity of the outer brightness-temperature gradient adds weight to this suggestion.

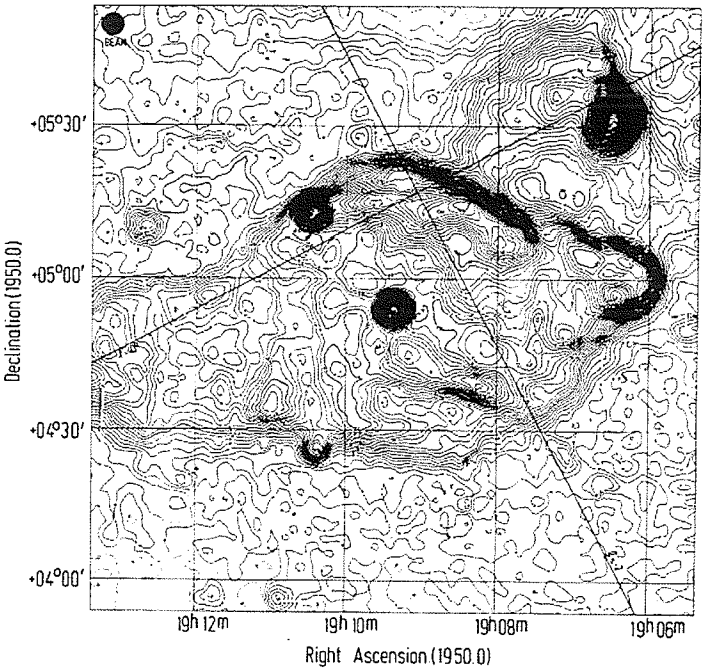

Figure 2.6: The map of W50 at 2695 MHz with radio contours. Note the "ears" in the east and west (Figure 1 from Geldzahler et al. (1980)).

Using their derived values of the flux densities and spectral index, they were able to estimate the mean linear diameter, distance, and height above the Galactic plane for W50. Using two different models (assuming the nebula is spherical or elliptical

in shape), they found a mean diameter of 40-65 pc, a distance of 2-3 kpc, and that it lies 70-115 pc below the Galactic plane.

Geldzahler et al. (1980) also observed a weak loop of emission to the northwest of W50, which had earlier been cataloged as an H II region, S74. They suggest that, if its emission extends over a complete circle, it will overlie the northwestern edge of W50 and could account for at least some of the emission in the ridge. The derived distances of W50 and S74 are close, and therefore any interactions between the two would be important.

Another important study of the W50 SNR was done by Elston & Baum (1987), in which they present the highest resolution radio observation at that time. They find that W50 has many traits in common to shell-type SNRs: 1) a nearly circular blast-wave shell in the north-south direction, 2) ridges of radio emission crossing the shell, 3) spatial coincidence of optical and radio filaments, and 4) X-ray emitting gas in the interior of the shell. However, it also possesses many unique traits (see Figure 2.7): 1) a sudden break in the radio shell at the location of the radio ears, 2) the morphology of the radio ears, and 3) the spatial distribution of the X-ray emission and its association with radio and optical filaments.

Another important conclusion that Elston & Baum (1987) suggest is that the diverse structure of W50 is probably the result of a non-uniform ISM. There is a large brightness asymmetry of the northern and southern parts of the spherical shell, which may be due to the differences in the medium that the shock is moving into. The ears also have different morphology, with the western ear being shorter and brighter. This can be understood if the ISM to the east has lower density.

The presence of the H II region, S74, northwest of W50 is most probably the

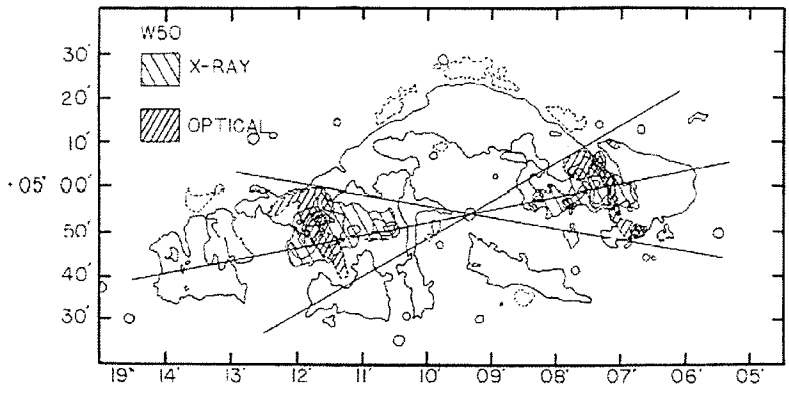

Figure 2.7: Map of 5σ contours of W50. Overlaid are the precession cone of the jets, the X-ray emission and the locations of optical filaments (Figure 4 in Elston & Baum (1987)).

cause of this density gradient. This is supported by the fact that emission from the eastern ear is highly polarized, where that of the western ear is depolarized. This implies W50 and S74 are at a common distance, as explained by Elston & Baum (1987) as follows: if the H II region is in front of W50, there would be a large enough rotation measure (measure of observed variation of linear polarization) to depolarize the western ear. However, it would require well distributed, high density inhomogeneities to complete the depolarization. If, on the other hand, S74 and W50 were interacting, the western ear of W50 would be depolarized by plasma mixed in the emitting region. For this to occur, a plasma density of ≥ 10 cm^{-3} is needed. Elston & Baum (1987) and references therein report a density of the base of the western ear to be ~ 100 cm^{-3}. They assume that the density difference to the outer ear would not be more than an order of magnitude, giving an adequate density to depolarize the ear.

A more recent study by Dubner et al. (1998) includes an even higher resolution image of W50 (Figure 2.8). They were able to reveal the complex structure of the extended source in great detail. Of particular interest are the set of filaments that run vertically across the east wing at distance of 0.5^o to 1^o from SS 433. These features are suggestive of a helical structure. The observed diameter of these features are contained within the $\sim 40^o$ precession angle of the relativistic jets from SS 433. This indicates that the helical structure are the large-scale traces of the subarcsecond beams. To further support this, the interspacing of the helix has a very regular value of $5'.2 \pm 0'.4$.

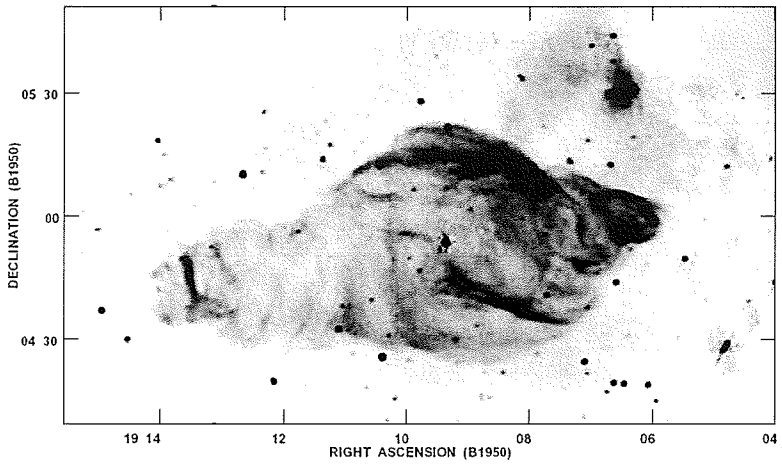

Figure 2.8: VLA radio continuum image of W50 at 1465 MHz in grey scale (Figure 1b from Dubner et al. (1998)).

Dubner et al. (1998) also note, as with previous studies, that the differing morphology around the remnant suggests a difference in acceleration processes of the relativistic particles. Because of the higher resolution, they were able to determine spectral indices for the different regions. For the central circular region $\alpha = 0.56 \pm 0.05$,

for the eastern wing α=0.82±0.05 and for the western wing α=0.49±0.09. The flatter index in the west indicates the presence of stronger shocks and higher compression in regions where the shock in encountering dense clouds (i.e. S74). The steepening toward the east is consistent with the jet propagating into a more diffuse region (see Appendix E).

In summary, radio observations are important in studying both SS 433 and W50, as they reveal key information about the physical processes near the source as well as the morphology of the nebula. This in turn can lead to strong indications of the connection between the relativistic jets of SS 433 and the oddly shaped W50 SNR. They also prove helpful in verifying previous results derived from observations in optical or infrared.

2.5 X-ray and Gamma-ray Observations

The first reported X-ray observations of this area of the sky were obtained by *Ariel V* in 1974-75 and were reported by Seward et al. (1976). They commented that the source was a candidate for identification with a compact stellar remnant. The X-ray source also appears in the 4U catalogue, compiled with *Uhuru*. Neither observations indicated that this source was unusual in any way as compared with the dozens of brighter X-ray sources in the Galactic plane. The estimated X-ray (2-10 keV) luminosity at this time was on the order of 10^{35} erg/s (Marshall et al., 1979; Seward et al., 1976), much smaller than the kinetic luminosity of the material in the jets, $L_J \sim 10^{39-40}$ erg/s (Margon, 1984; Brinkmann, Kotani & Kawai, 2005).

Marshall et al. (1979) analyzed the X-ray spectrum obtained with the *HEAO-1 A-2* experiment in the 2-30 keV range. At this time, the resolution was not good enough to indicate if the emission was thermal or non-thermal in nature, but both models required a very prominent (580 eV equivalent width) emission line at 6.8 keV. This line is a result of unresolved transitions of highly ionized iron, and is common in compact Galactic X-ray sources.

The *Einstein* observatory contributed largely to the spatial structure of SS 433. The first X-ray imaging observations show that 90% of the soft X-ray flux (1-3 keV) is coincident with the compact object, while 10% is contained in two extended (30′) jets that are closely aligned with the major axis of W50. This confirms the assocation of SS 433 and W50. It also gives further evidence for the existence of the ejected jets, and a minimum age of several thousand years is established from the ejection phenomenon (by knowing the velocity of the jets and the distance to W50; Seward et al. (1980)).

The X-ray intensity of SS 433 is highly variable on a number of different time scales. Daily variations have been observed, on some occasions being correlated with radio flares. Safi-Harb & Kotani (2002) and Kotani et al. (2002) give the first evidence for short time scale X-ray variability, on the order of 50-100 s. The spectral behavior observed mimics that seen in other microquasars. The fast variability is expected from super-Eddington accretion into the surface of a neutron star. These short time scales reveal that the high energy emission regions close to the compact object are being probed for the first time.

Until recently, the derived mass ratios from X-ray observations did not agree with those found using optical data. In fact, the accepted range determined with optical

observations for the mass ratio is q = M_x/M_* = 0.4-1.2, which points toward the compact object most probably being a black hole. On the other hand, the mass ratio derived from X-ray data was q = 0.15-0.25, which leads to the conclusion that the compact object must be a neutron star. However, it was recently reported (H. Marshall 2005, private communication) that q is derived to be 0.55 from X-ray data, which agrees with the previously reported optical results, and supports the suggestion for a black hole.

A study performed by Cherepashchuk et al. (2003) with *INTEGRAL* (a gamma-ray observatory) also indicates that the compact object is a black hole. Although SS 433 had been studied in the high X-ray energies before with *RXTE*, the detector on board *INTEGRAL* offers a unique opportunity to study this system up to hundreds of keV. However, it should be noted that the spectrum at this high energy had very few data points, and better spectra should be obtained in gamma-ray frequencies to verify these results.

X-ray observations have also been performed on the W50 nebula. Watson et al. (1983), using the *Einstein* observatory, found two bright diffuse lobes symmetrically displaced east and west of SS 433 and aligned with the W50 axis. Each lobe is visible from $\sim$15′ to $\sim$40′ from SS 433, having the emission peaking at $\sim$35′. This peak corresponds to the optical filaments and lies near the base of the radio lobes. *ASCA* studies of the eastern lobe by Yamauchi, Kawai & Aoki (1994) and Safi-Harb & Ögelman (1997) reveal a non-thermal nature of the lobe. A recent study by Moldowan et al. (2005) also reveals a non-thermal nature of the X-ray emission from the western lobe of SS 433 (see Chapter 4 for more detail). Both the eastern and western wings have a knotty structure (Safi-Harb & Ögelman, 1997; Moldowan

et al., 2005), which is a similar morphological feature to **active galactic nuclei (AGNs)**. It is also reported that the emission regions of both lobes show a general trend of spectral softening away from SS 433.

X-ray and gamma-ray observations are important to the study of both the SS 433 system and W50 nebula. It enables us to observe further into the binary system than with any other instrument, which allows for a more advanced study of the jets and the companion and compact stars. Of course, these observations also verify previous results, so as to solidify the understanding of this system.

2.6 Extragalactic Analogy

One of the most intriguing implications of the twin-jet model of SS 433 has been appreciated since it was first hypothesized and was the primary motivation for that line of interpretation: collimated, relativistic outflow of material is thought to be a basic, recurring phenomenon in a variety of AGN, including radio galaxies and quasi-stellar objects. If there is in fact a similarity between the basic physical processes, this allows for a study of the microscopic details of jet interaction, collimation, and precession processes in these AGNs through repeated observations of SS 433. The time scales for observable changes in the SS 433 jets are probably $\sim 10^5$ times more rapid than in the extragalactic cases.

2.7 Summary

The SS 433 system is truly unique. Observations of other X-ray binary systems within SNRs have been made. Circinus X-1 was thought to be one such object

(Margon, 1984), but observations show there is no evidence for the main peculiarity of SS 433, i.e. the collimated, relativistic jets. Other objects such as the "Red Rectangle", the bipolar nebula surrounding HD 44179, or the pulsating X-ray source 2259+586 centered in the SNR G109.1-1.0, have been considered to be SS 433-like (Margon, 1984). Again, further observations indicate that they are interesting objects, but probably quite different than the SS 433 system. In fact, 2259+586 has been found to be an **anomalous X-ray pulsar (AXP)**. See Safi-Harb (2005) for a review of other objects that are similar to the SS 433/W50 system.

It is imperative that observations in multiple wavelengths of both SS 433 and W50 are used to explain their unique and mysterious features. The countless observations performed on this system has provided a very accurate description of the jet motions, and have allowed for more accurate determinations of the many properties. Multi-wavelength observations of SS 433 and W50 are useful to verify previous results in order to solidify the models, and also to delve into new regions which have yet to be observed. Performing simultaneous observations in multiple frequencies could help solve the number of outstanding puzzles: the masses and nature of the donor and compact stars, the distance to the system, the jet formation process, the origin of disk precession, the emission mechanisms, the evolutionary state of the binary and the interaction of the W50 nebula with the ISM.

Chapter 3

Instrumentation

The understanding of X-ray binary systems and nebulae is tied to the scientific capabilities of the instruments used to observe them. The data in this thesis was acquired with the *Chandra* X-ray Observatory and the Rossi X-ray Timing Explorer (*RXTE*). The next two sections describe these instruments and data analysis procedures.

3.1 The *Chandra* X-ray Observatory

The *Chandra* X-ray Observatory, formerly known as *AXAF* (Advanced X-ray Astrophysics Facility), was launched in July, 1999. Its instruments consist of a high resolution mirror, two imaging detectors and two sets of transmission gratings. It is in an elliptical high-earth orbit, with a perigee of 29,000 km and an apogee of 120,000 km (as of December, 2004), more than one-third of the distance to the Moon. One orbit has a period of about 64 hours and 18 minutes, spending approximately 75% of this time above the van Allen belts, making uninterupted observations of up to 55 hours possible.

The High Resolution Mirror Assembly (HRMA) consists of four pairs of grazing-incident nested mirrors, the largest having a diameter of 1.2 m. The two imaging detectors, the High Resolution Camera (HRC) and the Advanced CCD Imaging Spectrometer (ACIS), are located on the focal plane. The HRC is used for high resolution imaging and fast timing measurements. It consists of two Micro-Channel

Plates (MCP), the HRC-I, designed for wide-field imaging, and HRC-S, specifically designed for the use of timing measurements. ACIS is comprised of two arrays of charged coupled devices (CCDs), a four chip array (ACIS-I) and a six chip array (ACIS-S), and can simultaneously provide imaging and spectroscopy data. This is useful for studying temperature and/or chemical gradients in X-ray sources. More detailed descriptions and images of all the components can be found on the *Chandra* X-ray Center (CXC) website (cxc.harvard.edu).

3.1.1 Advanced CCD Imaging Spectrometer

ACIS is unique in that it can simultaneously create high resolution images and moderate resolution spectra. With use in conjunction with either of the transmission gratings, higher resolution spectra can be obtained.

ACIS is made up of ten 1024×1024 pixel CCDs, which are split up into two arrays: ACIS-I is a 2×2 array for imaging, and ACIS-S is a 1×6 array for imaging or grating readout (see Figure 3.1). Up to six CCDs may be simultaneously used in any configuration. Although, it should be noted that this can greatly increase the total background count rate.

3.1.2 *Chandra* Data Reduction

The advantages of *Chandra* can only be fully utilized if the data obtained is processed carefully. It is possible to perform analysis on data straight from the CXC pipeline, which creates both level 0 and level 1 files. Level 0 files are created by splitting the raw **telemetry** data into FITS files. Level 1 files are sent to the observer, and are created by applying instrument dependent corrections. To get scientifically

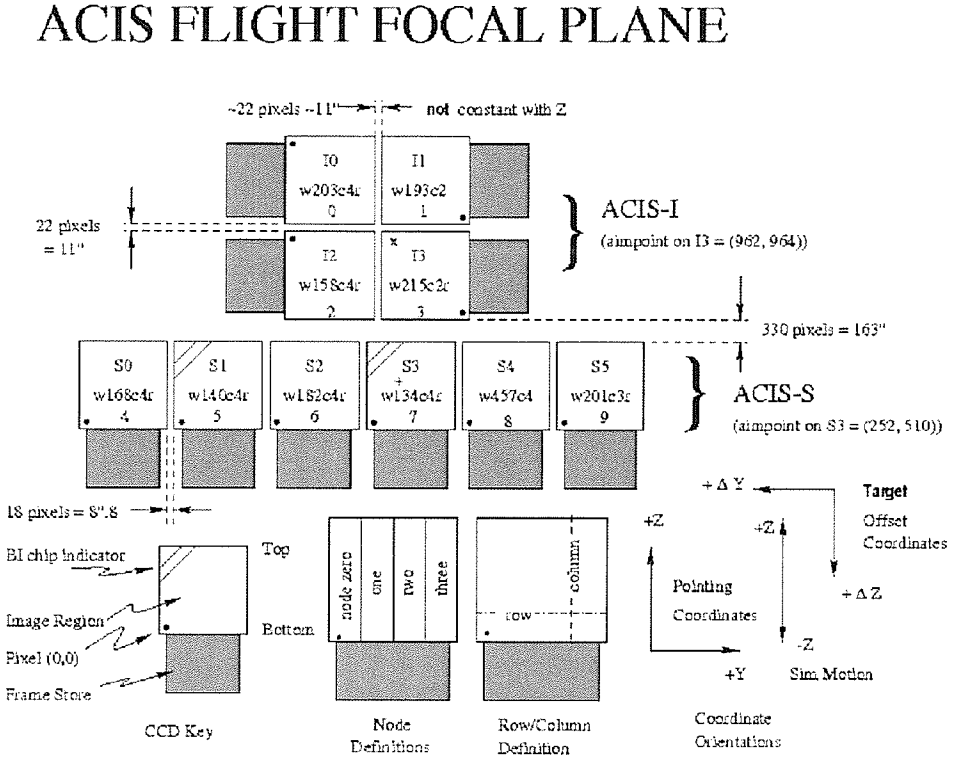

Figure 3.1: A Schematic drawing of the ACIS focal plane, including both ACIS CCD arrays (available at http://cxc.harvard.edu/proposer/POG/html).

accurate results, a level 2 file is then created by the observer by answering a number of questions separately for each observation.

Certain calibration files are needed for the standard processing of all *Chandra* data, which are stored in the calibration database directory (CALDB). The data reduction and analysis performed for this thesis was done with the *Chandra* Interactive Analysis of Observations (CIAO) version 3.0 software. A more technical and detailed description of the tools and threads (series of commands) used for this thesis can be found at http://cxc.harvard.edu/ciao/threads/index.html.

ACIS Data Preparation

The following are considerations in creating a new event file (Level 2) from the raw data from the pipeline (Level 1) for imaging and spectral analysis valid for this thesis.

I. CTI Correction

The loss of charge in a CCD as it is shifted from one pixel to the next during readout is known as charge transfer inefficiency (CTI). The charge is read out at only one location on the node, so charges at all other locations must be moved to the readout. As they move, some may be caught in charge traps that are distributed across the detector. This effect causes CTI.

An algorithm has been developed to estimate the amount of charge deposited on a CCD for an event, and is implemented in the tool ACIS_PROCESS_EVENTS (see http://cxc.harvard.edu/ciao/why/cti.html for more details). The use of the CTI correction eliminates nearly all of the apparent gain shift and drastically improves the energy resolution of the detector. It needs to be performed on data that is either taken at -120°C, uses the ACIS-I CCDs or the ACIS-S2 CCD, and the analysis will involve spectral studies. Since more than one of these describe the data used in the analysis in this thesis, this was the first step performed on the Level 1 file. The algorithm is implemented in the ACIS_PROCESS_EVENTS tool by setting the options *apply_cti=yes* and *ctifile=CALDB*.

II. ACIS Gain Map

The pulse height amplitude (PHA) is an engineering unit that describes the integrated charge per pixel from an event recorded in a detector. A gain table is used to map the PHA of an event to the energy value. Using this map, the energy value is con-

verted into a pulse invariant (PI) value using the equation PI=[(energy/14.6 keV)+1], where PI is in units of detector energy channels. The resulting spectral data can be added (binned) according to the needs of the analysis. Thus, correcting the gain map is important if one is doing any type of spectral analysis on ACIS data. As with the CTI correction, this is implemented in the ACIS_PROCESS_EVENTS tool, by setting *gainfile=CALDB*.

III. Event Grades

The local maxima for events are detected using 3×3 pixel islands, and are assigned grades based on the pattern of pixels within the island whose charge exceeds a certain value. Specific grades are most probably known to be caused by X-ray photons, so these events are kept. Most X-ray events occurring at energies less than ~2 keV are predominantly grade 0 (g0), indicating that a single pixel contains all of the charge. Events at higher energies tend to be a mix of other grades, with grade 6 (g6) predominating. Depending on the grade, the event may or may not be included in the telemetry.

When high energy particles (electrons and protons) pass through a CCD, they deposit a significant amount of ionizing radiation, generating up to hundreds of events. These events usually have charge deposited in at least five or six pixels of the island. These types of events generally have grades of 1, 5 or 7, and can be discriminated against purely on their event grade. To do this for the data used for the analysis in this thesis the tool DMCOPY is used with the option *grade=0,2,3,4,6*.

IV. Good Time Intervals

A list of good time intervals (GTI) is supplied by the pipeline, and includes observation periods that are not excluded by bad conditions such as a high background or an unstable aspect (the pointing position of the telescope as a function of time). The GTIs are contained in the Level 1 event file, and can be selected using the tool DMCOPY and the option *@evt1_filename.fits.*

V. Filtering

The energy scale of the ACIS CCDs is only calibrated over the range 0.277 - 9.886 keV (the carbon K and germanium K lines, respectively). Data outside of this range should normally not be used when performing spectral and image analysis. Thus, an energy range of 0.3-10 keV can be selected using the DMCOPY tool and the option *energy=300:10000.* This produces the final Level 2 event file used for analysis.

ACIS Background

The ACIS background consists of a relatively soft Cosmic X-ray Background (CXB) contribution and cosmic ray induced events with a hard spectrum. Most cosmic ray events can be filtered out by applying a grade filter as noted above. After such filtering, the CXB component and the cosmic ray component are comparable below $\sim$2 keV (during the quiescent background intervals, see below) and the cosmic ray component dominates above that energy.

A phenomenon that can seriously affect the scientific value of an observation are background flares, when the count rate can increase by a factor of up to 100. Unless the target is a bright point source, it is usually best to discard the time intervals where the flares are present.

During the quiescent periods and after the standard event screening, the background appears to be relatively constant with time. The weak dependence of the background on time allows users to use different observations that have been cleaned for flares as models for background. A number of source-free observations have been combined to create quiescent background event files, known as 'blank-sky' datasets. These files can be used to estimate the background for spectral and image analysis.

Very Faint Mode

There is a variety of telemetry formats available in which the ACIS CCDs can be operated. Specifying a format determines the type of information that is included in the telemetry stream. The data for this thesis were obtained using the Very Faint (VF) telemetry format, which provides the event position in detector coordinates, the event amplitude, arrival time, and the pixel values in a 5×5 island. This format offers the advantage of reduced background after ground processing but only for sources with low counting rates that avoid both telemetry saturation (limit at which ACIS looses its capacity to send all of the detected events to the ground) and pulse pile-up (X-rays of peak energy E1 are measured, but pulse coincidence can lead to a continuous band of overlapping pulses in the range E1 to 2E1, creating a pulse pile-up continuum).

The 5×5 event islands recorded in the VF mode reveals that a large number of events are in fact the end-points of big particles tracks. Such events can be screened by rejecting those in which any border pixel in the 5×5 island is above the split threshold. This correction can be made by using the ACIS_PROCESS_EVENTS tool with the option *check_vf_pha=yes*.

3.1.3 *Chandra* Image Analysis

An example of an image of the western lobe of W50 created directly from the Level 2 event file is seen in Figure 3.2. The usual method for creating a true-color image uses energy ranges of 300:1,500 eV, 1,500:2,500 eV or 2,500:10,000 eV to split the event file into three separate files for soft, medium and hard X-ray energies. However, because this particular image is so faint, only two energy ranges were used (0.3-2.4 keV and 2.4-10 keV), and regions of hard and soft X-ray emission can be determined.

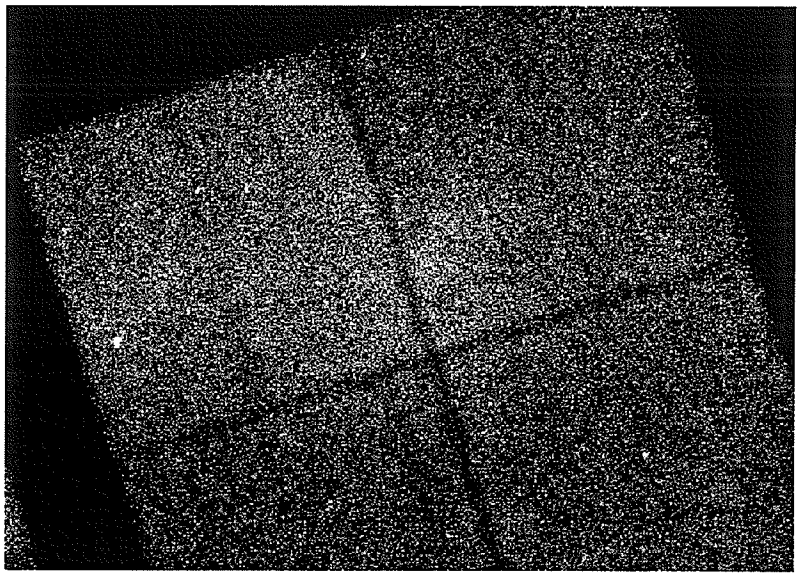

Figure 3.2: The *Chandra* image of the western lobe of W50 created from the Level 2 event file. As seen here, the source is very faint. Thus, the typical procedure for making a true-color image cannot be used.

The image is then smoothed using CSMOOTH, to blur the image and to remove noise. This tool uses a Gaussian smoothing algorithm to further process the image.

A two dimensional symmetric Gaussian distribution is given by

$$\frac{1}{2\pi\sigma} exp\Big(- \frac{x^2 + y^2}{2\sigma^2} \Big) \tag{3.1}$$

where σ is the standard deviation of the distribution. The smoothing scale or kernel size, which is the degree of smoothing, is determined by the size of σ. The technique adjusts the size of the kernel to match the local surface brightness (i.e. counts per pixel) so that the user defined significance level will be achieved. In regions of high brightness the smoothing function is on a small scale, while at low brightness the function increases to higher scales. This process was applied to the images used in this thesis, by smoothing with a Gaussian with σ=0″.5 (see http://cxc.harvard.edu/ciao/ahelp/csmooth.html for more details).

Using Gimp (an imaging software package), the two energy images were layered together using red and blue for the low and high energy images, respectively. The resulting image is seen in Figure 3.3.

To achieve a better image, the CIAO thread "Create an Image of Diffuse Emission" was used (see http://cxc.harvard.edu/ciao/threads/diffuse_emission/ for details). The procedure in this thread is intended to make a nice image for a poster or a paper, and to aid in the understanding of the morphology of the extended emission. The final output is not used for spectral analysis. The final image can be seen in Figure 4.2 in Chapter 4.

Using this image, regions of interest can be chosen for spectroscopic studies. Separate background regions are created for each source region so as to calibrate the emission more accurately. This correction is achieved using the ACISSPEC tool, which produces source and background spectra. Once this is complete, the spectra

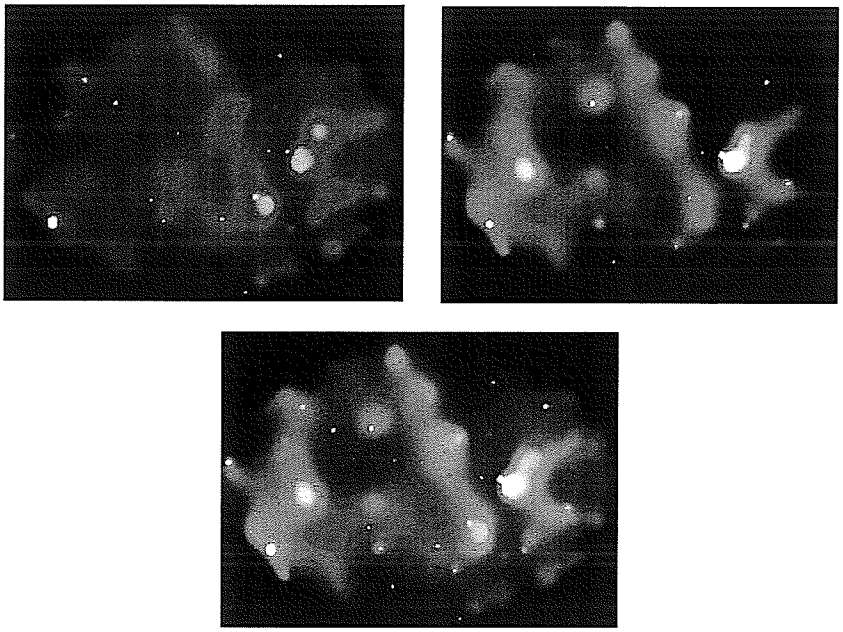

Figure 3.3: The red and blue images depict the 0.3-2.4 keV and 2.4-10 keV energy ranges, respectively. Each image was smoothed with a Gaussian with σ=0″.5. The bottom figure is the two images layered together.

can be analyzed using XSPEC, an X-ray spectral fitting program.

3.2 The Rossi X-ray Timing Explorer

The Rossi X-ray Timing Explorer (*RXTE*) was launched on board a Delta II rocket on December 30th, 1995 from NASA's Kennedy Space Center. It orbits at an altitude of 580 km, with an orbital period of about 90 minutes and an inclination of 23°. *RXTE* has unprecedented time resolution, covering timescales from microseconds to months, and moderate spectral resolution over a 2-250 keV energy range that combine to explore the variability of X-ray sources.

RXTE has two pointing instruments: the Proportional Counter Array (PCA), optimized for the lower (2-60 keV) energy range, and the High Energy X-ray Timing Experiment (HEXTE) that is used for the upper (15-250 keV) energy range. The two instruments are co-aligned and both have a field of view of 1^o full-width-half-max (FWHM). The energy resolution for the *PCA* and *HEXTE* is 18% at 6 keV and 60 keV, respectively, while they have 1μs and 10μs temporal resolutions. Also on board is the All Sky Monitor (ASM) built by MIT, and scans ~80% of the sky each orbit. The *PCA* and ASM data are processed on board using the Experiment Data System (EDS) built by MIT. For schematic drawings of the satellite and components, see http://heasarc.gsfc.nasa.gov/Images/xte/. All technical information for this section is found in the *RXTE* technical appendix F (available at http://rxte.gsfc.nasa.gov/docs/xte/appendix_f.html).

3.2.1 The Proportional Counter Array

The *PCA* consists of five identical sealed and collimated (1^o FWHM) xenon/methane multi-anode proportional counter units (PCUs) sensitive to X-rays in the energy range of 2-60 keV. Each PCU has four xenon grid layers, the upper three being used for X-ray detection. The total effective area at the peak of the efficiency curve is approximately 7,000 cm^2. The *PCA* allows for a rejection of background events caused by charged particles with high efficiency which significantly reduces the residual background event rate at lower energies.

3.2.2 The High Energy X-ray Timing Experiment

The *HEXTE* consists of two independent clusters each containing four detectors collimated to a 1^o FWHM field of view, and are co-aligned with the *PCA*. Each detector has a net open area of about 225 cm^2 and covers the energy range of 15-250 keV, with an intrinsic spectral resolution better than 9 keV at 60 keV. The two clusters contain mutually orthogonal "rocking" mechanisms, which can be moved independently to provide near simultaneous measurements of the internal and cosmic X-ray backgrounds at 1.5^o or 3^o on either side of the source.

3.2.3 Data Reduction

The *PCA* and *HEXTE* data are reduced using different methods. This section summarizes these methods, along with the variables to be taken into account when performing data reduction.

PCA Data Reduction

The *PCA* data used for this thesis was in the Binned Mode, and thus the recipe "Reduction and Analysis of *PCA* Binned-Mode Data" was used (available from http://heasarc.gsfc.nasa.gov/docs/xte/recipes/pca_spectra.html). The Standard-2 data, automatically used in all data analysis, provides all of the key information for accurate spectral analysis:

- PCU ID - each PCU has a slightly different response.
- Anode ID - For most sources, the best signal-to-noise is to be obtained from the top layer anode, since it receives the greatest source flux. Therefore, only this layer is used in the analysis for this thesis.

- At least 64 PHA bins - Being a proportional counter, the PCA has a somewhat crude spectral resolution: the 129 channels of Standard-2 (as opposed to the full 256) can be used without a loss of resolution.

There is a script, REX, that goes through most of the appropriate steps for reducing *PCA* data (available from http://heasarc.gsfc.nasa.gov/docs/xte/recipes/rex.html). It choses to use only the top layer data (as explained above) and PCUs 0, 1 and 2, since 3 and 4 go off and on regularly. For selection criteria, see Appendix B for more details. The final spectra can be analyzed in XSPEC.

HEXTE Data Reduction

The recipe used for the *HEXTE* data reduction completed for this thesis was "Reduction & Analysis of *HEXTE* Data" (available from the *RXTE* website, http://heasarc.gsfc.nasa.gov/docs/xte/recipes/hexte.html).

The files are divided into either science data or housekeeping data (see Table 3.1).

Table 3.1: Summary of *HEXTE* File Names

Data Type	ClusterA (Cl0)	ClusterB (Cl1)
Science data	FS50	FS56
Standard modes (archive data)	FS52	FS58
Calibration data	FS54	FS55
16s Housekeeping	FH53	FH59
128s Housekeeping	FHfd	FHfe

It should be noted that one of the detectors in Cluster 1 has lost its spectral capabilities. Thus, for spectral analysis, its data are incorrect. For this thesis, since

the majority of the *RXTE* study is spectroscopy, only Cluster 0 data has been used in the analysis. Also, if there is more than one science file (FS50), then the light curves and spectra must be combined. See Appendix C for scripts used for the *HEXTE* data reduction. The resulting files can then be used in XSPEC to analyze the spectra.

Chapter 4

The Multi-Wavelength Study of the W50 Nebula

Most of this chapter has been taking directly from the paper, Moldowan et al. (2005). Details and explanations have been added as necessary, as well as section 4.3.4 on the point sources in the *Chandra* field.

4.1 Introduction

SS 433 is near the center of W50, a large $2^\circ \times 1^\circ$ nebula stretched in the east-west direction, and cataloged as an SNR (Green, 2005). The SS 433/W50 system is the only Galactic object known of its kind, giving rise to a unique laboratory to study the association between SNRs and black holes as well as the interaction between relativistic jets and the surrounding medium.

The elongated morphology of W50 has been attributed to the impact of the SS 433 jets energizing and distorting the shell. From multi-wavelength studies, it has been concluded that the morphology and energetics of W50 are consistent with the picture of the jets interacting with an inhomogeneous medium and likely hitting a dense cloud in the west.

The *Chandra* observation presented here provides the highest resolution X-ray image obtained to date of the bright region of the western lobe of W50. This region was chosen because it coincides with infrared (IR) emission and can probe the jet-cloud interaction site. For this thesis, a spatially resolved spectroscopic study of this

region was performed to primarily determine the nature of the emission and correlate the X-ray emission with radio and IR observations. Before this study, the nature of the emission from the western lobe of W50 had not been accurately determined.

4.2 Observations and Data Reduction

The western lobe of W50 was observed with the ACIS-I chips on board *Chandra* on 2003 August 21 at a CCD temperature of -120°C. The charge transfer inefficiency (CTI) was corrected using the APPLY_CTI tool on the level 1 raw data. A new level 2 file was then obtained using the standard CIAO 3.0 routines. See section 3.1.2 of this thesis for details on the *Chandra* data reduction tools and commands. The final exposure time was 71 ksec.

4.3 Data Analysis

4.3.1 Imaging

To illustrate the W50 region covered by *Chandra*, Figure 4.1 shows the radio image of W50 (grey scale), and the regions covered by observations in infrared (large box) and X-ray (small box). The projection on the sky of the precession cone axes of the SS 433 jets is also overlayed. The radio image shows that the eastern wing of W50 exhibits a corkscrew pattern, which mimics the precession of the arcseconds-scale jets from SS 433 (Dubner et al., 1998, Hjellming & Johnston, 1981).

Interestingly, there is a hint of a corkscrew pattern visible in the *Chandra* image (Figure 4.2), supporting the conclusion that the SS 433 subarcsecond-scale relativistic jets are affecting the large scale radio and X-ray emission from W50. It is noted that

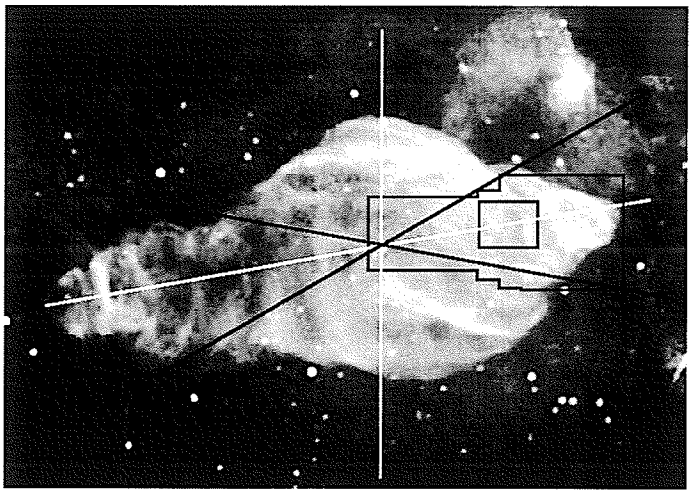

Figure 4.1: The image of W50, measuring 2^o by 1^o, in radio. The large and small boxes represent the field of view of the infrared and X-ray observations, respectively. The position angle of the jet cone is 100° (measured from N to E).

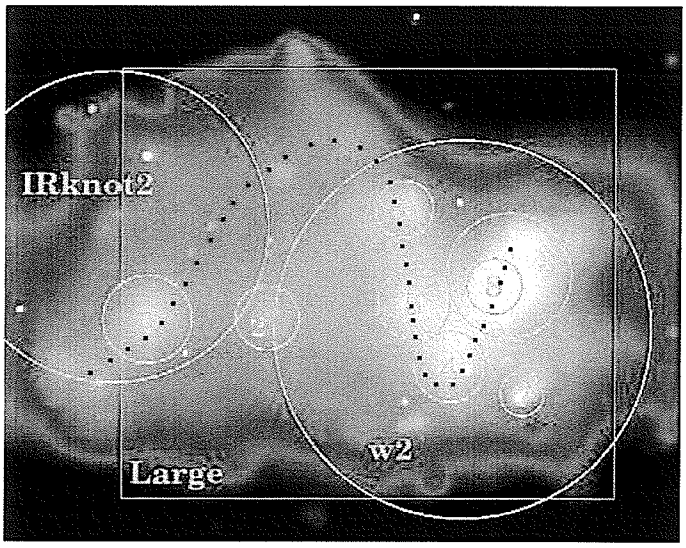

Figure 4.2: The 0.3-10 keV image of W50, corresponding to the small box in Figure 4.1, showing regions used for spectroscopy. The dots hint to a corkscrew pattern. See Figure 4.4 for scale.

the pattern traced in Figure 4.2 is most likely not the true corkscrew pattern, as the *Chandra* region is embedded in the much larger radio ear. It is only meant to guide the reader's eye.

In Figure 3.3 in Chapter 3, the energy image is shown in which red corresponds to the soft energy band (0.3-2.4 keV) and blue corresponds to the hard energy band (2.4-10 keV). In Figure 4.2, the intensity image is shown in the 0.3-10 keV energy range. These images were created using the methods outlined in section 3.1.3 of this thesis. Many point sources are resolved in the field and the knotty structure of the nebula is noted. The X-ray emission peaks at α (J2000) = $19^h\ 09^m\ 42^s.86$, δ (J2000) = $05^\circ\ 03'\ 38''.8$.

4.3.2 Spectroscopy

To perform spatially resolved spectroscopy of the remnant, the point sources were excluded from the *Chandra* field, and spectra were extracted from the diffuse emission for 11 regions shown in Figure 4.2. The w2 and IRknot2 regions correspond to the X-ray w2 region presented in Safi-Harb & Ögelman (1997) and the infrared knot2 region presented by Band (1987), respectively. These regions are selected in order to compare the *Chandra* results with those found in X-rays with *ROSAT* and *ASCA* and in infrared with *ISOCAM*.

The proximity of the western lobe to the Galactic plane complicates the spectral analysis because of contamination by the Galactic ridge. To minimize this contamination, several background regions were extracted from source-free regions around the diffuse emission from W50. These background regions consist of 6 circular regions (see Figure 4.3). Subsequently, the spectral parameters for the three largest regions

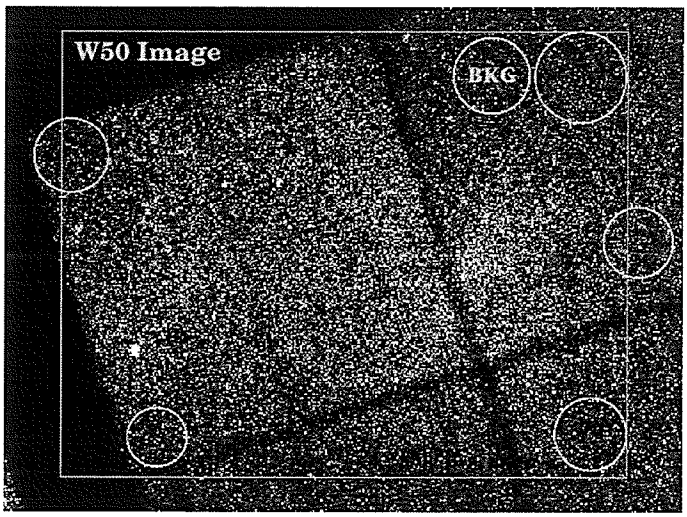

Figure 4.3: The background regions used in the analysis. The region marked by BKG is the region used for the spectral analysis of regions 1-8. The area of the W50 image (i.e. the dimensions of Figure 4.2) is also shown for comparison.

(w2, IRknot2, and Large) were determined using the resulting average background. For the eight smaller regions, this over-subtracts the background, so only one of the circular regions (marked BKG in Figure 4.3) is used. Spectra were extracted in the 0.5-10.0 keV range for all regions, except for the IRknot2 region, which used a range of 1.0-10.0 keV because of large error bars at low energies.

To determine whether the emission is thermal or not, the spectra were fitted with thermal bremsstrahlung and power-law models (following Safi-Harb & Ögelman, 1997). The bremsstrahlung model is characterized by the shock temperature (i.e. plasma temperature), kT, and the power-law model is characterized by the photon index, Γ. For an explanation of thermal and non-thermal X-ray emission mechanisms, see Appendix A.

Both models give adequate fits in each region. However, it is found that the

power-law models give slightly lower reduced χ^2 (see Appendix E for definition) values, and that the temperatures derived from the thermal bremsstrahlung models are high (unrealistically high for even the youngest SNRs). This, together with the absence of line emission in the spectra, leads to favoring a non-thermal interpretation for the X-ray emission.

Table 4.1 summarizes the *Chandra* results for the regions seen in Figure 4.2. A distance of 3 kpc (denoted by D_3) is used in the luminosity calculations (as in Dubner et al., 1998), the errors are at the 90% confidence level, and N_H refers to the column density of neutral hydrogen. Note that the spectrum softens with increasing distance from SS 433 except for regions 3, 6 and 8. This is consistent with the energy-color image shown in Figure 3.3. Table 4.2 summarizes the *Chandra* results for the w2 region in comparison to those of *ROSAT* & *ASCA*.

Table 4.1: Derived model parameters for all regions.

Region	Model	N_H (10^{21} cm^{-2})	Γ or kT (keV)	Luminosity (10^{32} erg/s)	Reduced χ^2 (DOF)
1	PL	$21.6\ ^{+5.1}_{-4.4}$	$1.85\ ^{+0.34}_{-0.30}$	8.10	1.19 (90)
	BREMS	$18.7\ ^{+3.5}_{-3.1}$	$8.98\ ^{+12.93}_{-2.93}$	6.74	1.21 (90)
2	PL	$10.9\ ^{+4.2}_{-3.1}$	$1.69\ ^{+0.38}_{-0.28}$	2.88	0.893 (52)
	BREMS	$9.4\ ^{+2.9}_{-2.5}$	$11.33\ ^{+41.8}_{-4.89}$	2.46	0.922 (52)
3	PL	$10.7\ ^{+2.0}_{-1.5}$	$1.94\ ^{+0.21}_{-0.17}$	12.7	1.09 (182)
	BREMS	$8.8\ ^{+1.4}_{-1.2}$	$6.02\ ^{+2.40}_{-1.49}$	10.4	1.11 (182)
4	PL	$5.6\ ^{+2.0}_{-1.3}$	$1.66\ ^{+0.25}_{-0.22}$	2.81	1.44 (66)
	BREMS	$4.7\ ^{+1.4}_{-1.2}$	$10.51\ ^{+15.96}_{-4.58}$	2.64	1.47 (66)
5	PL	$4.0\ ^{+2.1}_{-1.3}$	$1.34\ ^{+0.23}_{-0.17}$	2.94	1.27 (67)
	BREMS	$3.8\ ^{+0.9}_{-1.3}$	$34.09\ ^{+166}_{-22.7}$	2.82	1.27 (67)
6	PL	$9.8\ ^{+4.6}_{-3.5}$	$1.61\ ^{+0.38}_{-0.28}$	2.44	1.10 (44)
	BREMS	$8.9\ ^{+2.7}_{-3.1}$	$11.45\ ^{+94.9}_{-5.33}$	2.16	1.11 (44)
7	PL	$8.9\ ^{+5.4}_{-3.0}$	$1.86\ ^{+0.55}_{-0.38}$	0.92	1.24 (42)
	BREMS	$7.6\ ^{+4.1}_{-2.3}$	$6.54\ ^{+15.8}_{-2.56}$	0.80	1.24 (42)
8	PL	$13.1\ ^{+3.3}_{-2.7}$	$1.96\ ^{+0.28}_{-0.25}$	4.23	1.13 (55)
	BREMS	$11.1\ ^{+2.4}_{-1.0}$	$5.97\ ^{+3.72}_{-1.78}$	3.42	1.13 (55)
w2[a]	PL	$7.1\ ^{+1.1}_{-0.9}$	$1.88\ ^{+0.14}_{-0.11}$	54.5	1.21 (137)
	BREMS	$5.8\ ^{+0.8}_{-0.7}$	$6.07\ ^{+1.60}_{-1.13}$	45.6	1.21 (137)
Large[a]	PL	$9.6\ ^{+1.5}_{-1.2}$	$1.83\ ^{+0.15}_{-0.12}$	102	1.11 (164)
	BREMS	$8.0\ ^{+1.0}_{-1.0}$	$7.07\ ^{+2.35}_{-1.47}$	86.6	1.12 (164)
IRknot2[a]	PL	$28.0\ ^{+4.5}_{-4.1}$	$2.36\ ^{+0.30}_{-0.28}$	40.4	1.18 (133)
	BREMS	$23.1\ ^{+3.3}_{-2.9}$	$4.22\ ^{+1.59}_{-1.00}$	31.8	1.19 (133)

[a]The background regions used for these source regions are the 6 averaged circular regions, seen in Figure 4.3.

Table 4.2: Thermal Bremsstrahlung and Power-law Model Results for the w2 region

Data Set/ Model	N_H (10^{21} cm^{-2})	Γ or kT (keV)	L_x (10^{33} D_3^2 erg/s)	Reduced χ^2 (DOF)
Chandra				
PL.....	$7.1^{+1.1}_{-0.9}$	$1.88^{+0.14}_{-0.11}$	5.45	1.21 (137)
BREMS...	$5.8^{+0.7}_{-0.7}$	$6.07^{+1.60}_{-1.13}$	4.56	1.21 (137)
ROSAT/ASCA				
PL.....	$5.9^{+2.3}_{-1.9}$	$2.41^{+0.34}_{-0.26}$	5.45	1.41 (95)
BREMS...	$3.5^{+1.6}_{-1.5}$	$3.27^{+1.18}_{-0.77}$	4.23	1.28 (95)

Subsequently, the power-law fits are used to derive the synchrotron emission parameters. Assuming equipartition between particles and fields and integrating from radio to X-ray frequencies, the equipartition magnetic field (B_{eq}), the magnetic energy density ($B_{eq}^2/8\pi$), the total synchrotron electron energy (U_e) and the lifetime of the electrons (τ) can be determined using the following equations.

$$aU_e \approx \frac{VB^2}{8\pi} \tag{4.1}$$

$$U_e = 10^{12}\frac{L}{B^{3/2}}\frac{\nu_2^{1/2+\alpha} - \nu_1^{1/2+\alpha}}{\nu_2^{1+\alpha} - \nu_1^{1+\alpha}}\frac{2\alpha+2}{2\alpha+1} \quad \text{(ergs)} \tag{4.2}$$

$$\alpha = \Gamma - 1 \tag{4.3}$$

$$\tau = \frac{E}{dE/dt} = 1.6B^{-3/2}(G)\nu_c^{-1/2}(GHz) \quad \text{(years)} \tag{4.4}$$

(Lang, 1974) where V is the volume of the source region in cm^3, α is the spectral index, Γ is the photon index, and ν_c is the critical frequency (the frequency at which synchrotron radiation peaks). Table 4.3 summarizes the calculated synchrotron parameters, again using a distance of 3 kpc to the source. The range of values corresponds to a=1-100 (the ratio of baryon energy to electron energy), 100 being typical for cosmic rays (Lang, 1974).

Table 4.3: The calculated synchrotron emission parameters using the results from the power-law model fits.

Region	B_{eq} (10^{-5}G)	$B_{eq}^2/8\pi$ (10^{-12} ergs cm^{-3})	U_e (10^{44} ergs)	τ (10^3 yr)
1	0.53-1.99	1.1-16	0.57-8.0	0.37-2.6
2	0.52-1.94	1.1-15	0.21-3.0	0.38-2.7
3	0.44-1.65	0.78-1.1	1.1-16	0.48-3.5
4	0.47-1.77	0.90-12	0.24-3.3	0.44-3.1
5	0.50-1.86	1.0-14	0.27-3.7	0.40-2.9
6	0.56-2.07	1.2-17	0.17-2.4	0.35-2.5
7	0.52-1.93	1.1-15	0.07-0.94	0.38-2.8
8	0.66-2.44	1.7-24	0.22-3.1	0.27-1.9
w2	0.26-0.98	0.28-3.8	11-155	1.1-7.6
Large	0.23-0.84	0.20-2.8	27-369	1.3-9.5
IRknot2	0.28-1.06	0.32-4.5	7.3-101	0.94-6.8

The derived values of the synchrotron parameters as well as N_H for the w2 region (Table 4.2) agree with those found using *ROSAT* and *ASCA*, within error. However, the spectra appear harder with the *Chandra* observation.

4.3.3 Correlation with Radio and Infrared

To probe the interaction between the western jet of SS 433 and the ambient medium, the X-ray emission is studied in correlation with radio continuum and HI data obtained with the NRAO[1] VLA and Green-Bank radio telescope and infrared data obtained with *ISOCAM*. Fig 4.1 shows the radio, infrared, and X-ray regions and Figure 4.4 shows the X-ray emission with the infrared contours.

The average value of N_H found on the basis of the HI observations is $\sim$ (4 –

[1]The NRAO is a facility of the NSF operated under a cooperative agreement by Associated Universities Inc.

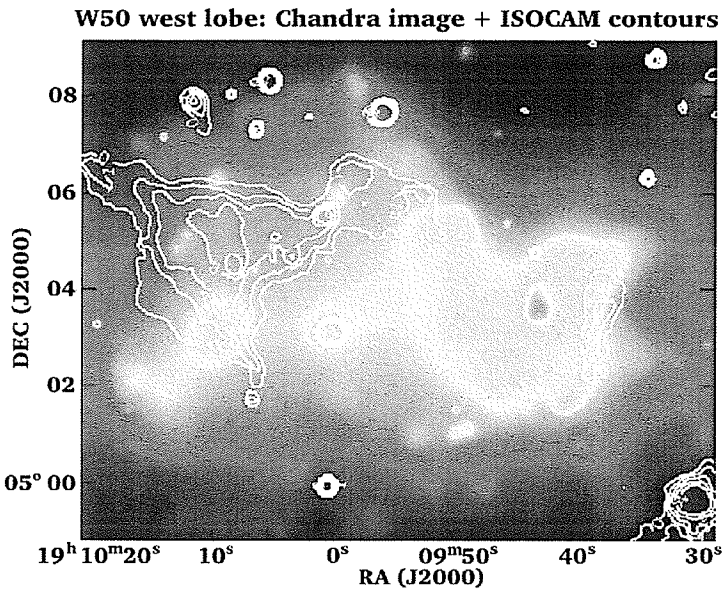

Figure 4.4: X-ray image of the western lobe shown with the infrared contours.

4.4) $\times 10^{21}$ cm^{-2}. This is slightly lower than the average found using the *Chandra* data, which is to be expected.

The energetics in the western lobe found with the X-ray data can then be compared to that found in Dubner et al. (1998). The total synchrotron electron energy is found in X-rays to be $\sim 2.5 \times 10^{45} - 3.5 \times 10^{46}$ ergs, which is in good agreement with the energy found from radio observations.

As seen in Figure 4.4, there is no correlation between the infrared emission and the peak of X-ray emission. This, along with the high value of N_H ($N_H \geq 2 \times 10^{22}$ cm^{-2}) derived for the IRknot2 region using the *Chandra* data, suggests that the infrared emission is not associated with the western lobe of W50. The derived value of $kT \geq 4.2$ keV is higher than the expected temperatures for SNRs, indicating that the X-ray emission in IRknot2 is non-thermal.

4.3.4 Point Sources

In the *Chandra* thread that was used to create the morphological image of the western lobe of W50, the WAVDETECT tool was used to detect 43 possible point sources in the *Chandra* field of view. These point sources are listed in Table 4.4 with the J2000 coordinates in degrees, the number of counts in the 0.3-2.4 keV (soft X-ray) and 2.4-10 keV (hard X-ray) energy ranges, and the signal-to-noise (S/N) ratio. Looking these up in Simbad, an astronomical database, only three of the point sources have known counterparts: source 1 is GSC 00471-00860, and is a star of unknown spectral class; source 8 is BD+04 3996 and is an A2 type star; source 25 is Zel 1907+050 and is a radio source.

Table 4.4: Point Sources

Source	RA (J2000)	DEC (J2000)	soft[a] Cnts	hard[b] Cnts	S/N	Source	RA (J2000)	DEC (J2000)	soft[a] Cnts	hard[b] Cnts	S/N
1	287.5587	5.0272	1802	68	30	23	287.4299	5.0488	6	5	2.3
2	287.4499	5.0415	76	16	6.5	24	287.4088	5.0627	3	3	1.7
3	287.4434	5.0663	15	14	3.4	25	287.4083	5.1044	15	39	4.7
4	287.4415	5.0403	2	3	1.6	26	287.4061	5.0147	13	3	2.6
5	287.433	5.0659	112	159	12	27	287.4026	5.0852	14	13	2.8
6	287.4103	5.0446	8	0	1.9	28	287.3992	5.0015	23	3	3.3
7	287.4022	4.9889	50	2	4.9	29	287.3985	5.0431	3	4	1.8
8	287.5053	5.0395	30	0	3.4	30	287.3967	5.0495	7	18	3.2
9	287.5035	5.0925	21	49	5.3	31	287.396	5.0114	20	16	4.2
10	287.5012	5.032	16	5	2.5	32	287.3907	5.0935	13	16	3.3
11	287.4988	5.0285	40	12	4.5	33	287.3739	5.0321	22	4	3.4
12	287.4917	5.0073	1	21	3.2	34	287.5808	5.0741	55	80	6.2
13	287.4794	5.0325	5	2	1.7	35	287.5677	5.1168	16	25	3.7
14	287.4757	5.0749	15	1	2.2	36	287.5248	5.0913	49	21	4.7
15	287.4672	5.0294	15	5	2.9	37	287.5079	5.0504	11	12	2.5
16	287.4624	4.9855	9	2	2.2	38	287.4992	5.0753	21	8	3
17	287.4549	4.9902	26	9	4.1	39	287.4575	5.0158	4	11	2.2
18	287.4454	5.0244	8	8	2.4	40	287.4387	5.1425	37	18	4.1
19	287.44	4.9854	2	13	2.6	41	287.4127	5.0013	4	3	1.5
20	287.4377	5.0024	10	1	2	42	287.3998	5.1123	11	12	2.6
21	287.437	5.1178	36	8	4.2	43	287.3729	5.1118	5	17	2.5
22	287.4368	5.0568	6	6	2.3						

[a]0.3-2.4 keV energy range; [b]2.4-10 keV energy range

The number of counts for the two energy ranges were found using the DMCOPY, DMEXTRACT and DMLIST tools. First, two new Level 2 event files were produced with DMCOPY by selecting the energy ranges noted above. Then, DMEXTRACT is used to form one FITS file from the region files of the sources and of the backgrounds. The DMLIST tool can be used to get a list of the counts for each region. The S/N ratio was found using the equation:

$$S/N = \frac{S}{\sqrt{S+B}} \tag{4.5}$$

where S is the source counts and B is the background counts.

Spectra were extracted for all point sources with total counts ≥ 100 (points 1, 2, 5 and 34 in Table 4.4). Background regions were created for each of these by selecting an ellipse around the point source region and then excluding the point source.

Using the CIAO 3.0 thread "Step-by-Step Guide to Creating ACIS Spectra for Point Sources" (available from http://cxc.harvard.edu/ciao/threads/pieces/), spectra were obtained for the four point sources. The tools used in this thread are DMEXTRACT (to extract the spectra), DMSTAT (to find the chip and sky centroids, as well as the CCD ID), ACIS_FEF_LOOKUP (to select the proper Fits Embedded Function (FEF)), MKRMF (to create the response matrix file (RMF)), ASPHIST (to bin the aspect solution (ASOL) file), MKARF (to create the auxiliary response file (ARF)), DMGROUP (to group the bins in the spectra file), and DMHEDIT (to edit the headers of the spectra files).

After the spectra are extracted, each point source was fitted by bremsstrahlung, power-law, blackbody, and Raymond-Smith models, along with a two-component bremsstrahlung & blackbody model in XSPEC. Both the bremsstrahlung and power-

law models have been described above and the mechanisms are detailed in Appendix A. The blackbody model is a blackbody spectrum characterized by the temperature, kT (see Appendix A for more information). The Raymond-Smith model is an emission spectrum from a hot diffuse gas based on the model calculations by Raymond & Smith (1977), including line emission from many elements. It is characterized by the plasma temperature, kT, the redshift, z, and the metal abundances (typically frozen to the cosmic abundance - for every 10,000 atoms of hydrogen, the gas contains 800 atoms of helium and 16 atoms of carbon, oxygen, and heavier elements).

Table 4.5 summarizes the best fit model for each point source with counts $\geq$100. The error bars are at the 90% level. The results indicate that point sources 1 and 5 are thermal in nature, whereas the sources 2 and 34 seem to be non-thermal. To unveil the true nature of these, and other point sources in the field, multi-wavelength observations with deeper exposures are needed.

Table 4.5: Results for the best fit model for point sources having $\geq$ 100 counts.

Source	Model Range (keV)	N_H (10^{22} cm^{-2})	Model Parameter	Unabs. Flux (erg cm^{-2}s^{-1})	Reduced χ^2 (DOF)
1	BB+BREMS	$0.620^{+0.22}_{-0.01}$	$kT_1 = 0.971^{+0.22}_{-0.45}$	3.02×10^{-12}	1.52 (91)
	0.5-10		$kT_2 = 0.097^{+0.002}_{-0.02}$		
2	PL	$0.233^{+0.59}_{-0.23}$	$\Gamma = 2.15^{+1.8}_{-1.1}$	1.40×10^{-14}	0.269 (12)
	0.5-5.0				
5	BB+BREMS	$1.46^{+4.0}_{-0.63}$	$kT_1 = 0.637^{+0.02}_{-0.50}$	1.43×10^{-13}	0.748 (45)
	0.5-9.5		$kT_2 = 1.35^{+1.1}_{-0.38}$		
34	PL	$0.879^{+4.5}_{-0.88}$	$\Gamma = 1.57^{+3.7}_{-1.3}$	2.85×10^{-14}	0.975 (22)
	0.5-10				

4.4 Discussion

From this study, a non-thermal interpretation is favored for the emission of the western lobe of W50. The derived values of N_H, equipartition magnetic field, synchrotron electron energies and lifetimes agree with those derived previously by Safi-Harb & Ögelman (1997) with *ROSAT* and *ASCA*.

The infrared emission is not correlated with the peak of X-ray emission. This, in addition to the high value of N_H derived for this region, suggests that the infrared emission is not originating from W50, and could be associated with a star forming region.

The corkscrew pattern seen in both the radio and X-ray images provides strong support to the hypothesis that the relativistic jets from SS 433 are causing the morphology of the W50 nebula.

43 point sources have been resolved in the *Chandra* field indicating that previous X-ray studies of the W50 nebula were confused. Only three sources have known counterparts. The hardness of all sources were characterized and spectra were extracted from four sources which had a sufficient number of counts for spectral analysis. However, multi-wavelength observations are needed to unveil their nature.

Chapter 5

The *RXTE* Study of SS 433

5.1 Introduction

RXTE is an invaluable satellite in the energy range between the *Chandra* X-ray observatory (i.e. ~0.5-10 keV) and the gamma-ray observatory, *INTEGRAL*, which observes up to energies of 100 keV. The *HEXTE* instrument on board *RXTE* is specifically designed to observe in the 15-250 keV range, having its best resolution at ~60 keV.

SS 433 is a unique Galactic X-ray binary system, and is classified as a microquasar that is expelling highly collimated jets at 0.26c. This system exhibits two major periodicities: the binary orbital period ($P_b = 13.082$ days) and the precessional period of the jets ($P_p = 162.15$ days). Recent optical and UV spectral observations (Gies et al., 2002), X-ray observations (H. Marshall 2005, private communication) and gamma-ray observations (Cherepashchuk et al., 2003) all indicate that the compact object in the binary system is a black hole (although the derived masses are in discrepancy).

This thesis presents the first complete *RXTE* spectroscopic study of the SS 433 X-ray binary system up to ~70 keV (smaller studies have been published by Kotani et al. (2002), Safi-Harb & Kotani (2002), and Safi-Harb & Kotani (2002)). The purpose is to determine the nature of the hard X-ray emission from the binary system, and to correlate the spectral parameters with the binary phase and observed radio flares.

5.2 Observations and Data Reduction

Archived *RXTE* observations of the SS 433 X-ray binary were downloaded from the *HEASARC*[1] database spanning the years of 1996-2004, and covering all precessional phases except $\psi \sim 0.1$-0.4. When $\psi \sim 0$, the eastern jet is pointing toward us, and the shifted lines are at a maximum separation (see Figure 2.3). Data reduction was performed using the standard techniques for both the *PCA* and *HEXTE* data, as outlined in Chapter 3 and Appendix C. In all, there were 78 observations with good data (i.e. at least one model has an acceptable value of reduced χ^2) in 7 different observation sets, with durations ranging from 0.24-28.8 ks (see Tables 5.1-5.7) for a total observation time of ~ 609 ks.

5.3 Spectral Analysis & Results

The *RXTE* spectra were fitted with thermal bremsstrahlung and power-law models, both with one and two Gaussian lines (referred to as B+G, B+2G, PL+G and PL+2G hereafter). The thermal model is characterized by the shock temperature, kT, and is associated with bremsstrahlung radiation. The power-law model is characterized by the photon index, Γ, and is associated with synchrotron radiation. For details of these emission mechanisms, see Appendix A. These models have been used in previous studies (i.e. Safi-Harb & Kotani, 2002; Cherepashchuk et al., 2003; Brinkmann, Kotani & Kawai, 2005), with B+2G being dubbed as the 'traditional' model of SS 433, and PL+2G being used at high energies to determine if the compact object is a black hole (the spectra of which have power-law tails up to 100s of keV).

[1] http://heasarc.gsfc.nasa.gov

The Gaussian lines are added to the models because, from previous studies (Marshall et al., 1979; Kotani, 1996) there are lines visible in the spectra at ~7 keV that are due to either Fe XXV (6.684 keV), Fe XXVI (7.058 keV) or the Fe **fluorescence** line (6.399 keV). Which of these are observed depends on the orientation of the system. The Fe fluorescence line is stationary, and Kotani (1996) suggests that it originates from the accretion disk. Thus, this line can only be seen when the eastern jet (see Figure 2.3) is pointed away from the observer (i.e. $\psi \sim 0.5$). During other phases, especially near $\psi \sim 0$, it is expected that the shifted Fe lines from the jets will be observed.

The value of N_H was allowed to vary between (0.7-2.4)$\times 10^{22}$ cm^{-2} (the lowest and highest observed values in the literature). If *HEXTE* data was used, the normalization factor for the *HEXTE* spectra was also allowed to vary. The *PCA* spectra were fitted over an energy range from 3 keV to a maximum energy that varies for each observation. This cut-off energy was chosen by observing where the spectra became dominated by the background (i.e. the signal-to-noise ratio was low). Only the top layer data (see sections 3.2.1 and 3.2.3) were used to maximize the signal-to-noise ratio. The energy used for the *HEXTE* spectra was from 15 keV to a maximum energy that varies for each observation (as for *PCA* spectra). Only the cluster 0 data for the *HEXTE* spectra was used, as cluster 1 has lost some spectral capabilities in one of its detectors (see section 3.2.2)

In most cases, the spectra were best fit by either the B+2G or PL+2G models, having one narrow and one broad Gaussian line, both centered at ~7 keV (see next two sections for explanation). Although this indicates the emission may be due to both thermal and non-thermal mechanisms, the data could not be fit by a B+PL+2G

model (for example). This is because the number of free parameters and the low count rates would allow for a wide variety of acceptable values, and thus would not easily constrain the model.

Figure 5.1 shows example fits of the B+2G and PL+2G models. For an explanation of the difference between these two model fits, see Appendix A. Only two out of the 78 observations were fit better with a PL+G model, while only one was best fit with a B+G model. Tables 5.1-5.7 summarize the best fit model parameters for the observations in each data set. The luminosities are calculated at a distance of 3 kpc (scaled by $D_3{}^2$), as explained in section 2.1.6.

[2] D_3 denotes the distance in units of 3 kpc

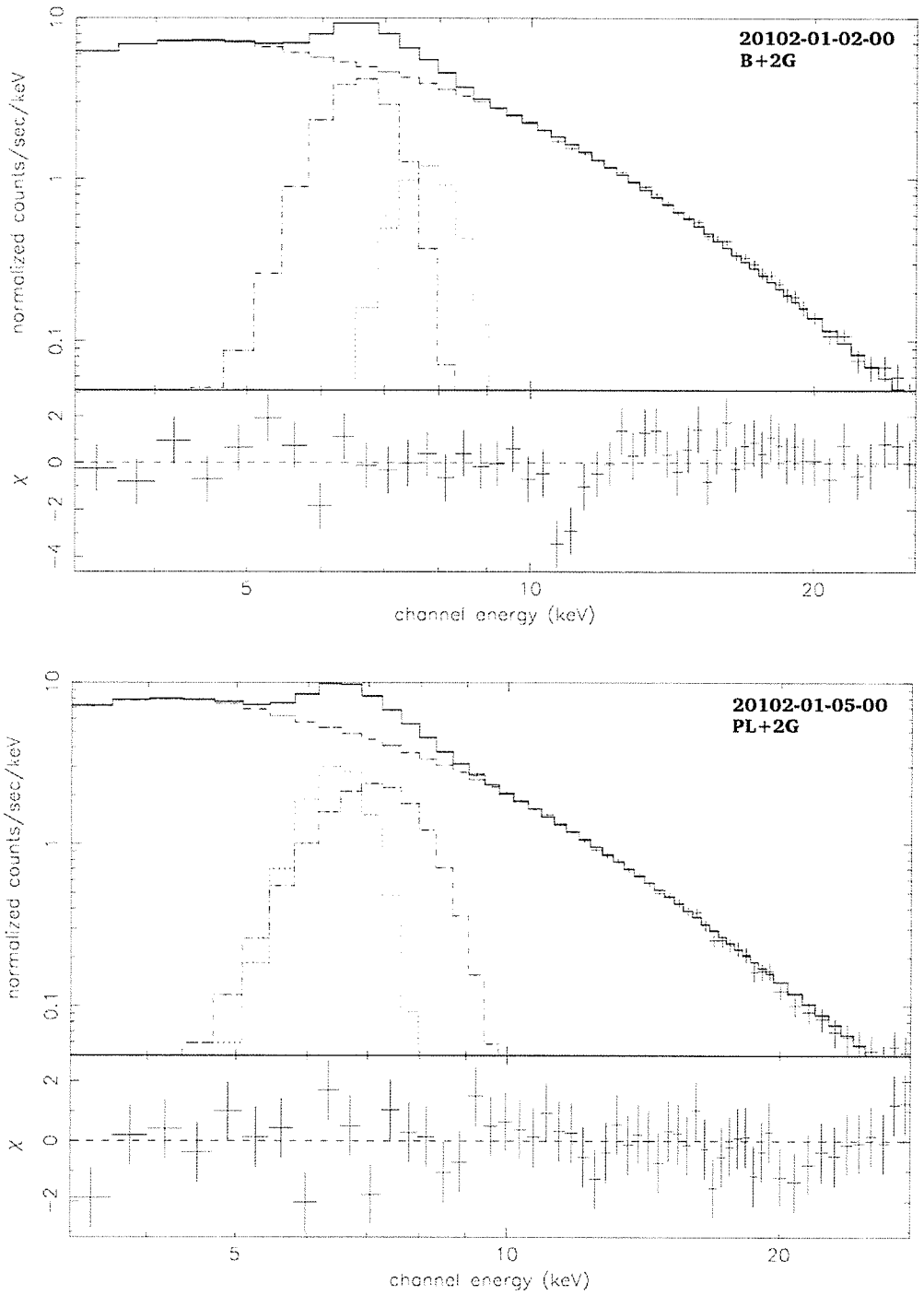

Figure 5.1: Example model fits, showing each model component, with residuals for B+2G (top) and PL+2G (bottom) models for two different *RXTE* observations. The two 'humps' (dotted, and dotted-dashed lines) are the Gaussian line fits, while the dashed line is either the bremsstrahlung or power-law fits. The solid line is the total model (either B+2G or PL+2G), and the data are crosses.

Table 5.1: *RXTE* best fit model parameters for the 10127 observation set.
Error bars are at the 90% confidence level.

OBS-ID	ϕ	N_H (10^{21} cm^{-2})	En. Range(s) (keV)	kT (keV)	Line E_1	σ_1	Total Lum.	Red. χ^2 (DOF)
JD-2,450,000	ψ	Model	*HEXTE* Cons.	or Γ	Line E_2 (keV)	σ_2 (keV)	(10^{35} D_3^2 erg/s)	Duration (ks)
10127-01-02-00	0.917	$2.40^{+0.0}_{-0.3}$	3-25	$1.98^{+0.01}_{-0.01}$	$6.82^{+0.04}_{-0.04}$	$0.29^{+0.13}_{-0.21}$	3.7	1.49 (43)
192.61	0.195	PL+2G			$7.07^{+0.08}_{-0.08}$	$1.16^{+0.10}_{-0.07}$		13.1
10127-01-03-00	0.964	$0.97^{+0.4}_{-0.2}$	3-24	$11.05^{+0.20}_{-0.44}$	$6.82^{+0.04}_{-0.04}$	$0.03^{+0.20}_{-0.03}$	2.7	1.49 (42)
193.21	0.199	B+2G			$6.69^{+0.10}_{-0.11}$	$0.59^{+0.05}_{-0.05}$		8.25
10127-01-05-00	0.007	$2.31^{+1.2}_{-1.4}$	3-17	$2.10^{+0.22}_{-0.27}$	$6.91^{+0.38}_{-0.60}$	$1.28^{+0.57}_{-0.22}$	2.4	0.915 (29)
193.77	0.203	PL+2G			$6.93^{+0.95}_{-0.20}$	$0.01^{+4.73}_{-0.00}$		11.0
10127-01-06-00	0.045	$0.98^{+0.2}_{-0.6}$	3-23	$11.30^{+0.76}_{-0.11}$	$6.85^{+0.32}_{-0.09}$	$0.01^{+0.16}_{-0.01}$	2.7	1.91 (41)
194.27	0.206	B+2G			$6.96^{+0.00}_{-0.09}$	$0.97^{+0.12}_{-0.03}$		9.20

Table 5.2: *RXTE* best fit model parameters for the 20102 observation set.
Error bars are at the 90% confidence level.

OBS-ID	ϕ	N_H (10^{21} cm^{-2})	En. Range(s) (keV)	kT (keV)	Line E_1	σ_1	Total Lum.	Red. χ^2 (DOF)
JD-2,450,000	ψ	Model	*HEXTE* Cons.	or Γ	Line E_2 (keV)	σ_2 (keV)	(10^{35} D_3^2 erg/s)	Duration (ks)
20102-01-01-00	0.643	$2.40^{+0.0}_{-0.3}$	3-30	$1.70^{+0.01}_{-0.02}$	$7.11^{+0.12}_{-0.08}$	$0.73^{+0.08}_{-0.07}$	3.1	1.02 (49)
869.28	0.369	PL+2G			$6.52^{+0.05}_{-0.03}$	$0.01^{+0.11}_{-0.00}$		16.3
20102-01-02-00	0.755	$1.74^{+0.3}_{-0.3}$	3-26	$22.04^{+1.18}_{-1.08}$	$6.57^{+0.02}_{-0.05}$	$0.21^{+0.05}_{-0.13}$	3.0	1.21 (44)
870.75	0.378	B+2G			$7.71^{+0.08}_{-0.05}$	$0.01^{+0.30}_{-0.00}$		16.7

Table 5.2: 20102 Set Cont.

OBS-ID	ϕ	N_H (10^{21} cm^{-2})	En. Range(s) (keV)	kT (keV)	Line E_1	σ_1	Total Lum.	Red. χ^2 (DOF)
JD-2450000	ψ	Model	*HEXTE* Cons.	or Γ	Line E_2 (keV)	σ_2 (keV)	(10^{35} D_3^2 erg/s)	Duration (ks)
20102-01-03-00	0.883	$2.40^{+0.0}_{-0.1}$	3-30	$1.73^{+0.01}_{-0.01}$	$6.54^{+0.03}_{-0.02}$	$0.01^{+0.09}_{-0.00}$	3.8	1.86 (49)
872.42	0.388	PL+2G			$7.05^{+0.07}_{-0.04}$	$0.85^{+0.05}_{-0.05}$		16.5
20102-01-04-00	0.980	$0.98^{+0.3}_{-0.3}$	3-25	$11.89^{+0.42}_{-0.40}$	$7.69^{+0.12}_{-0.22}$	$0.23^{+0.20}_{-0.23}$	2.4	1.10 (43)
873.68	0.396	B+2G			$6.54^{+0.04}_{-0.06}$	$0.19^{+0.07}_{-0.13}$		14.3
20102-01-05-00	0.112	$2.40^{+0.0}_{-0.2}$	3-28	$1.90^{+0.01}_{-0.02}$	$7.11^{+0.11}_{-0.06}$	$0.72^{+0.06}_{-0.08}$	3.2	0.812 (47)
875.42	0.406	PL+2G			$6.46^{+0.03}_{-0.01}$	$0.10^{+0.02}_{-0.09}$		15.3
20102-01-06-00	0.251	$1.45^{+1.5}_{-1.5}$	3-24	$1.89^{+0.10}_{-0.11}$	$6.92^{+0.32}_{-0.24}$	$0.89^{+0.26}_{-0.23}$	2.7	0.689 (41)
877.23	0.418	PL+2G			$6.54^{+0.06}_{-0.08}$	$0.01^{+1.15}_{-0.00}$		2.51
20102-01-07-00	0.245	$0.90^{+0.6}_{-0.6}$	3-23	$1.99^{+0.06}_{-0.04}$	$7.46^{+0.96}_{-0.55}$	$0.60^{+0.53}_{-0.60}$	0.93	0.551 (40)
890.24	0.498	PL+2G			$6.58^{+0.16}_{-0.14}$	$0.23^{+0.39}_{-0.23}$		21.2
20102-02-01-00	0.422	$2.40^{+0.0}_{-0.2}$	3-34	$1.87^{+0.01}_{-0.01}$	$7.12^{+0.09}_{-0.14}$	$0.92^{+0.07}_{-0.08}$	3.7	1.01 (55)
879.47	0.431	PL+2G			$6.62^{+0.03}_{-0.04}$	$0.27^{+0.04}_{-0.17}$		18.0
20102-02-01-01	0.332	$2.40^{+0.0}_{-0.2}$	3-31	$1.83^{+0.00}_{-0.02}$	$6.96^{+0.07}_{-0.04}$	$0.83^{+0.05}_{-0.05}$	3.6	1.21 (51)
878.29	0.424	PL+2G			$6.57^{+0.03}_{-0.04}$	$0.03^{+0.15}_{-0.03}$		17.9
20102-02-01-02	0.256	$2.40^{+0.0}_{-0.9}$	3-20	$1.92^{+0.02}_{-0.07}$	$7.09^{+0.60}_{-0.15}$	$0.72^{+0.14}_{-0.35}$	2.7	0.551 (36)
877.30	0.418	PL+2G			$6.48^{+0.06}_{-0.08}$	$0.10^{+0.77}_{-0.09}$		2.45
20102-02-01-03	0.316	$2.38^{+1.1}_{-0.9}$	3-22	$1.94^{+0.08}_{-0.06}$	$7.05^{+0.36}_{-0.12}$	$0.84^{+0.21}_{-0.15}$	2.7	0.685 (39)
878.08	0.423	PL+2G			$6.53^{+0.12}_{-0.09}$	$0.01^{+0.33}_{-0.00}$		2.99
20102-02-01-04	0.321	$1.70^{+0.6}_{-0.7}$	3-20	$14.40^{+1.33}_{-1.28}$	$7.73^{+0.30}_{-0.78}$	$0.31^{+0.55}_{-0.31}$	2.6	0.981 (36)
878.15	0.423	B+2G			$6.57^{+0.07}_{-0.18}$	$0.24^{+0.11}_{-0.24}$		3.41
20102-02-01-05	0.326	$2.40^{+0.0}_{-0.3}$	3-23	$1.91^{+0.02}_{-0.03}$	$7.11^{+0.92}_{-0.11}$	$0.80^{+0.11}_{-0.54}$	2.9	0.974 (40)
878.22	0.424	PL+2G			$6.50^{+0.06}_{-0.08}$	$0.11^{+0.25}_{-0.11}$		3.47

Table 5.2: 20102 Set Cont.

OBS-ID	ϕ	N_H (10^{21} cm^{-2})	En. Range(s) (keV)	kT (keV)	Line E_1	σ_1	Total Lum.	Red. χ^2 (DOF)
JD-2450000	ψ	Model	*HEXTE* Cons.	or Γ	Line E_2 (keV)	σ_2 (keV)	(10^{35} D_3^2 erg/s)	Duration (ks)
20102-02-01-060	0.348	$2.40\ ^{+0.0}_{-0.0}$	3-34	$1.84\ ^{+0.00}_{-0.02}$	$6.99\ ^{+0.07}_{-0.03}$	$0.93\ ^{+0.05}_{-0.04}$	3.9	1.48 (55)
878.50	0.425	PL+2G			$6.59\ ^{+0.02}_{-0.02}$	$0.10\ ^{+0.10}_{-0.10}$		28.8
20102-02-01-07	0.392	$1.87\ ^{+0.5}_{-1.0}$	3-24	$17.50\ ^{+1.50}_{-1.72}$	$6.62\ ^{+0.04}_{-0.09}$	$0.00\ ^{+0.26}_{-0.00}$	3.2	0.685 (41)
879.08	0.429	B+2G			$6.95\ ^{+0.24}_{-0.13}$	$0.82\ ^{+0.19}_{-0.10}$		2.67
20102-02-01-08	0.453	$2.30\ ^{+1.6}_{-1.7}$	3-17	$1.94\ ^{+0.11}_{-0.11}$	$7.14\ ^{+0.96}_{-0.16}$	$0.78\ ^{+0.21}_{-0.78}$	2.5	0.911 (28)
879.88	0.434	PL+2G			$6.46\ ^{+0.10}_{-0.08}$	$0.01\ ^{+0.55}_{-0.00}$		1.49
20102-02-01-09	0.464	$2.21\ ^{+1.2}_{-1.3}$	3-21	$2.03\ ^{+0.08}_{-0.09}$	$7.31\ ^{+0.70}_{-0.36}$	$0.69\ ^{+0.25}_{-0.50}$	2.6	0.612 (37)
880.02	0.435	PL+2G			$6.49\ ^{+0.08}_{-0.09}$	$0.22\ ^{+0.72}_{-0.22}$		1.89
20102-02-01-10	0.469	$2.40\ ^{+0.0}_{-0.5}$	3-24	$2.03\ ^{+0.02}_{-0.03}$	$7.57\ ^{+0.40}_{-0.54}$	$0.75\ ^{+0.26}_{-0.21}$	2.8	0.853 (41)
880.09	0.435	PL+2G			$6.60\ ^{+0.04}_{-0.07}$	$0.35\ ^{+0.05}_{-0.22}$		10.7
20102-02-01-11	0.443	$2.40\ ^{+0.0}_{-0.2}$	3-23	$1.89\ ^{+0.02}_{-0.02}$	$7.90\ ^{+0.33}_{-0.91}$	$0.40\ ^{+0.42}_{-0.40}$	2.9	1.12 (40)
879.75	0.433	PL+2G			$6.61\ ^{+0.08}_{-0.13}$	$0.38\ ^{+0.09}_{-0.38}$		4.10
20102-02-02-00	0.937	$2.40\ ^{+0.0}_{-0.1}$	3-27	$2.03\ ^{+0.01}_{-0.01}$	$7.05\ ^{+0.07}_{-0.05}$	$0.82\ ^{+0.06}_{-0.06}$	3.0	1.59 (45)
899.29	0.554	PL+2G			$6.49\ ^{+0.04}_{-0.03}$	$0.01\ ^{+0.14}_{-0.00}$		17.4
20102-02-02-01	0.866	$2.35\ ^{+0.6}_{-0.3}$	3-27	$1.97\ ^{+0.04}_{-0.04}$	$6.49\ ^{+0.04}_{-0.04}$	$0.06\ ^{+0.22}_{-0.06}$	3.0	0.486 (45)
898.36	0.548	PL+2G			$7.15\ ^{+0.48}_{-0.18}$	$0.80\ ^{+0.10}_{-0.23}$		8.08

Table 5.3: *RXTE* best fit model parameters for the 30273 observation set.
Error bars are at the 90% confidence level.

OBS-ID	ϕ	N_H (10^{21} cm^{-2})	En. Range(s) (keV)	kT (keV)	Line E_1	σ_1	Total Lum.	Red. χ^2 (DOF)
JD-2,450,000	ψ	Model	*HEXTE* Cons.	or Γ	Line E_2 (keV)	σ_2 (keV)	(10^{35} D_3^2 erg/s)	Duration (ks)
30273-01-01-00	0.008	$0.70\ ^{+0.2}_{-0.0}$	3-24	$10.56\ ^{+0.18}_{-0.23}$	$7.46\ ^{+0.19}_{-0.25}$	$0.43\ ^{+0.16}_{-0.15}$	2.2	1.60 (41)
900.22	0.559	B+2G			$6.48\ ^{+0.02}_{-0.04}$	$0.11\ ^{+0.08}_{-0.11}$		19.8
30273-01-01-01	0.085	$2.40\ ^{+0.0}_{-0.1}$	3-28	$1.86\ ^{+0.01}_{-0.01}$	$6.99\ ^{+0.17}_{-0.02}$	$0.79\ ^{+0.05}_{-0.06}$	3.00	0.920 (47)
901.23	0.566	PL+2G			$6.51\ ^{+0.03}_{-0.03}$	$0.00\ ^{+0.14}_{-0.00}$		25024
30273-01-02-00	0.163	$2.40\ ^{+0.0}_{-0.2}$	3-26	$1.83\ ^{+0.01}_{-0.02}$	$7.04\ ^{+0.16}_{-0.08}$	$0.77\ ^{+0.06}_{-0.06}$	3.2	1.05 (44)
902.25	0.572	PL+2G			$6.52\ ^{+0.04}_{-0.04}$	$0.11\ ^{+0.14}_{-0.11}$		20.4
30273-01-02-01	0.264	$2.04\ ^{+1.6}_{-0.5}$	3-23	$1.83\ ^{+0.06}_{-0.04}$	$7.87\ ^{+0.57}_{-0.68}$	$0.57\ ^{+0.51}_{-0.57}$	3.4	0.453 (40)
903.57	0.580	PL+2G			$6.63\ ^{+0.11}_{-0.11}$	$0.37\ ^{+0.45}_{-0.36}$		1.99
30273-01-02-010	0.240	$2.40\ ^{+0.0}_{-0.1}$	3-34	$1.88\ ^{+0.01}_{-0.01}$	$7.06\ ^{+0.17}_{-0.08}$	$0.84\ ^{+0.06}_{-0.06}$	3.8	0.915 (55)
903.25	0.578	PL+2G			$6.56\ ^{+0.03}_{-0.03}$	$0.21\ ^{+0.10}_{-0.12}$		27.3
30273-01-02-02	0.146	$2.35\ ^{+0.4}_{-0.6}$	3-25	$1.83\ ^{+0.03}_{-0.04}$	$7.18\ ^{+0.44}_{-0.10}$	$0.64\ ^{+0.10}_{-0.27}$	3.1	0.852 (43)
902.02	0.570	PL+2G			$6.43\ ^{+0.04}_{-0.03}$	$0.01\ ^{+0.23}_{-0.01}$		9.22
30273-01-03-00	0.335	$2.40\ ^{+0.0}_{-0.9}$	3-22	$1.89\ ^{+0.02}_{-0.06}$	$7.06\ ^{+0.14}_{-0.09}$	$0.93\ ^{+0.16}_{-0.11}$	3.1	1.00 (39)
904.50	0.586	PL+2G			$6.61\ ^{+0.04}_{-0.07}$	$0.01\ ^{+0.85}_{-0.00}$		5.71
30273-01-03-01	0.412	$2.40\ ^{+0.0}_{-0.3}$	3-23	$1.93\ ^{+0.02}_{-0.02}$	$7.18\ ^{+0.66}_{-0.12}$	$0.68\ ^{+0.12}_{-0.68}$	3.0	0.837 (40)
905.50	0.592	PL+2G			$6.49\ ^{+0.06}_{-0.05}$	$0.01\ ^{+0.26}_{-0.00}$		5.38
30273-01-03-010	0.391	$2.40\ ^{+0.0}_{-0.1}$	3-25	$1.91\ ^{+0.01}_{-0.01}$	$7.04\ ^{+0.07}_{-0.03}$	$0.81\ ^{+0.04}_{-0.04}$	3.2	1.86 (43)
905.22	0.590	PL+2G			$6.52\ ^{+0.01}_{-0.03}$	$0.01\ ^{+0.07}_{-0.00}$		23.6
30273-01-03-02	0.428	$2.40\ ^{+0.0}_{-1.2}$	3-20	$1.90\ ^{+0.03}_{-0.08}$	$6.91\ ^{+0.17}_{-0.08}$	$0.82\ ^{+0.18}_{-0.13}$	2.9	0.808 (36)
905.71	0.593	PL+2G			$6.53\ ^{+0.08}_{-0.10}$	$0.01\ ^{+0.27}_{-0.00}$		1.86
30273-01-04-000	0.463	$2.40\ ^{+0.0}_{-0.1}$	3-30	$1.88\ ^{+0.01}_{-0.01}$	$7.15\ ^{+0.06}_{-0.07}$	$0.73\ ^{+0.06}_{-0.04}$	3.4	1.68 (49)

Table 5.3: 30273 Set Cont.

OBS-ID	ϕ	N_H (10^{21} cm^{-2})	En. Range(s) (keV)	kT (keV)	Line E_1	σ_1	Total Lum.	Red. χ^2 (DOF)
JD-2450000	ψ	Model	*HEXTE* Cons.	or Γ	Line E_2 (keV)	σ_2 (keV)	(10^{35} D_3^2 erg/s)	Duration (ks)
906.17	0.596	PL+2G			$6.45\ ^{+0.03}_{-0.01}$	$0.01\ ^{+0.07}_{-0.00}$		28.6
30273-01-05-01	0.488	$2.40\ ^{+0.0}_{-0.2}$	3-28	$1.85\ ^{+0.02}_{-0.02}$	$7.65\ ^{+0.23}_{-0.55}$	$0.36\ ^{+0.36}_{-0.36}$	3.4	0.950 (47)
906.50	0.598	PL+2G			$6.51\ ^{+0.06}_{-0.07}$	$0.17\ ^{+0.10}_{-0.17}$		7.79
30273-01-05-02	0.575	$2.18\ ^{+1.4}_{-1.7}$	3-22	$1.89\ ^{+0.04}_{-0.11}$	$7.02\ ^{+0.25}_{-0.23}$	$0.97\ ^{+0.23}_{-0.17}$	3.0	0.827 (39)
907.64	0.605	PL+2G			$6.51\ ^{+0.05}_{-0.06}$	$0.01\ ^{+1.03}_{-0.00}$		1.94
30273-01-05-03	0.499	$1.60\ ^{+0.8}_{-0.9}$	3-20	$15.61\ ^{+2.63}_{-1.57}$	$7.44\ ^{+0.34}_{-0.51}$	$0.36\ ^{+0.37}_{-0.36}$	2.7	0.784 (36)
906.64	0.599	B+2G			$6.49\ ^{+0.03}_{-0.11}$	$0.16\ ^{+0.15}_{-0.16}$		2.18

Table 5.4: *RXTE* best fit model parameters for the 40146 observation set.

Error bars are at the 90% confidence level.

OBS-ID	ϕ	N_H (10^{21} cm^{-2})	En. Range(s) (keV)	kT (keV)	Line E_1	σ_1	Total Lum.	Red. χ^2 (DOF)
JD-2,450,000	ψ	Model	*HEXTE* Cons.	or Γ	Line E_2 (keV)	σ_2 (keV)	(10^{35} D_3^2 erg/s)	Duration (ks)
40146-01-01-03R	0.013	$0.70\ ^{+3.9}_{-0.0}$	3-14	$2.04\ ^{+2.43}_{-0.15}$	$5.84\ ^{+4.16}_{-0.84}$	$0.25\ ^{+1.75}_{-0.24}$	2.3	0.452 (16)
1292.74	0.980	PL+2G			$7.36\ ^{+0.86}_{-0.56}$	$0.89\ ^{+1.11}_{-0.88}$		2.69
40146-01-01-07R	0.022	$2.40\ ^{+0.0}_{-2.4}$	3-13	$2.13\ ^{+0.18}_{-0.25}$	$7.55\ ^{+0.20}_{-0.25}$	$0.89\ ^{+0.33}_{-0.28}$	2.3	1.04 (16)
1292.86	0.981	PL+G						0.24
40146-01-02-03R	0.054	$0.70\ ^{+3.9}_{-0.0}$	3-13	$2.07\ ^{+0.35}_{-0.12}$	$7.09\ ^{+0.31}_{-0.27}$	$1.06\ ^{+0.41}_{-0.34}$	1.9	0.500 (16)
1293.28	0.983	PL+G						2.82

Table 5.4: 40146 Set Cont.

OBS-ID	ϕ	N_H (10^{21} cm^{-2})	En. Range(s) (keV)	kT (keV)	Line E_1	σ_1	Total Lum.	Red. χ^2 (DOF)
JD-2450000	ψ	Model	*HEXTE* Cons.	or Γ	Line E_2 (keV)	σ_2 (keV)	(10^{35} D_3^2 erg/s)	Duration (ks)
40146-01-03-03R	0.140	$2.20\ ^{+0.2}_{-2.2}$	3-14	$43.38\ ^{+6.62}_{-19.45}$	$7.01\ ^{+0.15}_{-0.20}$	$0.01\ ^{+9.78}_{-0.00}$	4.8	0.991 (16)
1294.41	0.990	B+2G			$5.57\ ^{+1.68}_{-1.82}$	$0.01\ ^{+6.40}_{-0.00}$		2.75
40146-01-13-11R	0.952	$1.05\ ^{+3.1}_{-1.0}$	3-16	$12.57\ ^{+4.26}_{-3.31}$	$6.59\ ^{+0.12}_{-0.12}$	$0.63\ ^{+0.19}_{-0.19}$	2.0	0.388 (23)
1357.36	0.379	B+G						2.75
40146-01-14-03R	0.008	$2.40\ ^{+0.0}_{-1.4}$	3-15	$9.88\ ^{+1.87}_{-0.96}$	$7.66\ ^{+0.31}_{-0.65}$	$0.03\ ^{+1.09}_{-0.02}$	2.0	0.542 (18)
1358.09	0.383	B+2G			$6.44\ ^{+0.18}_{-0.22}$	$0.01\ ^{+1.80}_{-0.00}$		2.88
40146-01-14-07R	0.018	$0.70\ ^{+23.5}_{-0.0}$	3-13	$2.15\ ^{+7.85}_{-0.59}$	$6.60\ ^{+0.23}_{-0.37}$	$0.44\ ^{+5.17}_{-0.44}$	1.6	0.482 (13)
1358.22	0.384	PL+2G			$6.15\ ^{+3.14}_{-3.06}$	$1.92\ ^{+4.16}_{-1.60}$		2.69
40146-01-15-03R	0.084	$1.03\ ^{+1.9}_{-1.0}$	3-15	$12.43\ ^{+3.98}_{-2.45}$	$6.55\ ^{+0.21}_{-0.14}$	$0.01\ ^{+0.33}_{-0.00}$	2.2	0.428 (18)
1359.09	0.389	B+2G			$7.81\ ^{+0.30}_{-0.32}$	$0.10\ ^{+0.65}_{-0.00}$		2.82
40146-01-16-03R	0.105	$0.70\ ^{+2.6}_{-0.0}$	3-16	$16.30\ ^{+3.27}_{-4.66}$	$7.64\ ^{+0.43}_{-0.74}$	$0.01\ ^{+0.93}_{-0.00}$	2.3	0.765 (20)
1359.36	0.391	B+2G			$6.41\ ^{+0.14}_{-0.28}$	$0.31\ ^{+0.26}_{-0.31}$		2.69
40146-01-16-07R	0.115	$0.70\ ^{+2.4}_{-0.0}$	3-15	$16.66\ ^{+3.51}_{-4.61}$	$7.66\ ^{+0.40}_{-0.37}$	$0.01\ ^{+0.92}_{-0.00}$	2.2	0.734 (18)
1359.49	0.392	B+2G			$6.41\ ^{+0.14}_{-0.32}$	$0.31\ ^{+0.24}_{-0.31}$		0.24

Table 5.5: *RXTE* best fit model parameters for the 60058 observation set.

Error bars are at the 90% confidence level.

OBS-ID	ϕ	N_H (10^{21} cm^{-2})	En. Range(s) (keV)	kT (keV)	Line E_1	σ_1	Total Lum.	Red. χ^2 (DOF)
JD-2,450,000	ψ	Model	*HEXTE* Cons.	or Γ	Line E_2 (keV)	σ_2 (keV)	(10^{35} D_3^2 erg/s)	Duration (ks)
60058-01-01-00	0.107	$1.59^{+0.8}_{-0.7}$	3-29, 15-43	$27.60^{+4.16}_{-3.69}$	$7.05^{+1.03}_{-0.22}$	$0.83^{+0.27}_{-0.83}$	5.3	0.410 (49)
2222.80	0.716	B+2G	$0.55^{+0.10}_{-0.09}$		$6.57^{+0.10}_{-0.18}$	$0.33^{+0.81}_{-0.33}$		4.61
60058-01-02-00	0.178	$1.75^{+0.7}_{-0.6}$	3-26	$36.77^{+3.16}_{-5.09}$	$7.92^{+0.40}_{-0.96}$	$0.50^{+0.50}_{-0.17}$	3.3	0.795 (40)
2223.72	0.722	B+2G			$6.59^{+0.09}_{-0.21}$	$0.45^{+0.10}_{-0.40}$		5.04
60058-01-03-00	0.259	$2.11^{+0.7}_{-0.6}$	3-26, 15-45	$31.93^{+3.56}_{-3.96}$	$6.62^{+0.17}_{-0.28}$	$0.41^{+0.12}_{-0.41}$	6.1	0.860 (47)
2224.78	0.728	B+2G	$0.64^{+0.09}_{-0.08}$		$7.83^{+0.42}_{-0.99}$	$0.38^{+0.46}_{-0.00}$		4.48
60058-01-04-00	0.335	$2.31^{+0.1}_{-0.7}$	3-26	$33.11^{+5.79}_{-2.33}$	$7.34^{+1.64}_{-0.22}$	$1.07^{+0.19}_{-1.07}$	3.9	0.621 (40)
2225.77	0.734	B+2G			$6.70^{+0.13}_{-0.07}$	$0.49^{+0.18}_{-0.06}$		4.54
60058-01-05-00	0.405	$2.40^{+0.0}_{-0.1}$	3-28, 15-47	$36.26^{+1.82}_{-1.76}$	$6.77^{+0.03}_{-0.04}$	$0.54^{+0.04}_{-0.07}$	7.7	0.989 (49)
2226.70	0.740	B+2G	$0.58^{+0.07}_{-0.06}$		$8.45^{+0.15}_{-0.56}$	$0.00^{+0.38}_{-0.00}$		4.43
60058-01-06-00	0.486	$2.40^{+0.0}_{-0.6}$	3-24, 15-53	$28.75^{+3.92}_{-1.34}$	$6.77^{+0.07}_{-0.08}$	$0.08^{+0.28}_{-0.08}$	7.4	0.830 (48)
2227.76	0.746	B+2G	$0.69^{+0.07}_{-0.07}$		$6.96^{+0.10}_{-0.09}$	$1.01^{+0.16}_{-0.10}$		4.50
60058-01-07-00	0.562	$1.82^{+0.6}_{-1.3}$	3-28, 15-40	$29.10^{+12.00}_{-2.95}$	$6.77^{+0.29}_{-0.08}$	$0.01^{+4.22}_{-0.01}$	6.5	1.10 (48)
2228.75	0.753	B+2G	$0.55^{+0.08}_{-0.08}$		$6.90^{+0.13}_{-1.93}$	$0.91^{+4.14}_{-0.11}$		4.43
60058-01-08-00	0.643	$2.40^{+0.0}_{-0.4}$	3-26	$28.36^{+3.07}_{-1.65}$	$7.12^{+0.42}_{-0.23}$	$1.38^{+0.43}_{-0.37}$	4.1	0.799 (40)
2229.81	0.759	B+2G			$6.87^{+0.04}_{-0.07}$	$0.42^{+0.11}_{-0.31}$		4.50
60058-01-09-00	0.719	$2.17^{+0.6}_{-0.6}$	3-24	$24.10^{+2.79}_{-2.40}$	$8.68^{+0.28}_{-1.22}$	$0.01^{+1.18}_{-0.01}$	3.4	0.745 (38)
2230.80	0.765	B+2G			$6.89^{+0.04}_{-0.16}$	$0.57^{+0.07}_{-0.35}$		4.51
60058-01-10-00	0.861	$2.13^{+0.6}_{-0.7}$	3-24, 15-45	$27.59^{+4.80}_{-3.34}$	$6.93^{+0.13}_{-0.16}$	$1.11^{+0.28}_{-0.17}$	7.9	1.20 (45)
2232.65	0.777	B+2G	$0.61^{+0.08}_{-0.08}$		$6.87^{+0.06}_{-0.08}$	$0.19^{+1.20}_{-0.19}$		3.92
60058-01-11-00	0.946	$1.63^{+0.7}_{-0.7}$	3-23	$16.39^{+1.74}_{-1.39}$	$8.67^{+0.22}_{-0.19}$	$0.01^{+0.34}_{-0.01}$	2.9	0.954 (37)

Table 5.5: 60058 Set Cont.

OBS-ID	ϕ	N_H (10^{21} cm^{-2})	En. Range(s) (keV)	kT (keV)	Line E_1	σ_1	Total Lum.	Red. χ^2 (DOF)
JD-2450000	ψ	Model	*HEXTE* Cons.	or Γ	Line E_2 (keV)	σ_2 (keV)	(10^{35} D_3^2 erg/s)	Duration (ks)
2233.78	0.784	B+2G			$6.93^{+0.05}_{-0.05}$	$0.63^{+0.08}_{-0.09}$		4.30
60058-01-12-00	0.027	$1.83^{+1.2}_{-0.3}$	3-25	$15.78^{+1.72}_{-2.40}$	$7.41^{+0.60}_{-1.60}$	$1.15^{+1.49}_{-0.01}$	2.8	0.567 (39)
2234.84	0.790	B+2G			$6.83^{+0.20}_{-0.15}$	$0.51^{+0.28}_{-0.20}$		4.43
60058-01-13-00	0.103	$1.70^{+0.9}_{-0.9}$	3-25, 15-45	$36.62^{+12.48}_{-6.89}$	$6.89^{+0.05}_{-0.05}$	$0.16^{+0.21}_{-0.16}$	6.4	0.752 (47)
2235.83	0.796	B+2G	$0.44^{+0.07}_{-0.07}$		$6.76^{+0.16}_{-0.30}$	$1.30^{+0.46}_{-0.26}$		5.25
60058-01-15-00	0.169	$2.40^{+0.0}_{-0.7}$	3-25	$30.76^{+5.44}_{-1.42}$	$6.86^{+0.06}_{-0.06}$	$0.29^{+0.17}_{-0.29}$	4.3	0.717 (39)
2236.69	0.802	B+2G			$7.03^{+0.20}_{-0.16}$	$1.10^{+0.29}_{-0.17}$		4.21
60058-01-16-00	0.235	$2.40^{+0.0}_{-2.4}$	3-31	$1.54^{+0.01}_{-0.19}$	$6.74^{+0.06}_{-0.51}$	$1.32^{+0.53}_{-0.09}$	5.6	1.00 (46)
2237.55	0.807	PL+2G			$6.91^{+0.08}_{-0.04}$	$0.01^{+1.85}_{-0.00}$		3.30
60058-01-17-00	0.326	$2.26^{+0.7}_{-0.7}$	3-26, 15-40	$31.40^{+6.03}_{-4.19}$	$6.94^{+0.12}_{-3.14}$	$1.19^{+0.19}_{-0.17}$	8.5	1.01 (47)
2238.74	0.814	B+2G	$0.63^{+0.06}_{-0.06}$		$7.07^{+0.05}_{-0.06}$	$0.01^{+0.16}_{-0.00}$		3.87

Table 5.6: *RXTE* best fit model parameters for the 70416 observation set.

Error bars are at the 90% confidence level.

OBS-ID	ϕ	N_H (10^{21} cm^{-2})	En. Range(s) (keV)	kT (keV)	Line E_1	σ_1	Total Lum.	Red. χ^2 (DOF)
JD-2,450,000	ψ	Model	*HEXTE* Cons.	or Γ	Line E_2 (keV)	σ_2 (keV)	(10^{35} D_3^2 erg/s)	Duration (ks)
70416-01-01-00	0.734	$1.41^{+0.9}_{-0.6}$	3-20	$17.64^{+1.75}_{-2.22}$	$6.69^{+0.05}_{-0.06}$	$0.33^{+0.09}_{-0.11}$	2.7	1.24 (30)
2544.97	0.703	B+2G			$8.00^{+0.23}_{-1.12}$	$0.01^{+2.14}_{-0.00}$		1.98

Table 5.6: 70416 Set Cont.

OBS-ID	ϕ	N_H (10^{21} cm^{-2})	En. Range(s) (keV)	kT (keV)	Line E_1	σ_1	Total Lum.	Red. χ^2 (DOF)
JD-2450000	ψ	Model	*HEXTE* Cons.	or Γ	Line E_2 (keV)	σ_2 (keV)	(10^{35} D_3^2 erg/s)	Duration (ks)
70416-01-01-01	0.749	$2.33\ ^{+0.8}_{-0.6}$	3-25, 15-51	$13.06\ ^{+1.71}_{-1.13}$	$7.94\ ^{+0.30}_{-0.93}$	$0.01\ ^{+0.91}_{-0.01}$	3.9	0.605 (42)
2545.17	0.704	B+2G	$1.04\ ^{+0.35}_{-0.33}$		$6.69\ ^{+0.07}_{-0.20}$	$0.32\ ^{+0.11}_{-0.32}$		2.61
70416-01-01-02	0.756	$1.29\ ^{+0.7}_{-0.7}$	3-21	$15.44\ ^{+1.75}_{-1.43}$	$6.65\ ^{+0.11}_{-0.23}$	$0.36\ ^{+0.14}_{-0.36}$	2.5	0.701 (32)
2545.25	0.704	B+2G			$7.82\ ^{+0.25}_{-0.91}$	$0.31\ ^{+0.61}_{-0.31}$		2.30

Table 5.7: *RXTE* best fit model parameters for the 90401 observation set.

Error bars are at the 90% confidence level.

OBS-ID	ϕ	N_H (10^{21} cm^{-2})	En. Range(s) (keV)	kT (keV)	Line E_1	σ_1	Total Lum.	Red. χ^2 (DOF)
JD-2,450,000	ψ	Model	*HEXTE* Cons.	or Γ	Line E_2 (keV)	σ_2 (keV)	(10^{35} D_3^2 erg/s)	Duration (ks)
90401-01-01-01	0.425	$0.91\ ^{+0.6}_{-0.5}$	3-30, 15-66	$39.64\ ^{+7.05}_{-5.70}$	$7.33\ ^{+0.05}_{-0.05}$	$0.05\ ^{+0.14}_{-0.00}$	13.1	1.46 (51)
3077.29	0.986	B+2G	$1.13\ ^{+0.08}_{-0.07}$		$6.70\ ^{+0.10}_{-0.13}$	$1.42\ ^{+0.07}_{-0.15}$		2.46
90401-01-02-00	0.380	$0.93\ ^{+0.3}_{-0.9}$	3-24, 15-68	$43.44\ ^{+16.42}_{-7.40}$	$6.92\ ^{+0.09}_{-0.17}$	$1.21\ ^{+0.22}_{-0.06}$	16.0	1.09 (56)
3089.78	0.063	B+2G	$0.65\ ^{+0.06}_{-0.07}$		$7.34\ ^{+0.10}_{-0.51}$	$0.01\ ^{+0.30}_{-0.01}$		1.76
90401-01-02-01	0.365	$1.09\ ^{+0.7}_{-0.7}$	3-27, 15-62	$30.03\ ^{+5.35}_{-4.17}$	$7.09\ ^{+0.09}_{-0.05}$	$0.00\ ^{+0.34}_{-0.00}$	13.0	1.04 (54)
3089.58	0.061	B+2G	$1.04\ ^{+0.10}_{-0.10}$		$6.45\ ^{+0.13}_{-0.26}$	$1.34\ ^{+0.27}_{-0.17}$		1.47
90401-01-03-00	0.595	$2.39\ ^{+0.0}_{-1.3}$	3-25, 15-60	$1.79\ ^{+0.02}_{-0.09}$	$7.08\ ^{+0.09}_{-0.05}$	$0.01\ ^{+3.55}_{-0.00}$	10.2	1.16 (46)
3092.60	0.080	PL+2G	$0.97\ ^{+0.10}_{-0.09}$		$6.93\ ^{+0.08}_{-0.17}$	$1.13\ ^{+0.19}_{-0.11}$		2.38
90401-01-03-01	0.515	$0.70\ ^{+0.4}_{-0.7}$	3-25, 15-50	$33.19\ ^{+9.99}_{-2.92}$	$6.77\ ^{+0.06}_{-0.20}$	$1.35\ ^{+0.23}_{-0.10}$	12.0	1.49 (55)
3091.54	0.074	B+2G	$0.70\ ^{+0.05}_{-0.07}$		$7.18\ ^{+0.07}_{-0.04}$	$0.00\ ^{+2.12}_{-0.00}$		2.54

Table 5.7: 90401 Set Cont.

OBS-ID	ϕ	N_H (10^{21} cm^{-2})	En. Range(s) (keV)	kT (keV)	Line E_1	σ_1	Total Lum.	Red. χ^2 (DOF)
JD-2450000	ψ	Model	*HEXTE* Cons.	or Γ	Line E_2 (keV)	σ_2 (keV)	(10^{35} D_3^2 erg/s)	Duration (ks)
90401-01-03-02	0.574	$0.70\ ^{+0.3}_{-0.0}$	3-29, 15-43	$25.65\ ^{+1.11}_{-1.90}$	$7.12\ ^{+0.42}_{-0.42}$	$0.00\ ^{+2.94}_{-0.00}$	7.7	1.12 (49)
3092.32	0.078	B+2G	$0.96\ ^{+0.08}_{-0.08}$		$6.74\ ^{+0.08}_{-0.09}$	$1.09\ ^{+0.11}_{-0.10}$		5.66
90401-01-04-00	0.013	$1.80\ ^{+0.9}_{-1.8}$	3-23, 15-41	$2.47\ ^{+0.06}_{-0.19}$	$7.28\ ^{+1.24}_{-1.12}$	$0.00\ ^{+0.30}_{-0.00}$	2.5	1.01 (46)
3241.97	0.001	PL+2G	$0.98\ ^{+0.18}_{-0.24}$		$6.74\ ^{+0.11}_{-0.50}$	$1.29\ ^{+0.49}_{-0.18}$		11.5
90401-01-04-000	0.988	$0.70\ ^{+0.2}_{-0.0}$	3-20, 15-50	$7.01\ ^{+0.20}_{-0.25}$	$6.92\ ^{+0.48}_{-0.14}$	$0.99\ ^{+0.19}_{-0.23}$	2.2	1.30 (45)
3241.64	0.999	B+2G	$1.51\ ^{+0.22}_{-0.20}$		$7.28\ ^{+0.15}_{-0.99}$	$0.00\ ^{+6.48}_{-0.00}$		28.4
90401-01-04-01	0.863	$2.40\ ^{+0.0}_{-0.6}$	3-29, 15-57	$1.76\ ^{+0.01}_{-0.05}$	$7.48\ ^{+0.07}_{-0.10}$	$0.00\ ^{+1.51}_{-0.00}$	11.8	0.903 (54)
3240.00	0.989	PL+2G	$0.56\ ^{+0.05}_{-0.05}$		$7.17\ ^{+0.08}_{-0.14}$	$1.35\ ^{+0.17}_{-0.12}$		2.96
90401-01-04-02	0.949	$1.44\ ^{+2.2}_{-1.4}$	3-23, 15-50	$2.19\ ^{+0.16}_{-0.15}$	$6.89\ ^{+0.45}_{-0.75}$	$1.62\ ^{+0.58}_{-0.41}$	3.5	0.868 (45)
3241.12	0.996	PL+2G	$0.90\ ^{+0.28}_{-0.28}$		$7.33\ ^{+0.10}_{-0.09}$	$0.00\ ^{+1.36}_{-0.00}$		1.76

It is noted that, if the *HEXTE* spectra are good beyond the energy range of the *PCA* spectra, the addition of *HEXTE* data reduces the error bars of the spectral parameters in the majority of cases. This occurs for 19 out of 78 observations (see Tables 5.1-5.7). Thus, including the *HEXTE* data does in fact improve the accuracy of the model fits. Table 5.8 demonstrates this using the 90401-01-01-01 observation as an example. The energy ranges for the *PCA* and *HEXTE* data are 3-30 keV and 15-66 keV, respectively. The parameter values are from the best fit model, B+2G, and the error bars are at the 90% confidence level.

Table 5.8: Addition of *HEXTE* data improves the fit for the observation 90401-01-01-01. The errors are at the 90% confidence level.

Parameter	Value	Errors without *HEXTE*	Errors with *HEXTE*
N_H (10^{22} cm^{-2})	0.906	$^{+0.43}_{-0.90}$	$^{+0.562}_{-0.522}$
kT (keV)	39.64	$^{+17.1}_{-4.45}$	$^{+7.05}_{-5.70}$
Line E_1 (keV)	7.329	$^{+0.053}_{-0.055}$	$^{+0.051}_{-0.049}$
σ_1 (keV)	5.00×10^{-2}	$^{+0.16}_{-0.001}$	$^{+0.14}_{-0.001}$
Line E_2 (keV)	6.702	$^{+0.11}_{-0.22}$	$^{+0.10}_{-0.13}$
σ_2 (keV)	1.418	$^{+0.23}_{-0.12}$	$^{+0.072}_{-0.15}$
Red. χ^2 (DOF)		1.52 (45)	1.46 (51)

Also, in approximately half of these 19 observations, the addition of the *HEXTE* data allows for a better discrimination of the best fit model. This was tested by fitting only the *PCA* data with the same parameters as noted in Tables 5.1-5.7. If the spectra that included both *PCA* and *HEXTE* data has a larger spread (difference) between the reduced χ^2 values for the PL+2G and B+2G models, it allows for

an easier determination of the best fit model. Another major benefit to using the *HEXTE* data is that it covers the hard X-ray energy range that connects *Chandra* and *INTEGRAL* observations.

5.3.1 Correlation of Spectral Parameters

The useful energy range for each observation seen in Tables 5.1-5.7 is dependent on the binary phase as well as the length of the observation. This energy range decreases when the binary phase, $\phi \sim 0$ (**inferior conjunction** of the companion) because the compact object is blocked and therefore the X-ray energy decreases. This is demonstrated in Figure 5.2 (see Appendix B for lightcurves of all observation sets). The energy range also decreases if the duration of the observation is short, reducing

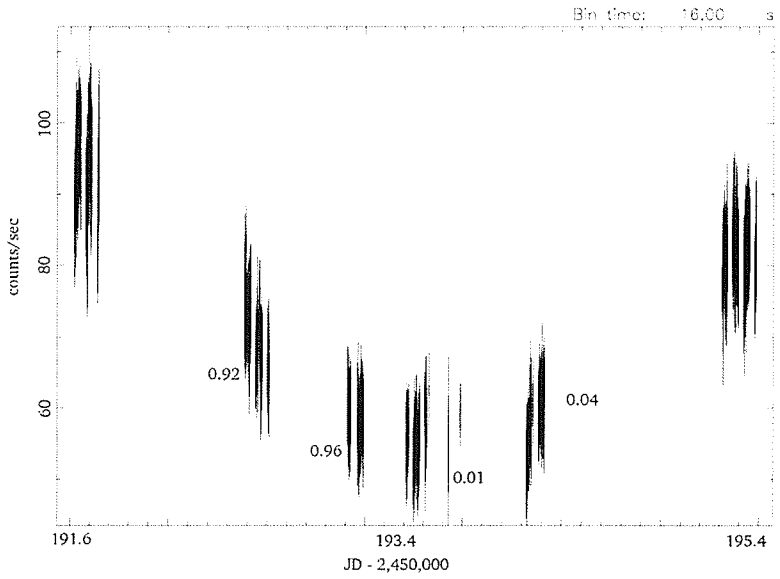

Figure 5.2: The lightcurve of all observations in the 10127 data set. The numbers in the graph are the binary phases of the observations. Notice that the count rate decreases when primary eclipse of the compact object occurs ($\phi \sim 0$).

the signal-to-noise ratio. The precessional phase most likely affects the useful energy range as well, and seems to do so at $\psi \sim 0.5$ (observation 20102-01-07-00). However, there are not many observations at this phase, so this cannot be confirmed.

Unfortunately, for the 40146 data set, the first two situations apply, therefore explaining why the useful energy ranges are smaller than the other data sets, and why the error bars for some of the spectral parameters are large. For this reason, this data set will not be included in the following analysis.

The spectral parameters, temperature, kT, photon index, Γ, and total unabsorbed flux (i.e. calculated flux assuming a column density, $N_H = 0$), can be correlated with the binary phase, ϕ. These are shown in Figures 5.3, 5.4, and 5.5, respectively.

Only the observations with the best fit model of B+2G are used for the kT graph, while the observations with PL+2G as the best fit model are used for the graph of Γ. All observations are used in the flux graph, but using the total unabsorbed flux (*PCA* plus *HEXTE* fluxes, if applicable) calculated from the best fit model. Note that each data set occurs at different precessional and binary phases, which accounts for the variety of peak heights in Figures 5.3 - 5.5.

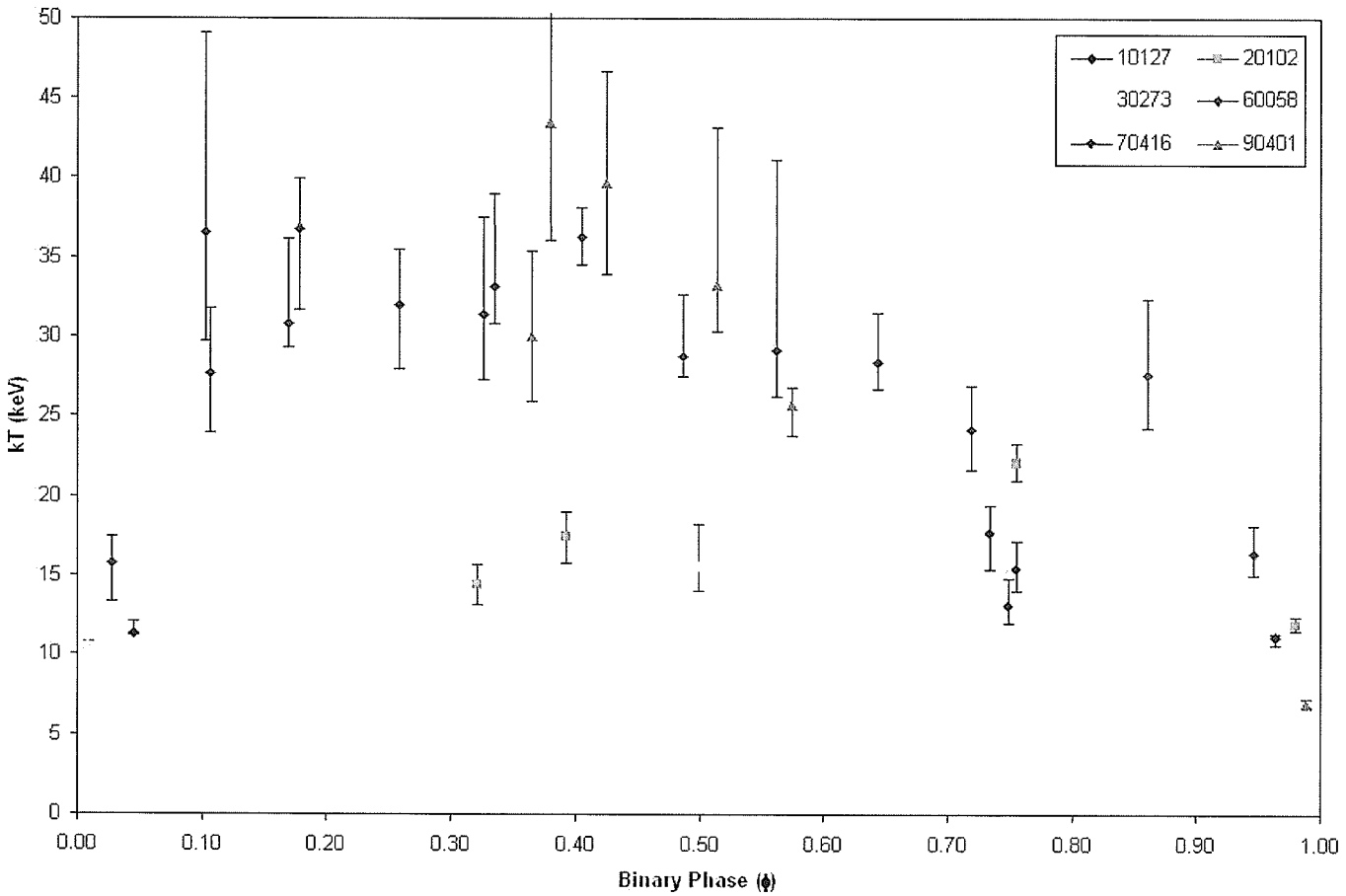

Figure 5.3: kT versus binary phase.

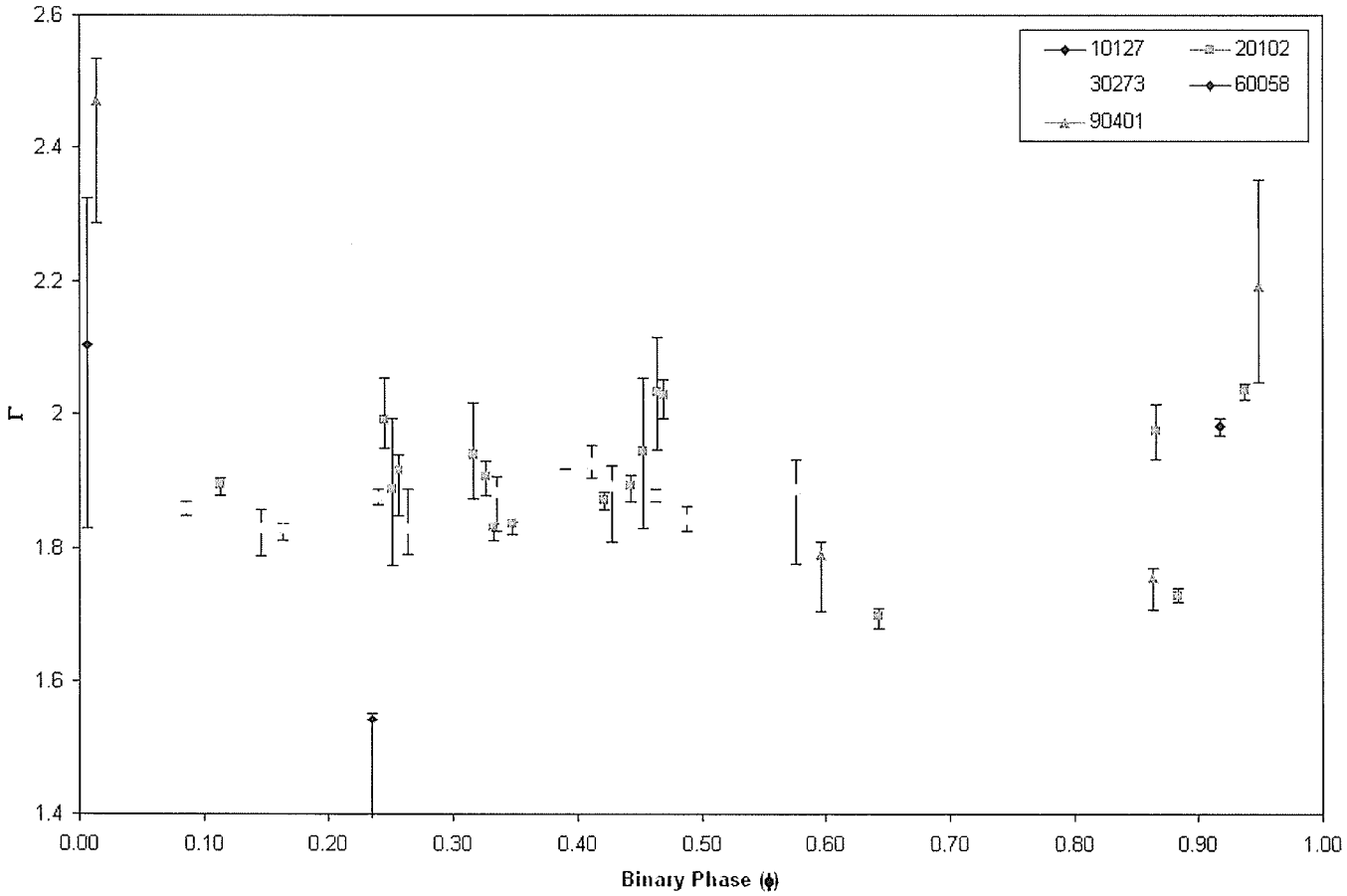

Figure 5.4: Γ versus binary phase.

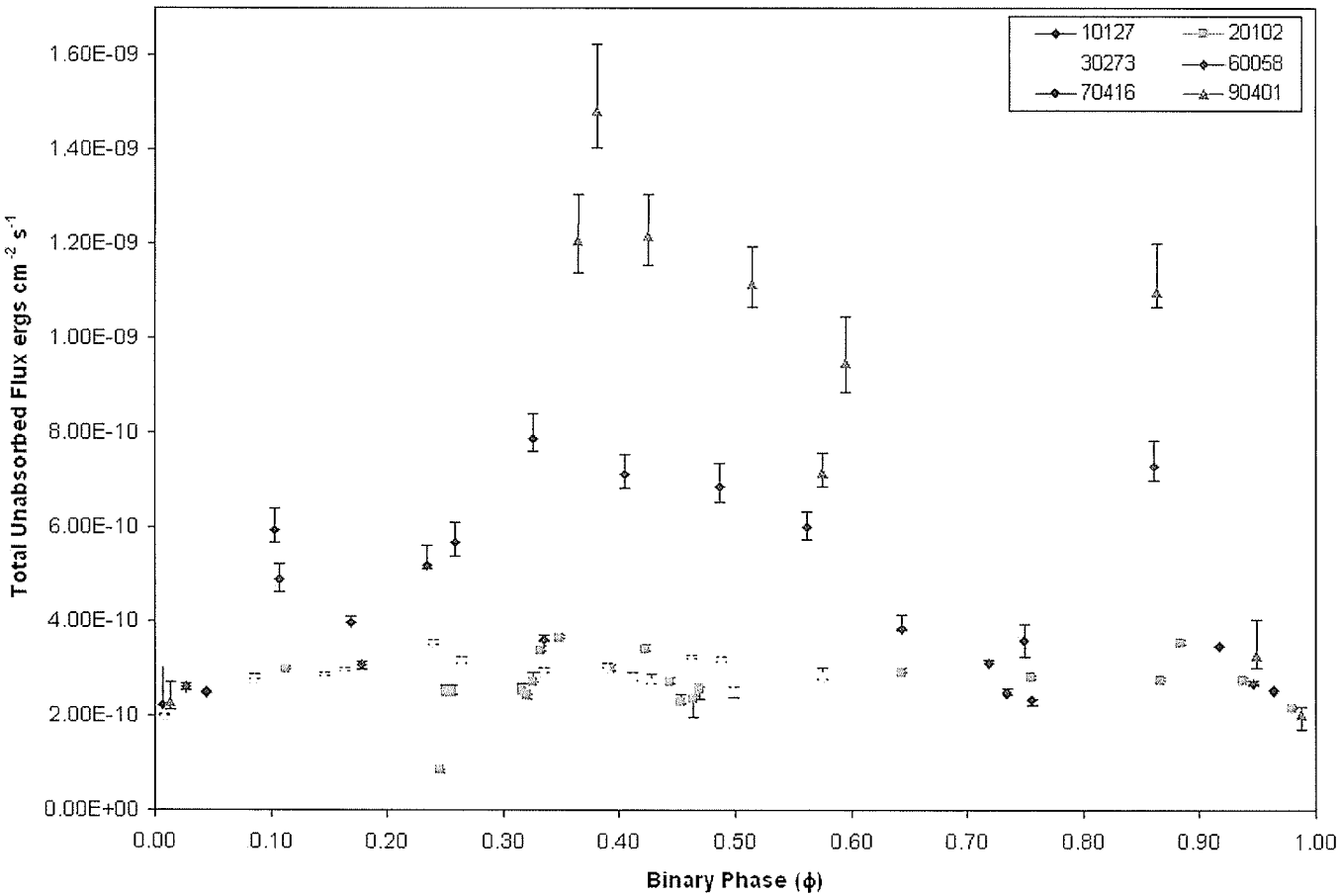

Figure 5.5: Total unabsorbed flux (*PCA* plus *HEXTE*) versus binary phase.

kT and flux are at a minimum during inferior conjunction of the companion ($\phi \sim 0$). Γ is oppositely correlated, having a maximum near $\phi \sim 0$. The X-ray spectrum hardens when the compact object is eclipsing the companion (**superior conjunction**). These results are as expected in an X-ray binary system. When the compact object is eclipsed and only the companion star is seen (whose emission does not peak in X-rays), the X-ray brightness will decrease. Thus, the X-ray flux decreases as does the observed temperature. The spectrum softens (i.e. Γ is larger) because the X-ray luminosity from the companion star is much less than that of the compact object.

Figure 5.6 shows how the spectra vary with different combinations of ϕ and ψ. In the top left, $(\phi,\psi) \approx (0,0)$: the binary is in inferior conjunction and the eastern jet is pointed toward the observer. Notice that the bump is less evident when compared to the top right figure ($(\phi,\psi) \approx (0.5,0)$), during superior conjunction. When $(\phi,\psi) \approx (0,0.5)$ or $(0.5,0.5)$ these bumps are much larger (bottom left and bottom right spectra in Figure 5.6).

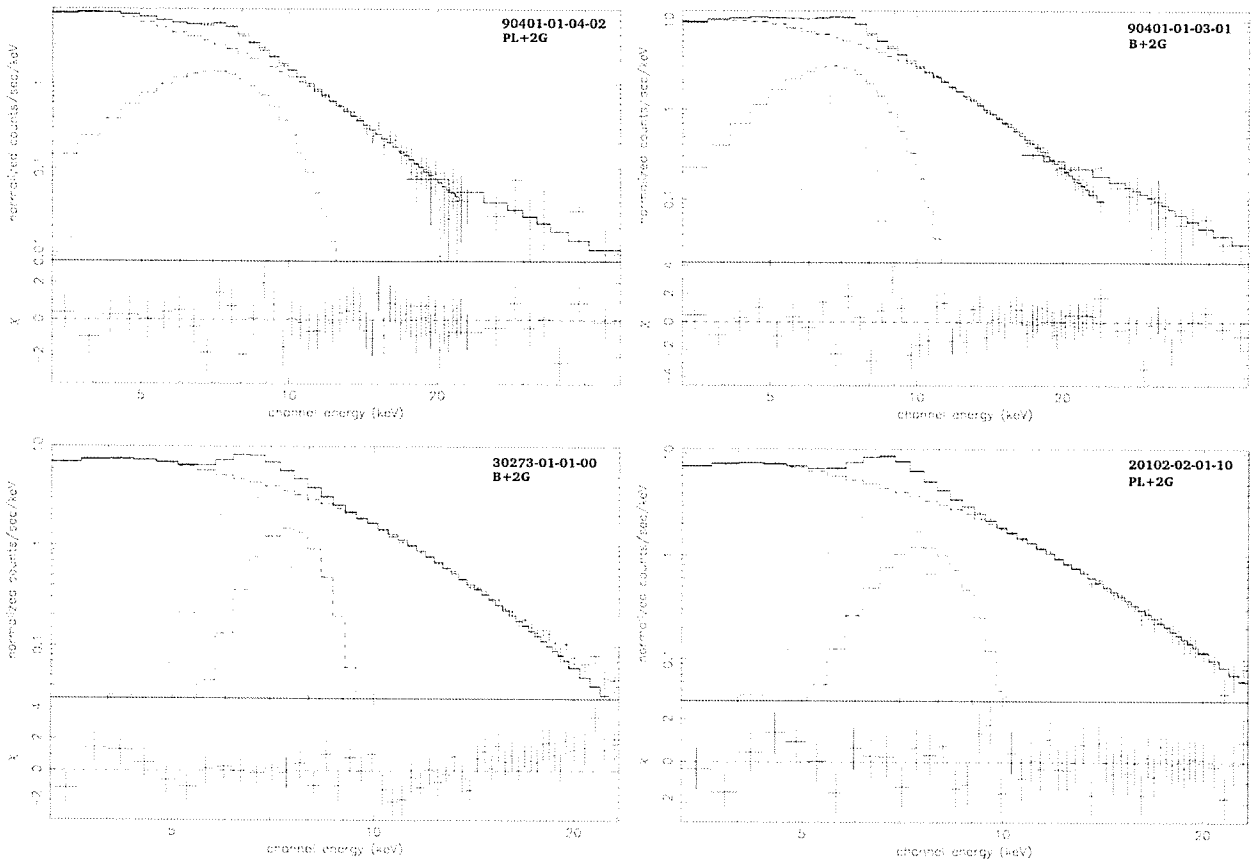

Figure 5.6: Example spectra with different combinations of ϕ and ψ. Crosses are data and the solid line is the fitted model. **Top left:** Observation 90401-01-04-02, with $(\phi,\psi) \approx (0,0)$. **Top right:** Observation 90401-01-03-01, with $(\phi,\psi) \approx (0.5,0)$. **Bottom left:** Observation 30273-01-01-00, with $(\phi,\psi) \approx (0,0.5)$. **Bottom right:** Observation 20102-02-01-10, with $(\phi,\psi) \approx (0.5,0.5)$. Notice the difference in the bump that occurs near 7 keV.

This indicates that some of the line emission must be coming from the jets. When $\psi \sim 0$, the eastern jet (see Figure 2.3) is pointed toward us. At this point, the red and blueshifted lines are at maximum separation, and are not overlapping in the spectra. In this case, when $\phi \sim 0$, the compact object, and therefore the base of the jets, is eclipsed by the companion, and a small, spread-out bump at $\sim$7 keV is observed. However, when $\phi \sim 0.5$, the compact object and base of the jets are visible, so the strength of the lines increase, giving rise to a larger bump. On the other hand, when $\psi \sim 0.5$, the western jet (Figure 2.3) is pointed toward us, and the lines are at a secondary maximum separation. The lines overlap more so in the spectra than at $\psi \sim 0$. Also, because the accretion disk is more visible at this phase, the Fe fluorescence line is observed. This gives rise to a much more prominent bump at $\sim$7 keV, regardless of the binary phase.

Since the spectra are best fit by either the B+2G and PL+2G models roughly half the time each, this indicates that the emission could be a function of both ϕ and ψ. Figure 5.7 shows that the best fit model is indeed spatially separated on the plot. Note that the emission is, in general, modeled by PL+2G when $\psi \sim$ 0.4-0.6, and by B+2G between $\psi \sim$ 0.6-0.8. The best-fit model does not depend on the binary phase of the system. Therefore, the emission seems to depend on the orientation of the jets: when the western jet is pointing toward the observer ($\psi \sim 0.5$) the emission is non-thermal; mid-phase, when $\psi \sim 0.75$, the emission is thermal in nature.

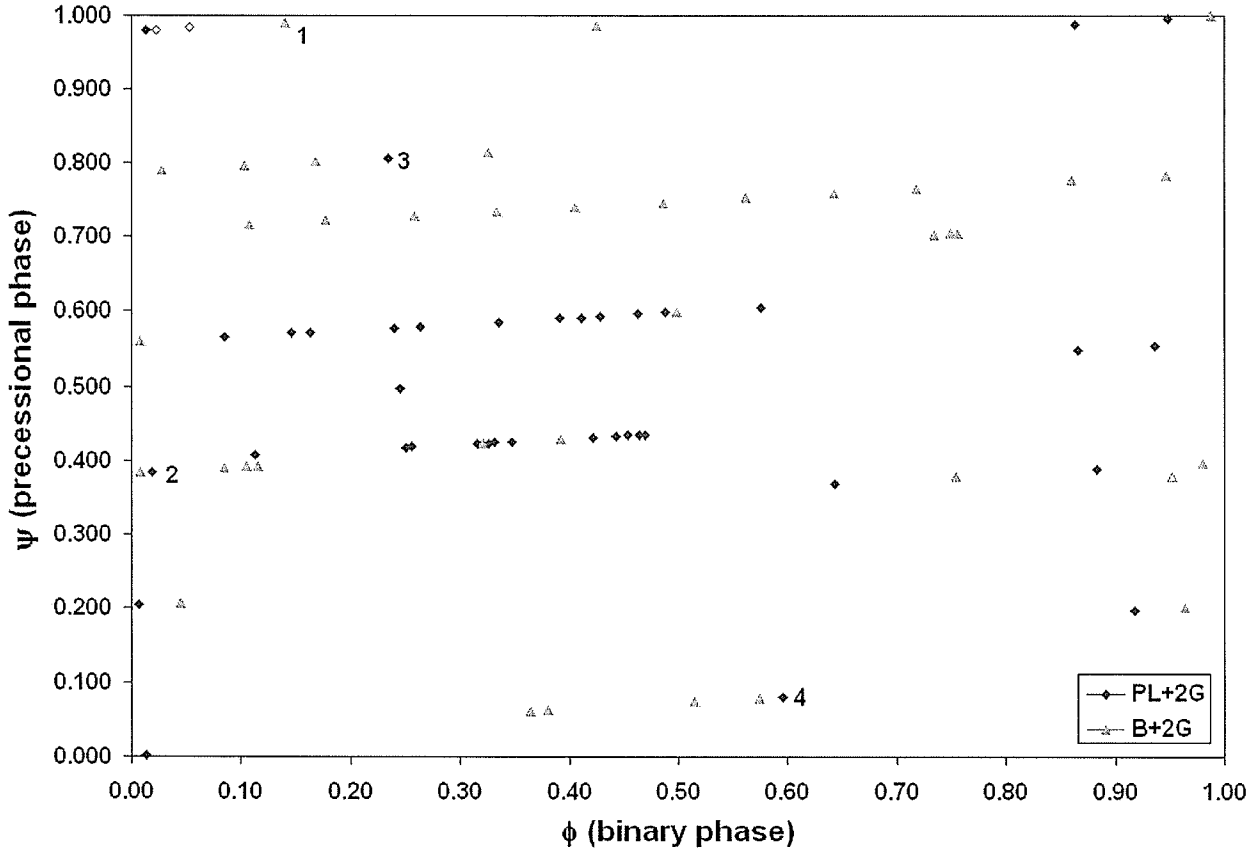

Figure 5.7: The best fit model for each observation as a function of ϕ and ψ. The open diamonds and triangle represent the observations that are best fit by the PL+G and B+G models, respectively. There is a spatial separation on the plot between the observations with the B+2G and PL+2G best fit models, indicating that the observed emission depends on the orientation of the system. Refer to section 5.3.2 for the points marked with numbers 1-4.

This is to be expected since, when one of the jets is pointing toward us, we see further into the jet, where higher energy interactions (described by a non-thermal model) are occurring. When the jets are mid-phase, we are not looking as deep into the jet, and therefore observe lower energy (thermal) interactions.

Unfortunately, there have been no archived or public *RXTE* observations between $\psi \sim$ 0.1-0.4 to confirm that the emission in this range would be best fit by B+2G. The anomalous observations in Figure 5.7 (i.e. those that do not follow the best fit model pattern) could be due to radio activity of the source (see following section).

There seems to be a discrepancy of the best fit model at $\psi \sim$ 0.9-0.1. In this phase range, the PL+2G and B+2G are the best fit models for seven observations each. This indicates that the interpretation above might be too simple, and other aspects may be involved in the emission mechanisms of this source (such as effects from the magnetic field and accretion disk). These results also hint that there is probably both thermal and non-thermal emission occurring in the jets and near the compact object.

To further investigate the effect of the Fe-line model fitting on the hard X-ray tail, each observation is being re-fit, ignoring energies below 8.5 keV. Time constraints do not allow for this work to be included in this thesis, but it is the subject of a paper in preparation.

5.3.2 Radio & X-ray Correlations

The radio activity of SS 433 has been monitored with the RATAN-600 radio telescope since 1986 (Trushkin et al., 2003; S. Trushkin 2005, private communication). This large data set allows observations in other wavelengths to be correlated with the

radio activity. Safi-Harb & Kotani (2002) and Kotani et al. (2002) have studied the correlations between the radio activity and data from the 60058 set. The *RXTE* data used for this thesis overlaps with four individual radio flares. Figures 5.8 - 5.11 show the variations of the spectral parameters (temperature, photon index, and unabsorbed flux) as a function of **Julian Date**, near when a radio flare occurs.

A radio flare in the SS 433 binary system causes an ejection of a jet bullet (see Chapter 2). Right before this event occurs, the accretion disk will compress, causing a decrease in the X-ray flux (since the X-ray object is smaller). As the bullet moves out from the binary, the accretion disk will expand, and the X-ray flux will increase (Trushkin et al., 2003). During the flare, the X-ray temperature is expected to increase, then decrease gradually. The photon index should peak at the onset of the flare, then decrease rapidly (i.e. the spectrum will soften prior to the flare, then harden directly afterward).

Two radio flares occur within the 40146 data set. The variations of the spectral parameters after the first radio flare are seen in Figure 5.8. The ranges of ϕ and ψ are 0.013-0.140 and 0.980-0.990, respectively. The temperature, kT, and the unabsorbed flux decrease after the radio flare, while the photon index, Γ, seems to peak near the radio flare, and then decreases. The first three observations are best fit by either the PL+2G or PL+G models, while the last observation is best fit by B+2G (marked '1' in Figure 5.7). Unfortunately, there are no *RXTE* observations before this radio flare, so it cannot be determined if the model changed to a power-law directly after the event, or if the spectral parameters behave as expected.

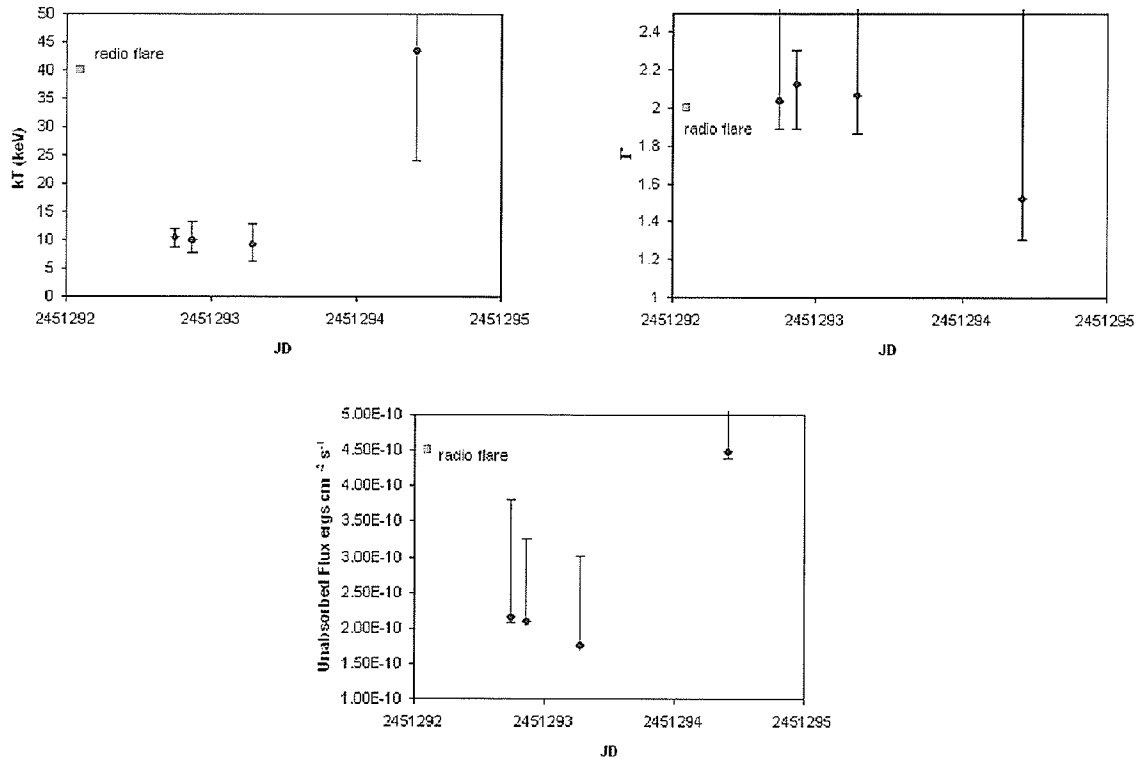

Figure 5.8: The spectral parameter variations of the first four observations in the 40146 data set. The pink square refers to only the time of the radio flare. **Top left:** The temperature, kT, from the B+2G/G fits. **Top right:** The photon index, Γ, from the PL+2G/G fits. **Bottom:** The unabsorbed flux, from the best fit model.

The variations of the spectral parameters near the second radio flare are seen in Figure 5.9. The ranges of ϕ and ψ are 0.952-0.115 and 0.379-0.392. kT and unabsorbed flux decrease after the radio flare, while Γ peaks near the flare, and then decreases. All of the observations are best fit with a B+2G or B+G model, except for the third observation, which is fit best by PL+2G (marked '2' in Figure 5.7). There are no *RXTE* observations before the radio flare to determine if the model changed after the event, or if the spectral parameters behave as predicted.

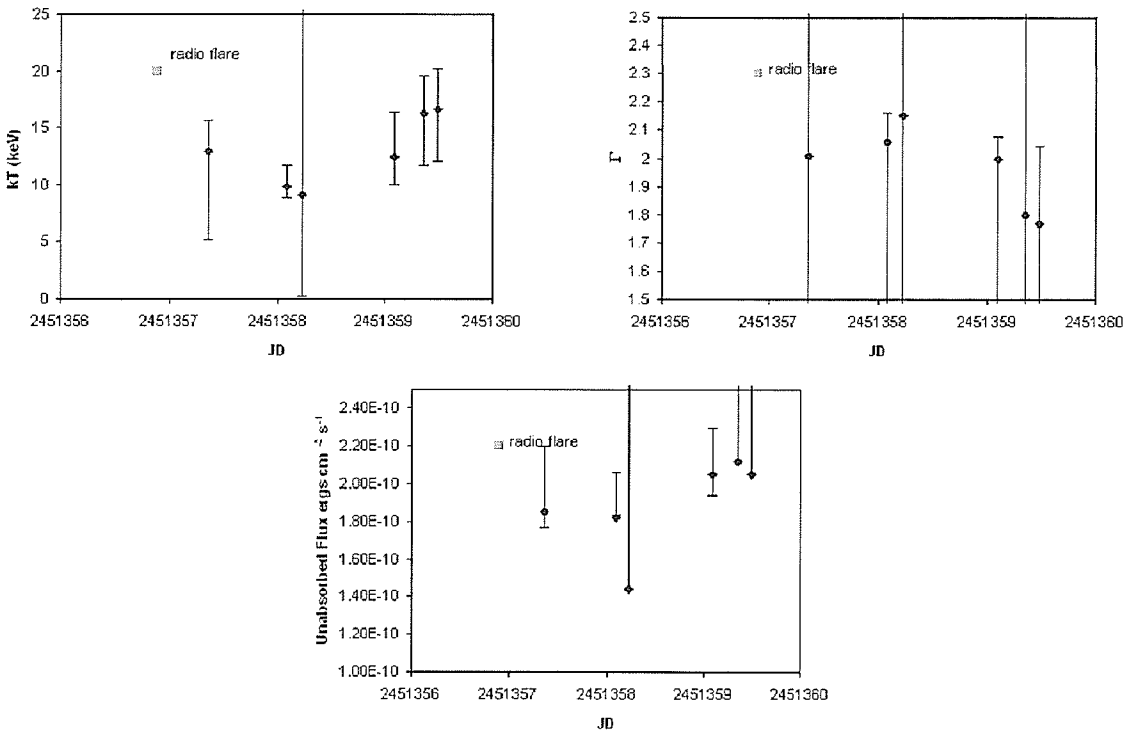

Figure 5.9: The spectral parameter variations of the last six observations in the 40146 data set. The pink square refers to only the time of the radio flare. **Top left:** The temperature, kT, from the B+2G/G fits. **Top right:** The photon index, Γ, from the PL+2G/G fits. **Bottom:** The unabsorbed flux, from the best fit model.

The third radio flare occurs within the 60058 data set, and the variations of the spectral parameters are seen in Figure 5.10. These observations cover ϕ = 0.107-0.326 and ψ = 0.716-0.814. The temperature, kT, peaks directly after the radio flare, while the unabsorbed flux decreases prior to it, then increases. Γ peaks right before the event, then dramatically decreases. Every observation in this set is best fit by B+2G, except the second to last one, which is best fit by PL+2G (marked '3' in Figure 5.7). The reduced χ^2 for this observation is 1.00 compared to 1.13 for the

B+2G model, with 46 degrees of freedom. The temperature derived with the B+2G model is also very high ($\sim$ 65 keV), so this model can be ruled out.

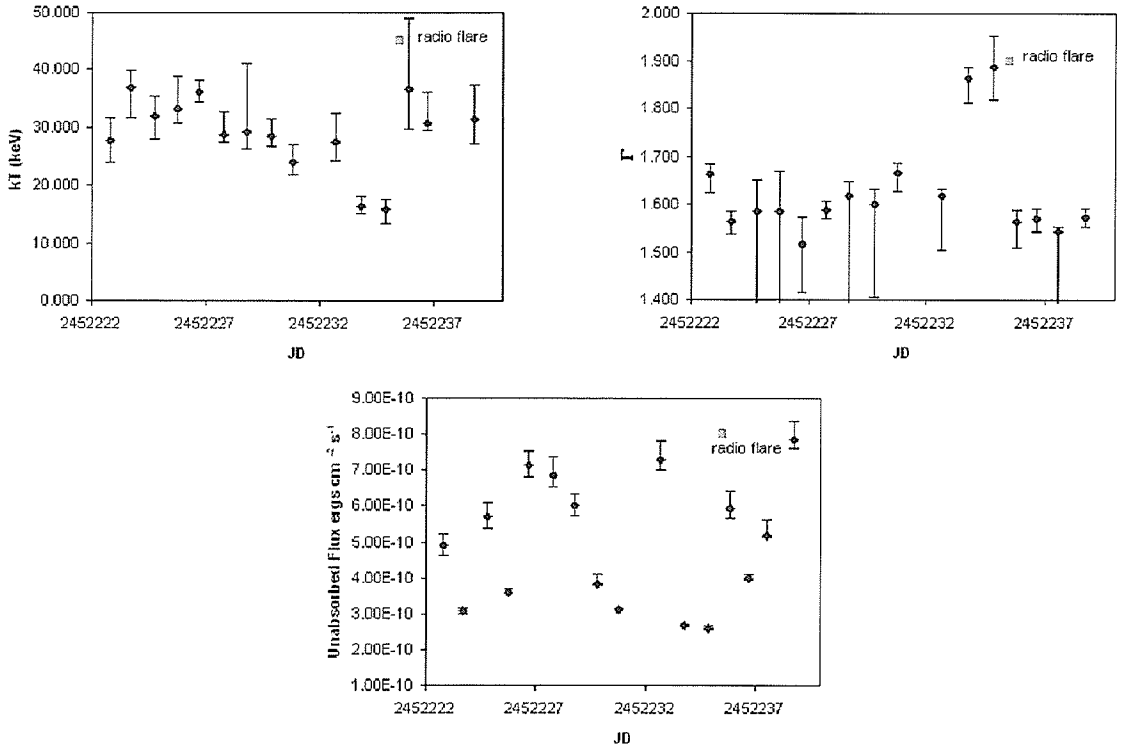

Figure 5.10: The spectral parameter variations the observations in the 60058 data set. The pink square refers to only the time of the radio flare. **Top left:** The temperature, kT, from the B+2G/G fits. **Top right:** The photon index, Γ, from the PL+2G/G fits. **Bottom:** The unabsorbed flux, from the best fit model.

Thus, the spectrum may have switched from thermal to power-law temporarily after the radio flare. This behavior is as described above, and is similar to other microquasars (Safi-Harb & Kotani, 2002).

The last radio flare occurs within five observations in the 90401 data set, covering $\phi = 0.380$-0.574 and $\psi = 0.063$-0.078. The variations of the parameters as a function

of Julian Date near the flare are seen in Figure 5.11. kT, unabsorbed flux, and Γ

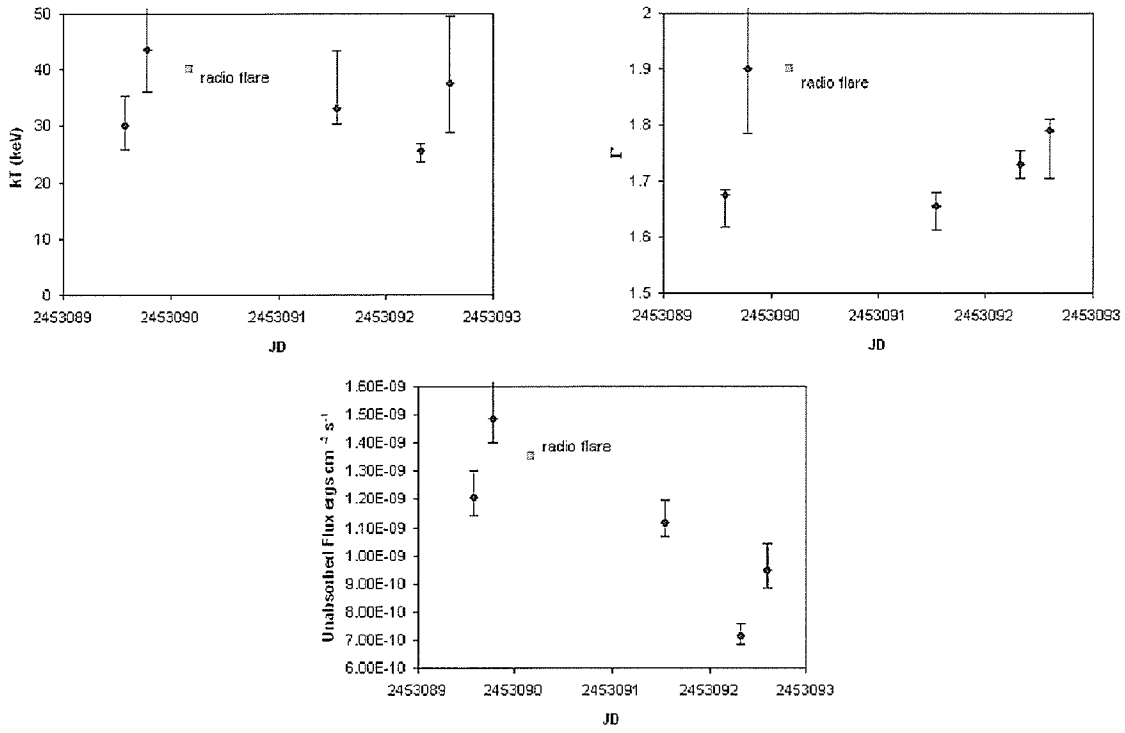

Figure 5.11: The spectral parameter variations of five observations in the 90401 data set. The pink square refers to only the time of the radio flare. **Top left:** The temperature, kT, from the B+2G/G fits. **Top right:** The photon index, Γ, from the PL+2G/G fits. **Bottom:** The unabsorbed flux, from the best fit model.

all seem to peak before the radio flare, then decrease. The flux does not behave as expected, which could be due to the orientation of the system: the compact object is in front of the companion, and the eastern jet is pointed toward the observer. These two conditions could increase the X-ray flux enough to cancel out the effect from the radio flare. All of the observations are fit best by a B+2G model, except for the third observation, which is best fit by PL+2G (marked '4' in Figure 5.7). As with 60058,

the B+2G model can be ruled out for this observation, and the spectrum seems to have switched to a power-law after the radio flare for a short time.

As previously explained, since the data in the 40416 data set do not have many data points in each observation, the error bars for the spectral parameters are rather large. Also, the behavior of the spectral parameters in the 40146 data set cannot be determined, as the radio flare is not encompassed by X-ray observations. Thus, the correlations from the 60058 and 90401 data sets are more reliable. The behavior seen in the 60058 data set agree with those reported by Safi-Harb & Kotani (2002), and are similar to that of other microquasars. Both kT and Γ in the 90401 data set seem to behave in the same manner, but the flux does not, as explained above.

In each set that overlaps with a radio flare, there is always one observation which has a different best fit model than the other observations in that set. In the 40416a set, all but one of the observations are best fit with PL+2G/G models. In the 40146b and 60058 sets, all but one of the observations in each set are best fit with B+2G/G models. The 90401 set is fit best by B+2G and PL+2G about half the time each (see Table 5.7). The 40146a and 90401 sets have $\psi \sim 0$, one of the expected phases where the spectrum should more likely be modeled with a power-law. The other two data sets occur mid-phase (i.e. not $\psi \sim 0$ or 0.5), where the emission is expected to be due to bremsstrahlung radiation (discussed in the previous section). Thus, for at least three of these cases, a radio flare seems to switch the emission mechanism from that which is expected. This confirms that the 'anomalous' points in Figure 5.7 could be due to radio flares.

5.3.3 Redshifts

The theoretical redshifts for each observation are calculated using the equation from the kinematic model (Abell & Margon, 1979):

$$1 + z = \gamma(1 \pm v_j \; sin\theta \; sini \; cos(2\pi\psi) \pm v_j \; cos\theta \; cosi) \tag{5.1}$$

where

$$\psi = \frac{t - t_{0,p}}{P_p}, \tag{5.2}$$

θ is the half-opening angle of the jet cone, i is the inclination angle, v_j is the velocity of the jet, γ is the Lorentz factor, $t_{0,p}$ is the initial epoch for the precessional period, P_p, and t is the Julian date of the observation (see Table 2.1 for values). The 2π is included to convert the precessional phase to radians. Using this convention, a negative value for z corresponds to blueshifts, and a positive z corresponds to redshifts. The theoretical redshift curves are plotted in Figure 5.12.

The observational redshifts are calculated from the line energies (denoted by Line E in Tables 5.1-5.7) derived from the best fit model in each observation, using both the rest energies of Fe XXV and Fe XXVI, and the relations

$$z = \frac{\lambda_0 - \lambda}{\lambda} \tag{5.3}$$

and

$$E = h\nu = \frac{hc}{\lambda} \tag{5.4}$$

where λ_0 is the rest energy of the line, h is Planck's constant, and c is the speed of light. The best fit observed redshifts are plotted in Figure 5.12.

Rest energies of both lines are used to determine which lines are best fit to the theoretical redshift values. These best fits are in sets: for example if z calculated

from Line E_1, using the Fe XXV line (6.684 keV), matches closely with one of the theoretical calculations, then z from Line E_2 must be from the Fe XXVI line. However, if one of the observed line energies is ~6.4 keV, it could be due to the Fe fluorescence line. For this to be an accurate determination, the uncertainty of the energy of these lines are confirmed to encompass the 6.4 keV line, and the precessional phase must not be near $\psi \sim 0$.

The Fe fluorescence line is most likely in 43 of the spectra. The other line energy is chosen to best match the theoretical calculations of z. Table 5.9 summarizes the calculated theoretical redshifts, the observed line energies of each observation, and the most probable identification of those lines.

Table 5.9: Identification of the Fe lines and redshifts.

OBS-ID	Theoretical z (+)	Line E_1 (keV)	Line 1 ID
ψ	Theoretical z (-)	Line E_2 (keV)	Line 2 ID
10127-01-02-00	0.115	6.82	Fe XXVI
0.195	-0.044	7.07	Fe XXV
10127-01-03-00	0.113	6.69	Fe XXVI
0.199	-0.042	6.82	Fe XXV
10127-01-05-00	0.111	6.91	Fe XXVI
0.203	-0.040	6.93	Fe XXV
10127-01-06-00	0.109	6.85	Fe XXVI
0.206	-0.038	6.96	Fe XXV
20102-01-01-00	0.024	6.52	Fe fl.
0.369	0.047	7.11	Fe XXV
20102-01-02-00	0.020	6.57	Fe fl.
0.378	0.051	7.71	Fe XXVI

Table 5.9: Redshifts/Line IDs cont.

OBS-ID	Theoretical z (+)	Line E_1 (keV)	Line 1 ID
ψ	Theoretical z (-)	Line E_2 (keV)	Line 2 ID
20102-01-03-00	0.016	6.54	Fe fl.
0.388	0.055	7.05	Fe XXV
20102-01-04-00	0.014	6.54	Fe fl.
0.396	0.058	7.69	Fe XXVI
20102-01-05-00	0.010	6.46	Fe fl.
0.406	0.061	7.11	Fe XXV
20102-01-06-00	0.007	6.54	Fe fl.
0.418	0.065	6.92	Fe XXV
20102-01-07-00	-0.005	6.58	Fe XXV
0.498	0.076	7.46	Fe XXVI
20102-02-01-00	0.003	6.62	Fe fl.
0.431	0.068	7.12	Fe XXV
20102-02-01-01	0.005	6.57	Fe fl.
0.424	0.066	6.96	Fe XXV
20102-02-01-02	0.007	6.48	Fe fl.
0.418	0.065	7.09	Fe XXV
20102-02-01-03	0.005	6.53	Fe fl.
0.423	0.066	7.05	Fe XXV
20102-02-01-04	0.005	6.57	Fe fl.
0.423	0.066	7.73	Fe XXVI
20102-02-01-05	0.005	6.50	Fe fl.
0.424	0.066	7.11	Fe XXV
20102-02-01-060	0.005	6.59	Fe fl.
0.425	0.067	6.99	Fe XXV

Table 5.9: Redshifts/Line IDs cont.

OBS-ID	Theoretical z (+)	Line E_1 (keV)	Line 1 ID
ψ	Theoretical z (-)	Line E_2 (keV)	Line 2 ID
20102-02-01-07	0.004	6.62	Fe fl.
0.429	0.068	6.95	Fe XXV
20102-02-01-08	0.003	6.46	Fe fl.
0.434	0.069	7.14	Fe XXV
20102-02-01-09	0.002	6.49	Fe fl.
0.435	0.069	7.31	Fe XXV
20102-02-01-10	0.002	6.60	Fe fl.
0.435	0.069	7.57	Fe XXVI
20102-02-01-11	0.003	6.61	Fe fl.
0.433	0.069	7.90	Fe XXVI
20102-02-02-00	0.000	6.49	Fe fl.
0.554	0.071	7.05	Fe XXV
20102-02-02-01	-0.001	6.49	Fe fl.
0.548	0.072	7.15	Fe XXV
30273-01-01-00	0.001	6.48	Fe fl.
0.559	0.070	7.46	Fe XXVI
30273-01-01-01	0.003	6.51	Fe fl.
0.566	0.069	6.99	Fe XXV
30273-01-02-00	0.004	6.52	Fe fl.
0.572	0.067	7.04	Fe XXV
30273-01-02-01	0.006	6.63	Fe fl.
0.580	0.065	7.87	Fe XXVI
30273-01-02-010	0.006	6.56	Fe fl.
0.578	0.066	7.06	Fe XXV

Table 5.9: Redshifts/Line IDs cont.

OBS-ID	Theoretical z (+)	Line E_1 (keV)	Line 1 ID
ψ	Theoretical z (-)	Line E_2 (keV)	Line 2 ID
30273-01-02-02	0.004	6.43	Fe fl.
0.570	0.068	7.18	Fe XXV
30273-01-03-00	0.008	6.61	Fe fl.
0.586	0.064	7.06	Fe XXV
30273-01-03-01	0.010	6.49	Fe fl.
0.592	0.062	7.18	Fe XXV
30273-01-03-010	0.009	6.52	Fe fl.
0.590	0.062	7.04	Fe XXV
30273-01-03-02	0.010	6.53	Fe fl.
0.593	0.061	6.91	Fe XXV
30273-01-04-000	0.011	6.45	Fe fl.
0.596	0.060	7.15	Fe XXV
30273-01-05-01	0.012	6.51	Fe fl.
0.598	0.060	7.65	Fe XXVI
30273-01-05-02	0.014	6.51	Fe fl.
0.605	0.057	7.02	Fe XXV
30273-01-05-03	0.012	6.49	Fe fl.
0.599	0.060	7.44	Fe XXVI
40146-01-01-03R	0.174	5.84	Fe XXVI
0.980	-0.102	7.36	Fe XXV
40146-01-01-07R	0.174	7.55	Fe XXV
0.981	-0.103	-	-
40146-01-02-03R	0.174	7.09	Fe XXV
0.983	-0.103	-	-

Table 5.9: Redshifts/Line IDs cont.

OBS-ID	Theoretical z (+)	Line E_1 (keV)	Line 1 ID
ψ	Theoretical z (-)	Line E_2 (keV)	Line 2 ID
40146-01-03-03R	0.174	5.57	Fe XXVI
0.990	-0.103	7.01	Fe XXV
40146-01-13-11R	0.020	6.59	Fe fl.
0.379	0.051	-	-
40146-01-14-03R	0.018	6.44	Fe fl.
0.383	0.053	7.66	Fe XXVI
40146-01-14-07R	0.018	6.15	Fe fl.
0.384	0.054	6.60	Fe XXVI
40146-01-15-03R	0.016	6.55	Fe fl.
0.389	0.055	7.81	Fe XXVI
40146-01-16-03R	0.015	6.41	Fe fl.
0.391	0.056	7.64	Fe XXVI
40146-01-16-07R	0.015	6.41	Fe fl.
0.392	0.056	7.66	Fe XXVI
60058-01-01-00	0.066	6.57	Fe fl.
0.716	0.006	7.05	Fe XXV
60058-01-02-00	0.069	6.59	Fe fl.
0.722	0.003	7.92	Fe XXVI
60058-01-03-00	0.072	6.62	Fe fl.
0.728	-0.001	7.83	Fe XXVI
60058-01-04-00	0.076	6.70	Fe XXVI
0.734	-0.005	7.34	Fe XXV
60058-01-05-00	0.079	6.77	Fe XXVI
0.740	-0.008	8.45	Fe XXV

Table 5.9: Redshifts/Line IDs cont.

OBS-ID	Theoretical z (+)	Line E_1 (keV)	Line 1 ID
ψ	Theoretical z (-)	Line E_2 (keV)	Line 2 ID
60058-01-06-00	0.083	6.77	Fe XXVI
0.746	-0.011	6.96	Fe XXV
60058-01-07-00	0.086	6.77	Fe XXVI
0.753	-0.015	6.90	Fe XXV
60058-01-08-00	0.090	6.87	Fe XXVI
0.759	-0.019	7.12	Fe XXV
60058-01-09-00	0.093	6.89	Fe XXVI
0.765	-0.022	8.68	Fe XXV
60058-01-10-00	0.100	6.87	Fe XXVI
0.777	-0.028	6.93	Fe XXV
60058-01-11-00	0.104	6.93	Fe XXVI
0.784	-0.032	8.67	Fe XXV
60058-01-12-00	0.107	6.83	Fe XXVI
0.790	-0.036	7.41	Fe XXV
60058-01-13-00	0.110	6.76	Fe XXVI
0.796	-0.039	6.89	Fe XXV
60058-01-15-00	0.113	6.86	Fe XXVI
0.802	-0.042	7.03	Fe XXV
60058-01-16-00	0.116	6.74	Fe XXVI
0.807	-0.045	6.91	Fe XXV
60058-01-17-00	0.120	6.94	Fe XXVI
0.814	-0.049	7.07	Fe XXV
70416-01-01-00	0.059	6.69	Fe XXV
0.703	0.013	8.00	Fe XXVI

Table 5.9: Redshifts/Line IDs cont.

OBS-ID	Theoretical z (+)	Line E_1 (keV)	Line 1 ID
ψ	Theoretical z (-)	Line E_2 (keV)	Line 2 ID
70416-01-01-01	0.059	6.69	Fe XXV
0.704	0.012	7.94	Fe XXVI
70416-01-01-02	0.059	6.65	Fe XXV
0.704	0.012	7.82	Fe XXVI
90401-01-01-01	0.174	6.70	Fe XXVI
0.986	-0.103	7.33	Fe XXV
90401-01-02-00	0.168	6.92	Fe XXVI
0.063	-0.096	7.34	Fe XXV
90401-01-02-01	0.168	6.45	Fe XXVI
0.061	-0.097	7.09	Fe XXV
90401-01-03-00	0.163	6.93	Fe XXVI
0.080	-0.092	7.08	Fe XXV
90401-01-03-01	0.165	6.77	Fe XXVI
0.074	-0.094	7.18	Fe XXV
90401-01-03-02	0.164	6.74	Fe XXVI
0.078	-0.093	7.12	Fe XXV
90401-01-04-00	0.175	6.74	Fe XXVI
0.001	-0.103	7.28	Fe XXV
90401-01-04-000	0.175	6.92	Fe XXVI
0.999	-0.103	7.28	Fe XXV
90401-01-04-01	0.174	7.17	Fe XXVI
0.989	-0.103	7.48	Fe XXV
90401-01-04-02	0.175	6.89	Fe XXVI
0.996	-0.103	7.33	Fe XXV

Figure 5.12 shows the theoretical redshift curves, using a precessional period of 162.15 days, along with the best fit observed redshifts. The data fits the model well at ~JD 2,450,250 and ~2,452,250. The discrepancies in the other observed redshifts could be due to the modulations previously observed in the precessional period of the jets (it has been observed to be anywhere from 161-165 days).

Figures 5.13 and 5.14 show the theoretical redshift curves using a 161 and 165 day precessional period, respectively. For simplicity, these graphs assume that the initial epoch, when $\psi = 0$, occurs at the same date (see Table 2.1). It is seen that the data does fit to these theoretical curves better in some instances.

To investigate this further, the *RXTE* data is fit by Equation 5.1, with precessional period, P_p, and the date of initial epoch, $t_{0,p}$, (and therefore ψ) being allowed to vary. All other quantities are assumed to have the values as outlined in Table 2.1. Using MATLAB version 7, the minimum χ^2 value for the fit is then determined. Figure 5.15 shows the best fit curve, while Figure 5.16 shows a two-dimensional plot of the χ^2 contours, as a function of precessional phase offset and precessional period. The green star in Figure 5.16 shows that the minimum χ^2 contour (darkest blue) actually extends over a range of values. Thus, the best fit values for P_p and ψ are constrained to a one-dimensional solution. However, it is noted that the best fit values of the phase offset and P_p for this data are ~ 0.4 and ~ 165.5 days, respectively. These results indicate that the modulation in the period should be taken into account in the kinematic model. Further studies are required to determine if this modulation is periodic.

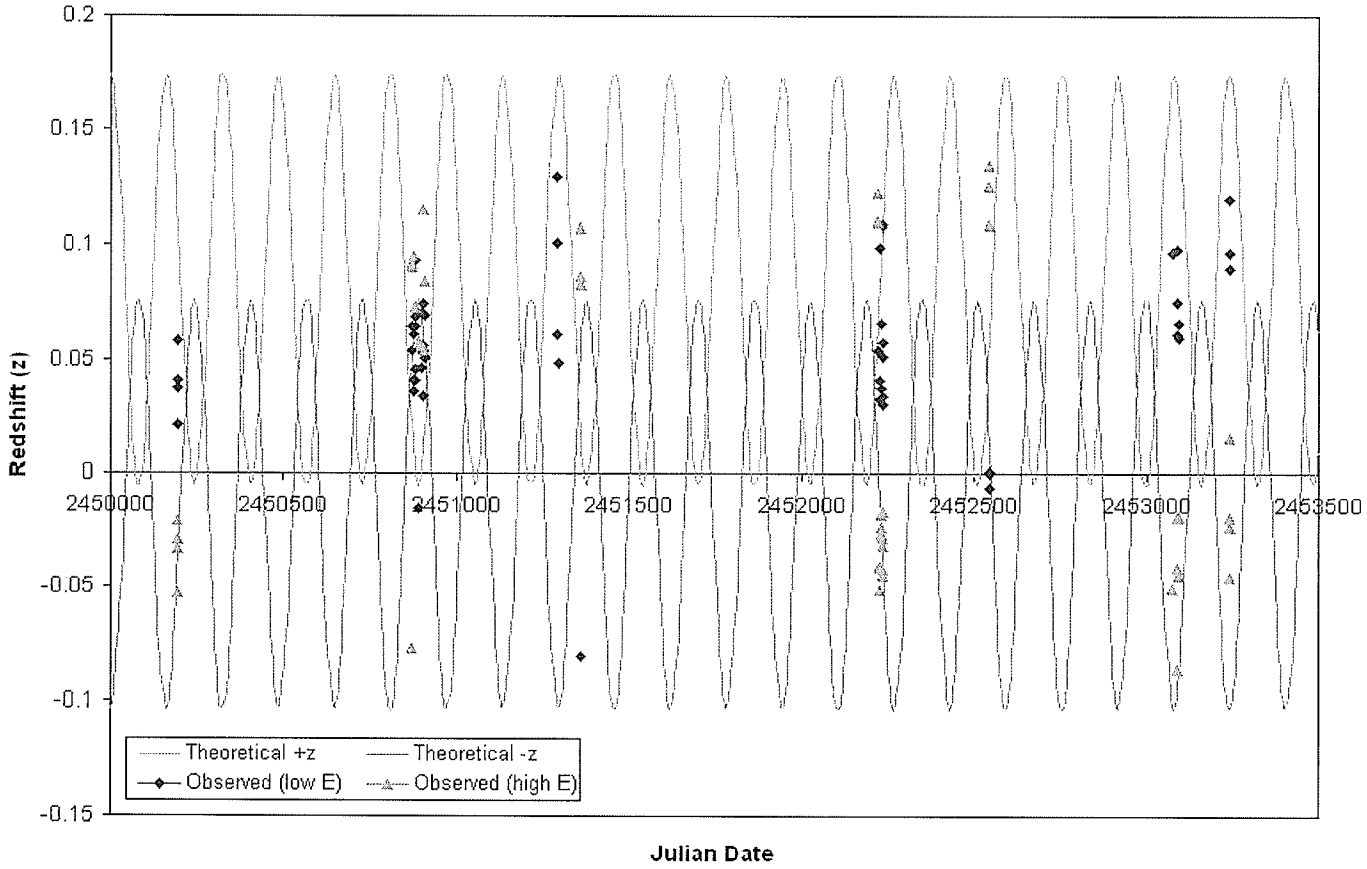

Figure 5.12: The theoretical redshift curves are calculated from the kinematic model using a precessional period of 162.15 days. The Observed (low E) points are the redshifts that most likely correspond to Fe XXV, while the Observed (high E) points most likely correspond with Fe XXVI. The lines associated with Fe fluorescence are not shown, as they are in the stationary spectrum.

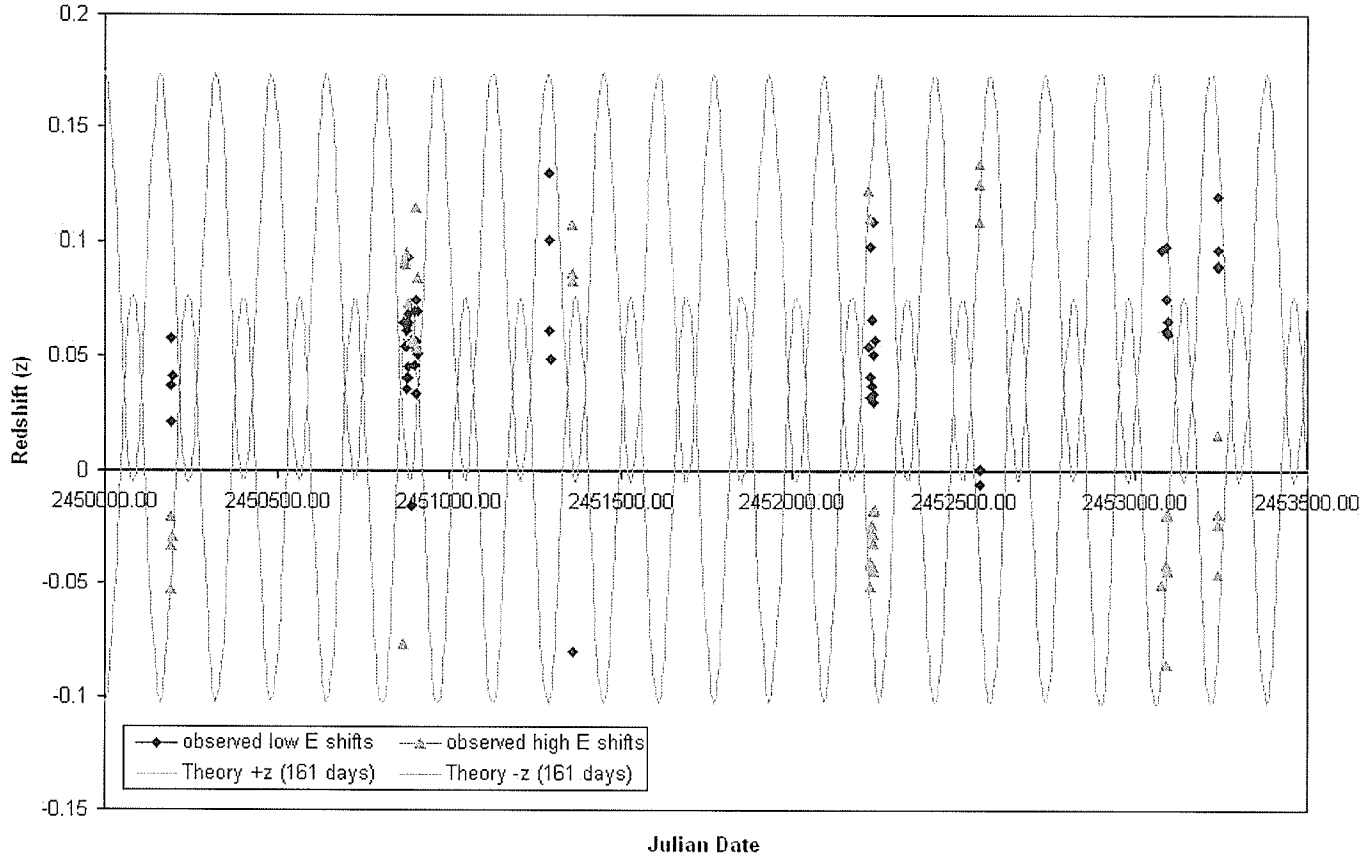

Figure 5.13: The theoretical redshift curves are calculated from the kinematic model, but using a precessional period of 161 days.

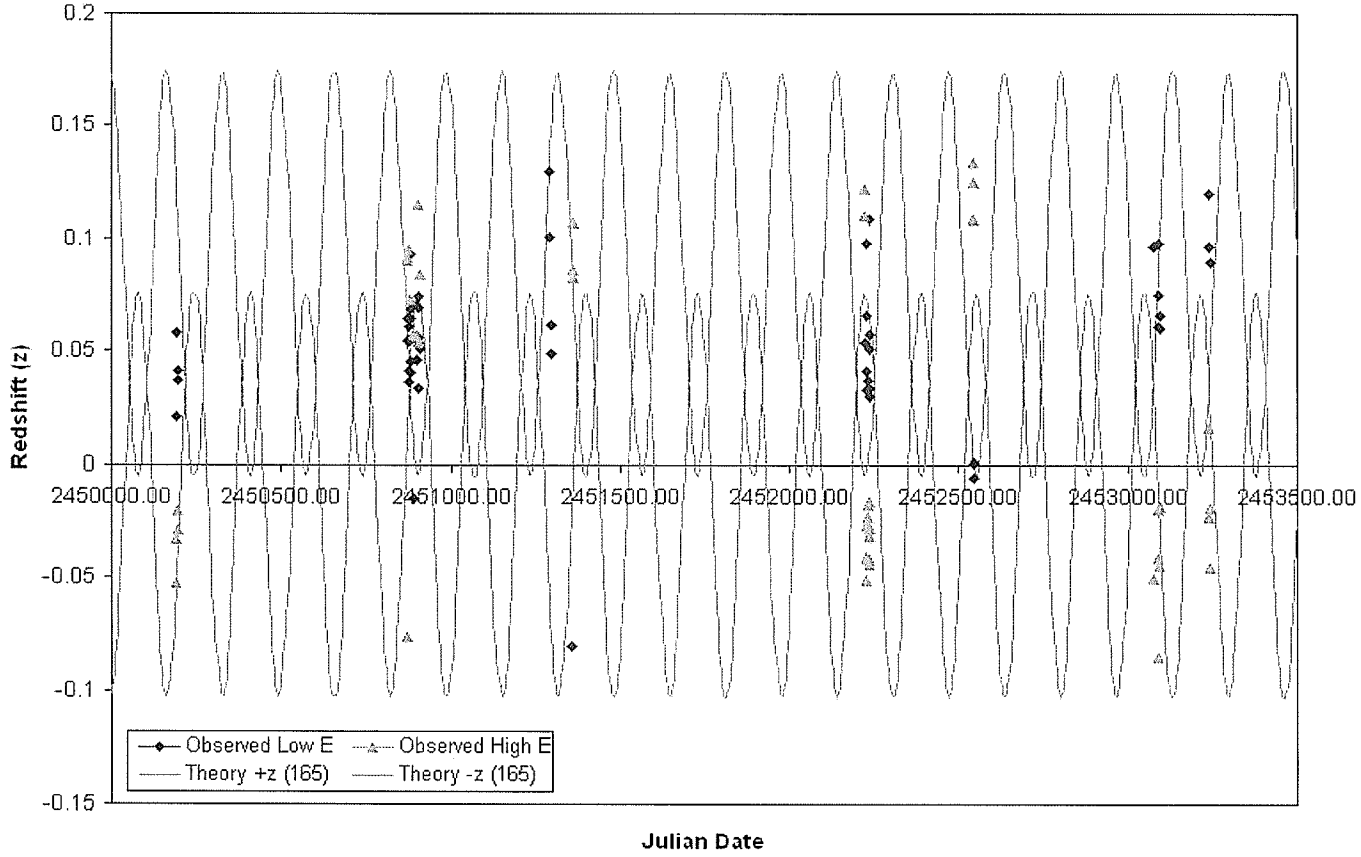

Figure 5.14: The theoretical redshift curves are calculated from the kinematic model, but using a precessional period of 165 days.

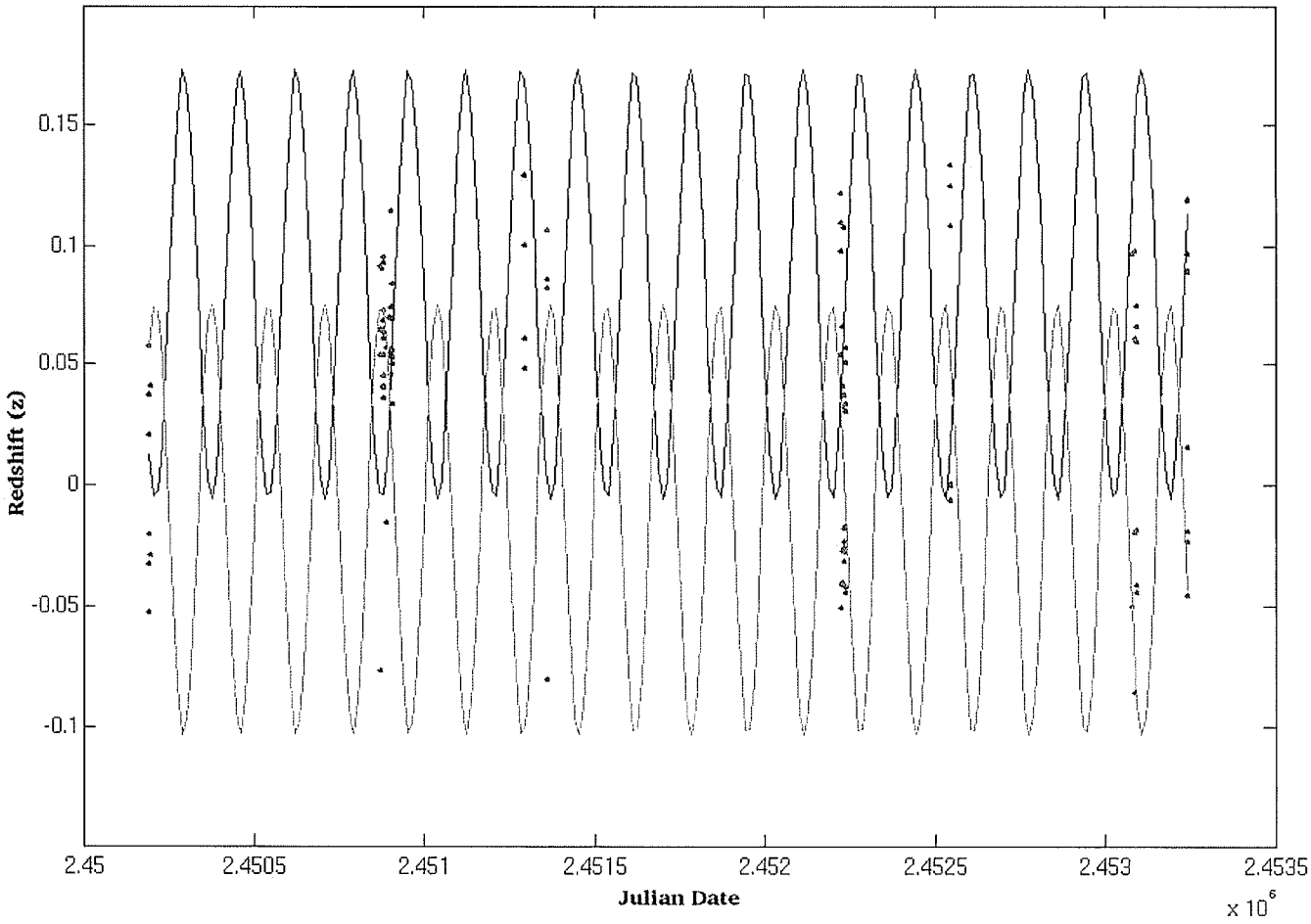

Figure 5.15: The *RXTE* data presented has been best fit by the theoretical redshift curve (Equation 5.1). The green and blue points correspond to the pink and blue points, respectively, in Figures 5.12 - 5.14. Both P_p and $t_{0,p}$ were allowed to vary. All other parameters have values as in Table 2.1.

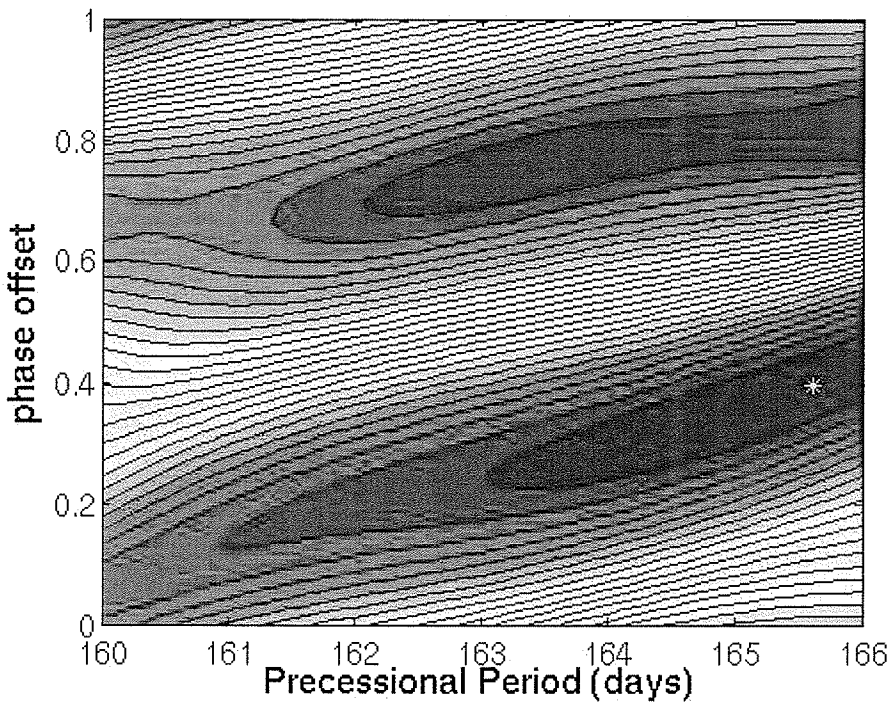

Figure 5.16: The χ^2 contours for the fit seen in Figure 5.15. Blue and red indicates minimum and maximum values for χ^2, respectively. The green star marks the point of the minimum value of χ^2 in this range, and therefore indicates the best fit values for precessional phase offset (~ 0.4; i.e. ψ has this value instead of 0 at the initial epoch noted in Table 2.1) and precessional period (~ 165.5 days).

There are also two other explanations for why the observed redshifts do not always agree with theoretical predictions. It is possible that the line identifications could be incorrect, which would affect the fit to the theoretical curves. Also, data from the 40146 data set have large uncertainties, which could be causing the observed redshifts to deviate from the model near JD 2,451,300.

5.4 Discussion

The archived *RXTE* observations used in this analysis spans over eight years, covering the full range of binary phase and all precessional phases except from ψ ~0.1-0.4 (maximum separation of the lines occurs at $\psi \sim 0$). SS 433 is known to be a moderately bright X-ray source in the 2-10 keV energy range, with $L_x \sim 5 - 50 \times 10^{34}\ D_3^2$ erg/s (Marshall, Canizares & Schulz, 2002). The range of high X-ray luminosity is derived with the *RXTE* data to be (0.93-16)$\times 10^{35}\ D_3^2$ erg/s. Comparing this to the kinetic luminosity of the jet, $L_J \sim 10^{39-40}$ erg/s (Margon, 1984; Brinkmann, Kotani & Kawai, 2005), it is found that ~0.001-0.1% is due to X-rays.

The spectra are fit with either the PL+2G or B+2G models (and in some cases the PL+G and B+G models). When these best fit models occur seems to depend on both the orientation of the jets (i.e. ψ) and on radio events. The emission is likely associated with non-thermal (synchrotron) radiation near $\psi \sim 0.5$, and thermal (bremsstrahlung) radiation otherwise. This is to be expected because the particle interactions will be of higher energy when looking further into a jet. However, at $\psi \sim 0$ or 1, the determination of the best fit model is inconclusive, and more in depth studies need to be carried out in order to explain this behavior. Radio flares appear to switch the spectrum from that which is anticipated, explaining the observations that do not follow the typical best fit model pattern (Figure 5.7).

These results can be linked with those presented in the *INTEGRAL* paper by Cherepashchuk et al. (2003), where SS 433 was observed in March, April and May, 2003. This corresponds to precessional phases of $\psi = 0.72$-0.94 and binary phases of

$\phi = 0.31$-0.97. According to the *RXTE* results, the spectra should be modeled by a power-law near the end of these observations (when $\psi \sim 0$), which is indeed the case. They also derive the hard X-ray luminosity to be $0.74{\times}10^{35}\ D_3^2$ erg/s (25-50 keV) and $1.9{\times}10^{35}\ D_3^2$ erg/s (50-100 keV), which are close to the derived luminosity range from the *RXTE* observations.

The best fit model does not seem to depend on ϕ, but the behavior of spectral parameters do: the temperature (kT), photon index (Γ), and total unabsorbed flux all behave as expected when correlated with the binary phase. The temperature and total unabsorbed are at a minimum near $\phi \sim 0$, when the compact object is being eclipsed the companion star (inferior conjunction), while the photon index is at a maximum at this binary phase.

The addition of *HEXTE* data above the *PCA* energy range helps with both constraining the model parameters and allows for easier discrimination between the B+2G and PL+2G models. The useful energy range for each spectra is a function of the binary phase, as well as the duration of the observation and perhaps the precessional phase (there are not enough observations at $\psi \sim 0.5$ to confirm this).

Correlating the X-ray data to radio activity, it is seen that kT, Γ and the unabsorbed flux all behave as predicted for microquasars in the 60058 data set only. The data in the 90401 data set behave in a similar manner, except that the flux increases prior to the flare, which is not expected. However, this could be due to the orientation of the system in which the compact object is fully visible and the eastern jet is pointing toward the observer. Both of these situations increase the hard X-ray flux, and could in fact cancel out the effect from the radio flare. No conclusions could be made about the behavior in the 40146 data set.

The theoretical redshift curves for both jets are calculated, and the observational redshifts are superimposed on these curves to test the kinematic model. In some cases, the model is in good agreement with the observations. By fitting the redshift curves to the *RXTE* data, it is found that the best fit values for the precessional phase should be ~ 0.4 at the initial precessional epoch, and the precessional period is ~ 165.5 days. The deviations could be due to the imperfect 162.15 day precessional clock, incorrect line identifications, or to the large uncertainties of the spectral parameters in some observations.

Chapter 6

Conclusions

6.1 Summary

In this thesis the Galactic binary system SS 433 and the surrounding nebula, W50, are studied with the *RXTE* and *Chandra* astronomical satellites. The *Chandra* observation of the western lobe of W50 is the highest resolution image of this region to date, and allows for a spatial resolution of the emission. It is found that it is modeled best by a power-law model, indicating that the emission is non-thermal (synchrotron) in nature. The derived values of N_H, equipartition magnetic field, synchrotron electron energies and lifetimes agree with those derived previously with *ROSAT* and *ASCA*.

The X-ray emission is correlated with that of both infrared and radio in order to study the interaction between the western jet of SS 433 and the ambient medium. It is found that the infrared emission is not correlated with the peak of X-ray emission. This, in addition to the high value of N_H derived for the IRknot2 region in the *Chandra* field, suggests that the infrared emission is not originating from W50.

The total synchrotron electron energy is found in X-rays to be $\sim 2.5 \times 10^{45} - 3.5 \times 10^{46}$ ergs, which is in good agreement with the energy found from radio observations. The corkscrew pattern seen in both the radio and X-ray images provides strong support to the hypothesis that the relativistic jets from SS 433 are causing the morphology of the W50 nebula.

The *RXTE* study of the SS 433 binary system is the first of its kind in that it encompasses data from multiple observations spanning over eight years, covers all precessional phases except $\psi \sim$ 0.1-0.4, and includes the addition of data from the *HEXTE* instrument. The hard X-ray luminosity is found to be $\sim (1-16) \times 10^{35}\ D_3^2$ erg/s, which suggests the total X-ray luminosity is ~0.001-0.1% of the total kinetic luminosity of the jets ($L_J \sim 10^{39-40}$ erg/s).

The spectra are best fit by either a bremsstrahlung or power-law model with two Gaussian lines centered at ~7 keV. The best fit model of each observation seems to depend on the orientation of the jets: the spectra are modeled by a power-law when $\psi \sim 0.5$, and by thermal bremsstrahlung otherwise. It also depends on radio flares, switching from the expected best fit model in a given precessional phase range. Near $\psi \sim 0$ or 1, the results are inconclusive, and additional model fits are being carried out in order to investigate this (paper in preparation).

The addition of the *HEXTE* data allows for a better discrimination between the power-law and bremsstrahlung models, and also increases the accuracy of the model parameters. It proves to be an important instrument for spectral analysis between the *Chandra* X-ray Observatory and *INTEGRAL*.

The temperature (kT), photon index (Γ) and total unabsorbed flux are correlated as predicted with the binary phase. Both kT and unabsorbed flux increase up to a maximum near $\phi \sim 0.5$, and are at a minimum during the primary eclipse of the compact object, while Γ is oppositely correlated. The correlations of the spectral parameters with radio activity are not always as expected for microquasars. There is evidence that the radio flares cause the spectra to switch from bremsstrahlung to power-law (or vice versa in one instance).

In some cases, the kinematic model agrees with the observed redshifts. Deviations could be due to the imperfect 162.15 day precessional clock, incorrect identification of the lines, or to the large uncertainties of the spectral parameters in some observations.

The *Chandra* and *RXTE* study of the W50 nebula and X-ray binary system, SS 433, reveals interesting properties of this system. The *Chandra* study gives further evidence that the SS 433 jets are interacting with W50, causing non-thermal emission at the X-ray lobes. By understanding the properties of this interaction, it allows for predictions of the interactions of other microquasars and AGNs with their surrounding medium. The *RXTE* study indicates that perhaps not all microquasars behave as expected, or that there is an evolution of these objects through various stages. It also gives the first derived value for the hard X-ray luminosity from SS 433, which can be compared to other microquasars and AGNs, and could lead to a classification scheme of these objects.

6.2 Looking to the Future

In this thesis the emission mechanisms for both the western lobe of W50 and SS 433 were constrained, the interaction between the western jet of SS 433 and the surrounding medium was confirmed, and the spectral parameters of SS 433 were correlated with the binary phase as well as the radio activity. It was also found that the addition of *HEXTE* data improved the constraints on spectral parameters, as well as the best fit model, proving the usefulness of this instrument.

We are still far from understanding the intricate details of the SS 433/W50 system. New observations are needed to constrain the numerous parameters of the

binary system and to examine in more detail the interactions of the jets and ambient medium as well as between the W50 nebula and the surrounding ISM. The question of the masses of both stars, the distance to the system, as well as the jet parameters still remain unanswered.

Interesting future observations directly tied to the results in this thesis would be: a) an *RXTE* observation between $\psi = 0.9$-0.4 to study the correlations of the best fit models with jet orientation, b) simultaneous X-ray and radio observations during flaring activity to allow for a more accurate correlation between X-ray emission and radio events, c) *Chandra* observations of other areas of the W50 nebula (northern and eastern parts) to permit mapping of the nature of the emission, and d) additional multi-wavelength campaigns (i.e. simultaneous observations in X-ray, infrared, optical and radio) to compare with other microquasars. Studies such as these would further our understanding of the SS 433 system, as well as similar astronomical objects, such as other microquasars and their giant counterparts, AGNs.

Appendix A

X-ray Emission Mechanisms

There are three major physical processes that produce X-rays that are important to this thesis. Each has a unique spectral signature, and thus gives an indication of the nature of the source emission. The following information was obtained from Carroll & Ostlie (1996), Charles & Seward (1995), Lang (1974) and Longair (1992).

A.1 Thermal Emission

Thermal emission occurs when a gas is hot and has low enough density that it is classified as thin, and is transparent to its own radiation. At temperatures above 10^5 K, atoms are ionized. The thermal energy shared by these particles is transfered through collisions. When an electron passes close to a positive ion, the strong electric forces cause its trajectory to change. This accelerates the electron, thus causing it to emit radiation, known as bremsstrahlung (i.e. breaking radiation) or free-free radiation (see Figure A.1).

Electrons in thermal equilibrium have a well determined Maxwellian velocity distribution, and the radiation from such collisions is a continuum with a characteristic shape determined only by the temperature. The higher the temperature, the faster the motion of the electrons and the higher the energy of the photons in the bremsstrahlung radiation. This is demonstrated in Figure A.2. For temperatures $>$ 1 million degrees, photons are predominantly X-rays. Thus, a measurement of the

spectrum can determine the temperature of the gas.

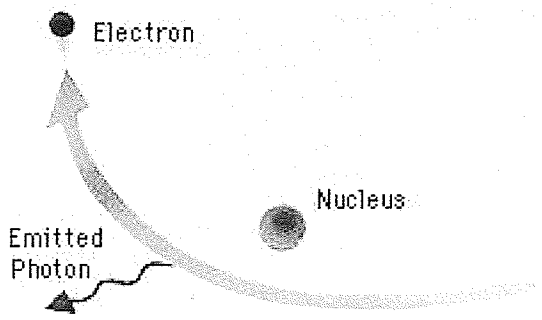

Figure A.1: A diagram showing bremsstrahlung radiation (available from http://imagine.gsfc.nasa.gov/docs/science/how_l2/xray_generation_el.html).

The thermal bremsstrahlung spectrum falls off exponentially at high energies, and is characterized by the temperature, T. The shape of the spectrum is given by a total continuum emission per unit frequency, volume and time as

$$P_\nu^{ff} = \frac{2^5 \pi e^6}{3mc^3} \left(\frac{2\pi}{3mk}\right)^{1/2} T^{-1/2} Z^2 n_e n_i e^{-h\nu/kT} \bar{g}_{ff}(\nu, T) \qquad \text{(A.1)}$$

(Lang, 1974) where T is the plasma temperature, k is Boltzmann's constant, Z is the charge of positive ions, n_e is the electron density, n_i is the positive ion density, m is the electron mass, and $\bar{g}_{ff}(\nu, T)$ is the velocity-averaged Gaunt factor.

In a hot gas, X-ray line emission becomes an important radiation source. Elements heavier than hydrogen are not completely ionized except at very high temperatures. When an electron collides with an atom, the atom will go into an excited state (from the energy transfer). It will then emit radiation to return to its ground state. This radiation appears as spectral lines with energies determined by the radiating ion species.

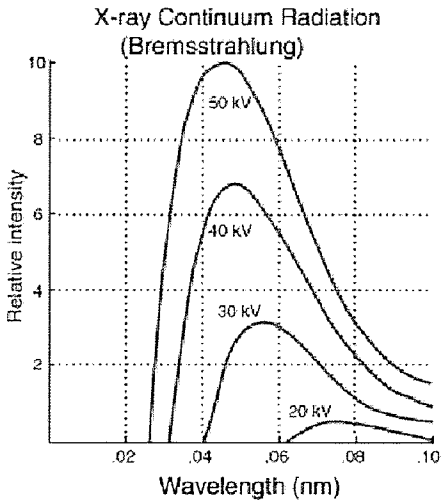

Figure A.2: A plot of the thermal bremsstrahlung X-ray continuum. As the temperature increases, the peak intensity increases but the peak wavelength decreases (available from http://hyperphysics.phy-astr.gsu.edu/hbase/quantum/xrayc.html).

Radiation from a thermal gas is therefore a blend of thermal bremsstrahlung (continuum) and line emission. Table A.1 summarizes the radiation as a function of temperature for a gas of cosmic composition (information from Charles & Seward (1995)).

Table A.1: Type of thermal emission as a function of temperature for a cosmic gas.

Temperature (K)	Radiation
$< 10^6$	most of the energy is radiated as UV lines
$= 2\times10^6$	1/2 the energy is radiated as soft X-rays (energy <0.3 keV)
$= 1\times10^7$	all energy radiated as X-rays, 1/2 by line emission, 1/2 by bremsstrahlung
$= 5\times10^7$	almost all energy is radiated in the X-ray continuum

A.2 Synchrotron Radiation

A fast electron traversing a region containing a magnetic field will change direction because the field exerts a force perpendicular to the direction of motion. The velocity vector changes, thus the electron is accelerating and consequently emits radiation. The frequency of the radiation depends on the electron energy, the magnetic field strength, and the direction of motion relative to the field.

In typical astronomical settings, the magnetic field can be somewhat aligned but particle velocities are expected to be isotropic. So, the observed spectrum only depends on the magnetic field strength and the energy spectrum of the electrons. The usual spectrum for the electrons is a power-law, and thus the resulting spectrum from synchrotron radiation is also a power-law. Also, if a magnetic field is aligned, the radiation will be polarized, and observed polarization usually indicates synchrotron radiation. The form of the power-law spectrum is

$$P_\nu = \frac{2}{3} c \sigma_T n_o \frac{U_B}{\nu_L} \left(\frac{\nu}{\nu_L} \right)^{-(\Gamma-1)/2} \tag{A.2}$$

(Lang, 1974) where σ_T is the Thomson cross section, U_B is the energy density of the magnetic field, n_o is the density of the ISM and ν_L is the non-relativistic Lamor frequency. A power law electron energy distribution with photon index, Γ, will produce a power law spectrum with spectral index of $-(\Gamma - 1)/2$. The power-law spectrum is shown in Figure A.3.

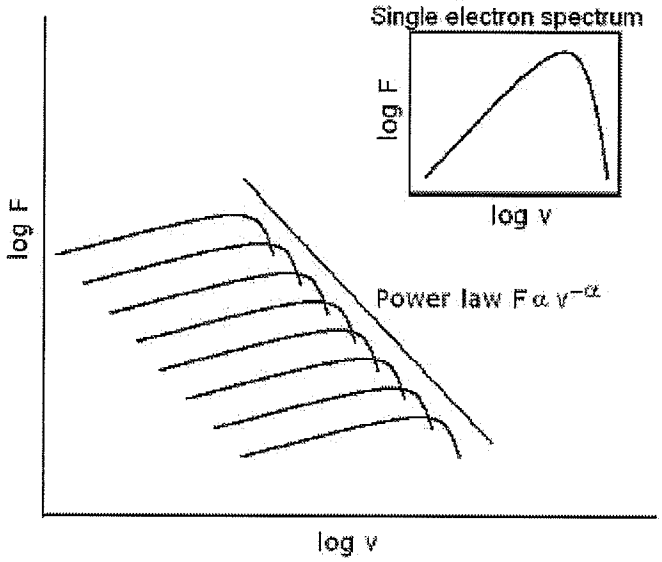

Figure A.3: A plot of the power-law spectrum of synchrotron radiation, shown as the sum of radiation produced by individual electrons. Inset: the spectrum of a single electron (adapted from Carroll & Ostlie (1996)).

A.3 Bremsstrahlung Versus Power-Law Model Fits

In the energy range of the *RXTE* observations, it is not easy to distinguish between the B+2G and PL+2G model fits (i.e. Figure 5.1). The important thing to note is that power-law models have tails that extend up to large energies, whereas the bremsstrahlung model will fall off faster (i.e. at lower energies). Thus, the non-thermal model is flatter (harder) in the spectra. This can be seen in Figures A.4 and A.5.

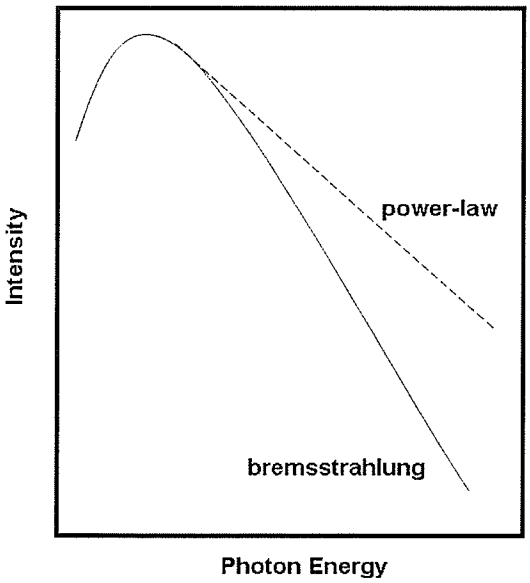

Figure A.4: A comparison of the curves produced by power-law and bremsstrahlung models. Notice how the tails drop off at different rates at high energies.

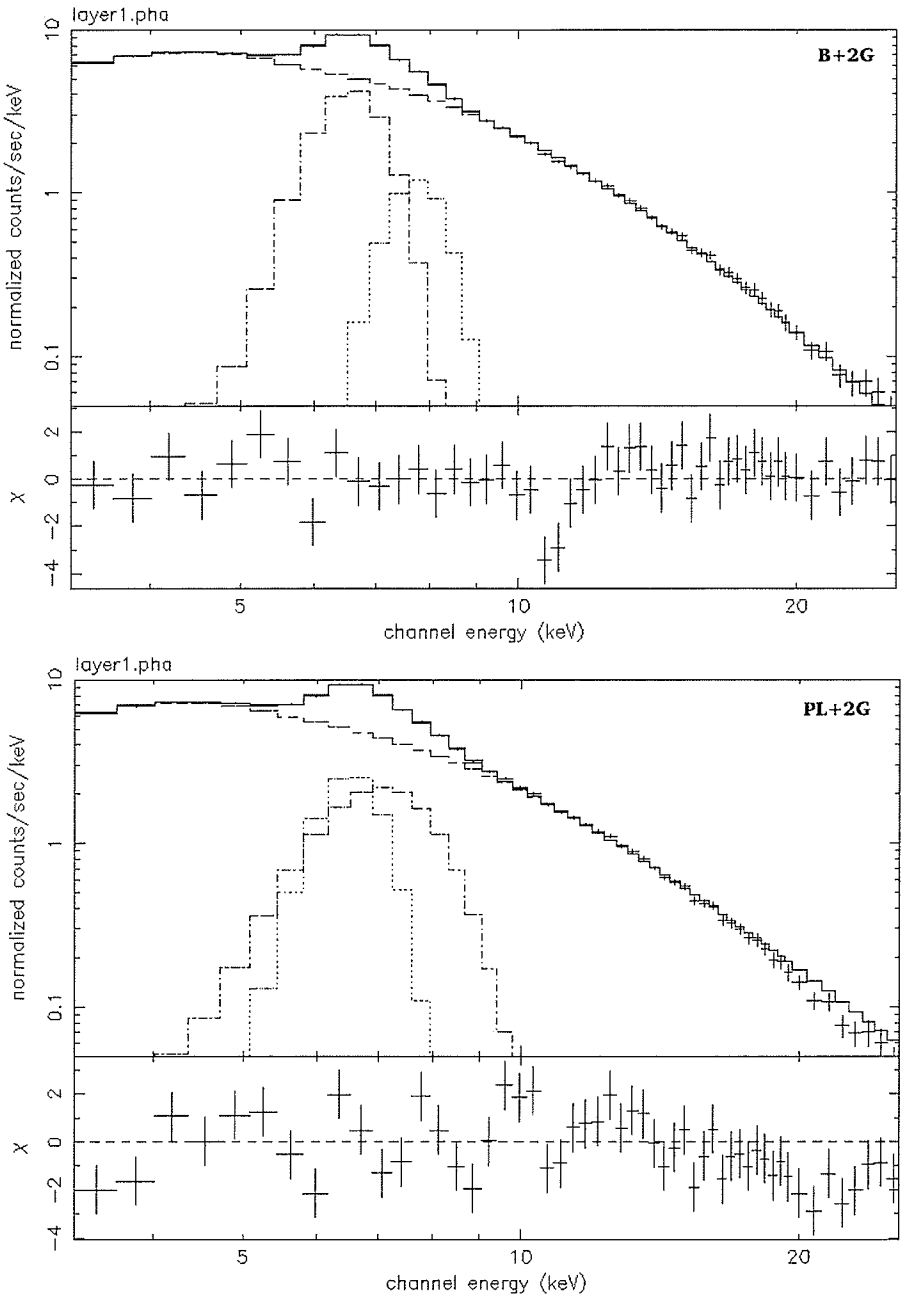

Figure A.5: Example B+2G and PL+2G model fits for the 20102-01-02-00 observation. Data are crosses and the solid line is the fitted model. The energy range is 3-26 keV, $\phi = 0.76$ and $\psi = 0.378$. **Top:** The B+2G model with reduced $\chi^2 = 1.21$. **Bottom:** The PL+2G model with reduced $\chi^2 = 2.23$. It is observed that the PL+2G has a harder (flatter) slope, and does not fit the data as well as the B+2G at higher energies.

A.4 Blackbody Radiation

It is well known that black surfaces completely absorb any radiation incident upon it. However, it is a law of nature that any surface must not only absorb but also emit radiation. This radiation is isotropic under thermodynamic equilibrium. The spectrum radiated is a well-defined continuum with peak emission at an energy dependent only on the temperature, T. The higher the temperature, the more energetic the photons. The form of the spectrum is given by

$$I(E,T) = \frac{2h\nu^3}{c^2}\frac{1}{e^{h\nu/kT}-1} \equiv B_\nu(T) \tag{A.3}$$

(Charles & Seward, 1995) where k is Boltzmann's constant, h is Planck's constant and c is the speed of light. This equation is known as Planck's radiation law.

Stars radiate as approximate blackbodies with temperatures ranging from 2,500 K to 40,000 K. Although the spectrum is strongly modified by the stellar atmosphere, it retains an overall gross shape imposed by the blackbody process. Figure A.6 shows example spectra for stars with temperatures ranging from 4,000-7,000 K. The wavelength corresponding to the radiation intensity peak will displace toward shorter wavelengths as the temperature increases, according to the relationship

$$\lambda_{max} = 0.28978/T \quad (\text{cm/K}). \tag{A.4}$$

This is known as Wien's displacement law (Carroll & Ostlie, 1996). A newly formed neutron star is expected to have a hot surface ($> 1 \times 10^6$ K), and will emit blackbody radiation with photons in X-ray frequencies.

The total radiation flux (erg·cm^2/s) can be obtained by summing the flux values for all wavelengths. According to the Stefan-Boltzmann law, the total radiation flux

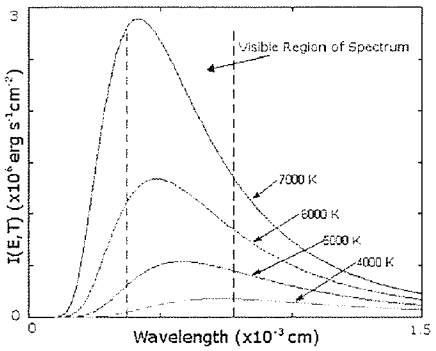

Figure A.6: A plot of blackbody spectra for stars with temperatures ranging from 4,000-7,000 K. Notice how, as the temperature increases, the peak intensity increases and the wavelength at which this occurs decreases.

is proportional to the fourth power of the temperature:

$$\pi F = \pi B = \sigma T^4 \tag{A.5}$$

(Carroll & Ostlie, 1996) where σ is the Stefan-Boltzmann constant.

Appendix B

RXTE Lightcurves

The following show the lightcurves for each *RXTE* observation set. Some sets (40146 and 90401) have been broken down into two or more sub-sets because of large breaks in the observation times. It should be noted that all the *RXTE* observations are used to produce these lightcurves, and not just the 78 observations with good data. Also, the REX script, which was used for the *PCA* data reduction (see section 3.2.3) only chooses:

- the top layer *PCA* data
- PCUs 0, 1 and 2 (since PCUs 3 and 4 go on and off regularly)
- the energy range of ~1-10 keV
- and times when:
  - the Earth elevation angle is greater than 10^o
  - the pointing offset is less than 0.02^o
  - the time since the peak of the last South Atlantic Anomaly (SAA - an effect of the Van Allen Belt) passage is greater than 30 minutes
  - the electron contamination is less than 0.1

See http://rxte.gsfc.nasa.gov/docs/xte/recipes/rex.html for details. Each lightcurve is binned by 16 s.

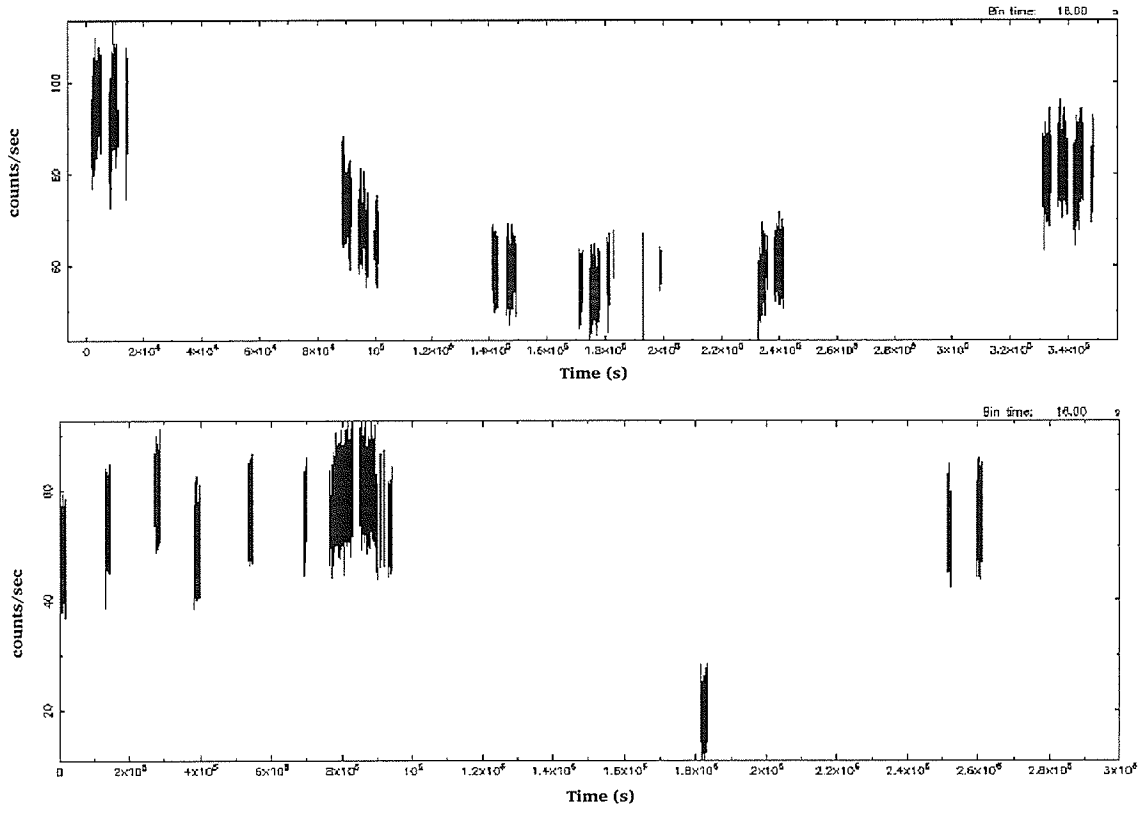

Figure B.1: **Top:** 10127 lightcurve (2,450,191.6 JD - 2,450,195.4 JD). **Bottom:** 20102 lightcurve (2,450,869.3 JD - 2,450,899.3 JD).

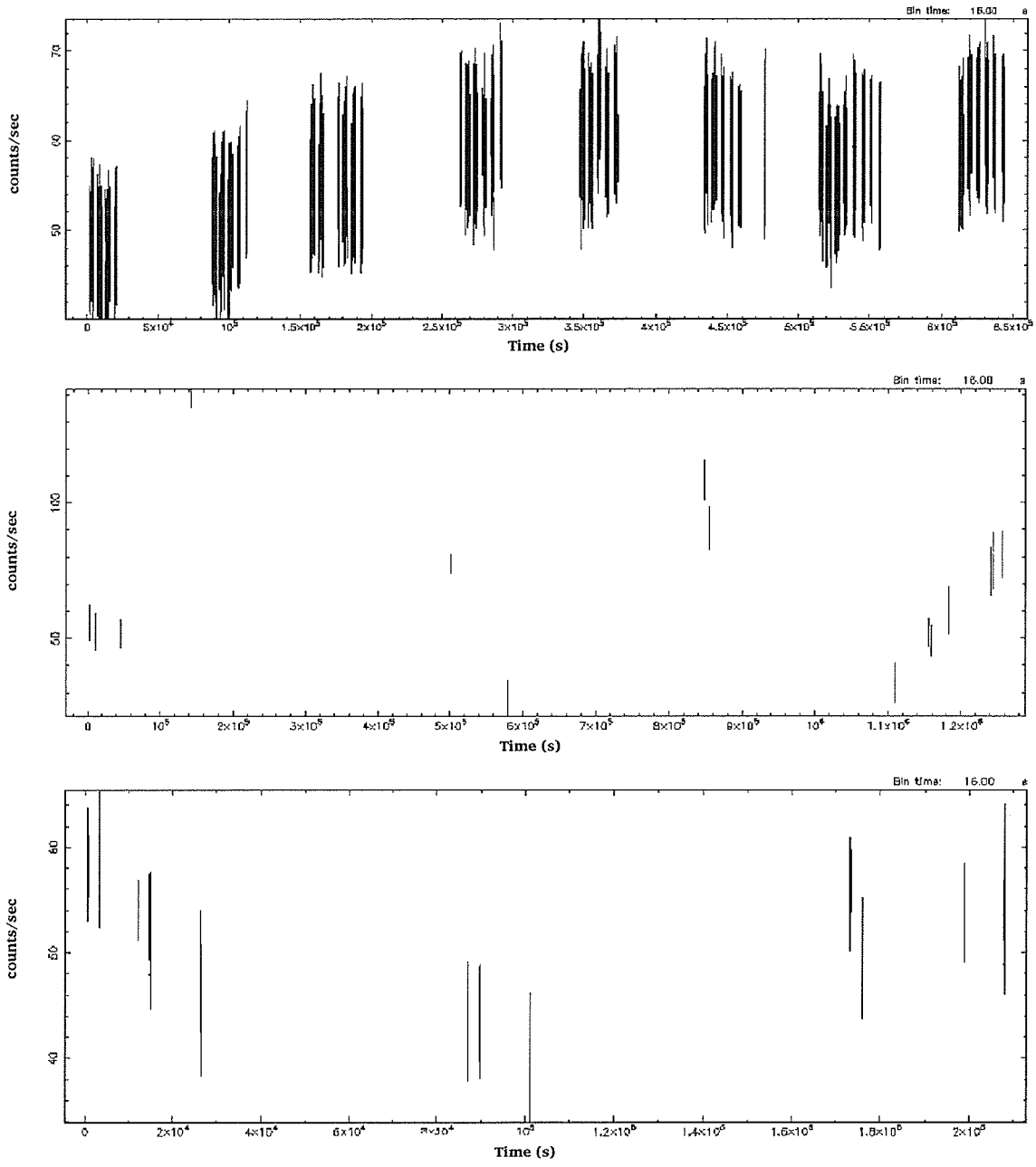

Figure B.2: **Top:** 30273 lightcurve (2,450,900.2 JD - 2,450,907.6 JD). **Middle:** 40146a lightcurve (2,451,292.7 JD - 2,451,307.3 JD). **Bottom:** 40146b lightcurve (2,451,307.3 JD - 2,451,359.5 JD).

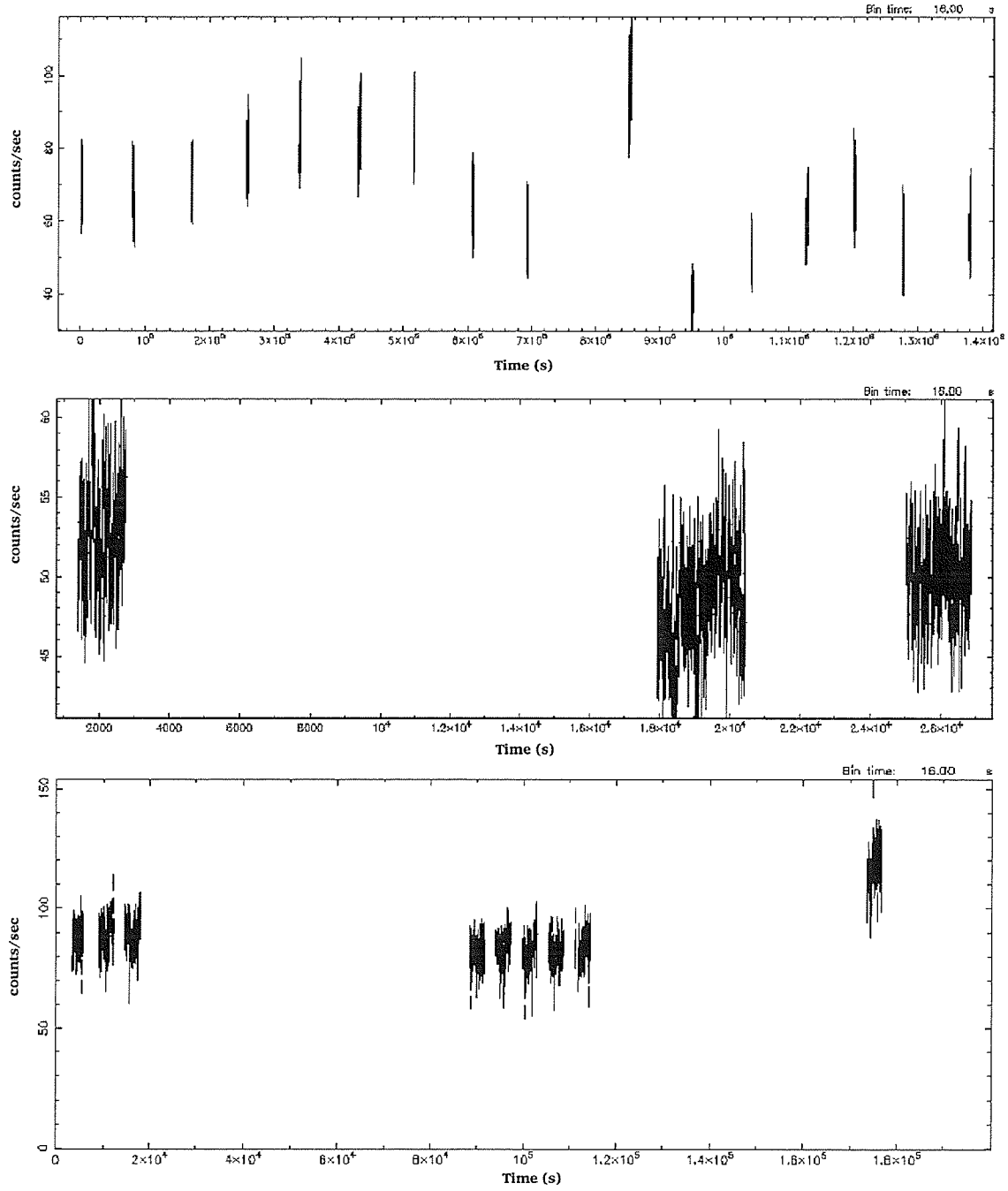

Figure B.3: **Top:** 60058 lightcurve (2,452,222.8 JD - 2,452,238.7 JD). **Middle:** 70416 lightcurve (2,452,545.0 JD - 2,452,545.2 JD). **Bottom:** 90058a lightcurve (2,453,077.3 JD - 2,453,079.3 JD).

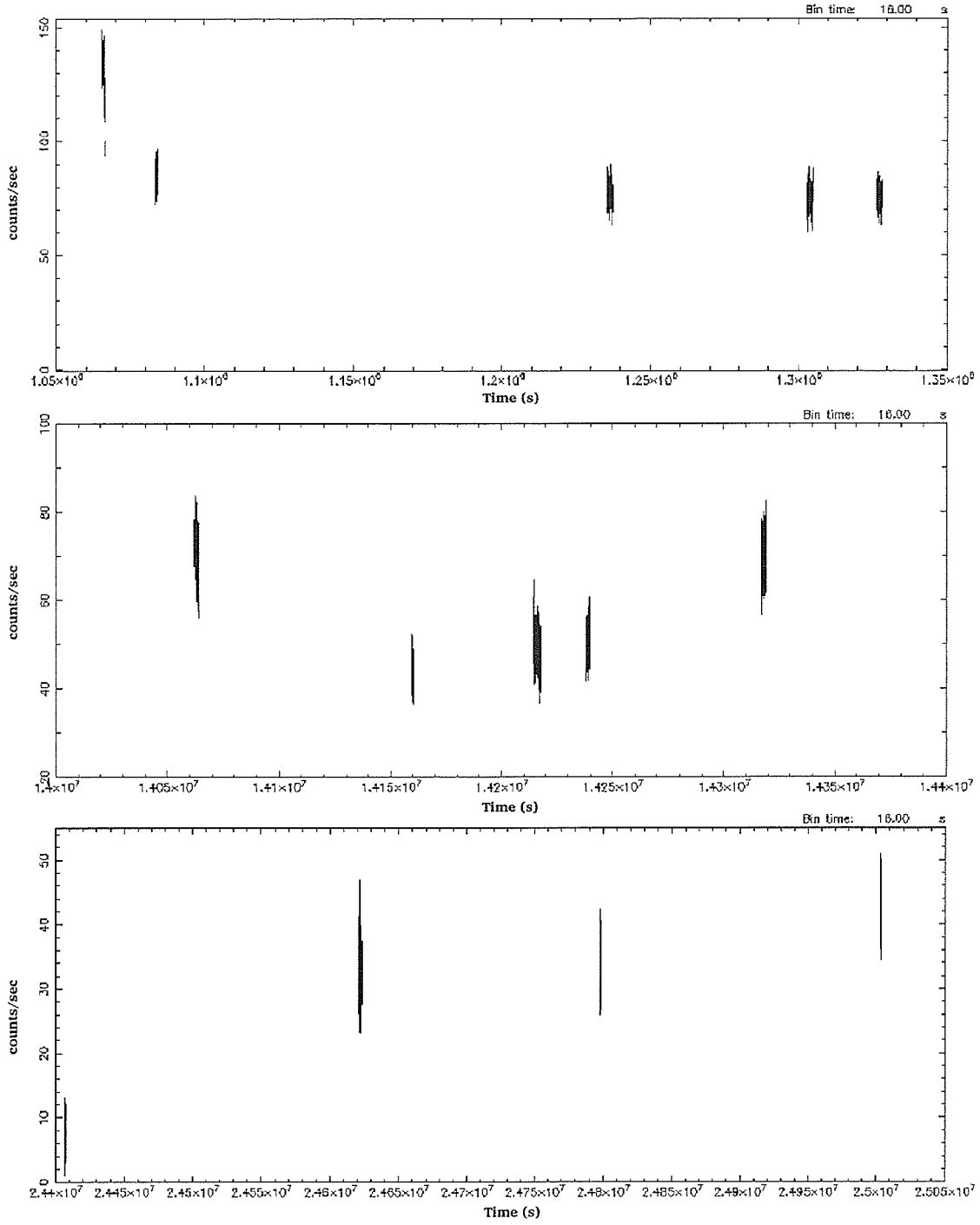

Figure B.4: **Top:** 90401b lightcurve (2,453,089.6 JD - 2,453,092.6 JD). **Middle:** 90401c lightcurve (2,453,240.0 JD - 2,453,243.0 JD). **Bottom:** 90058d lightcurve (2,453,359.7 JD - 2,453,366.6 JD).

Appendix C

RXTE Scripts

The following are the scripts used for the reduction of the *HEXTE* data. For more details on each of the required input parameters, see http://heasarc.gsfc.nasa.gov/docs /xte/recipes/hexte.html. The REX script was used for the *PCA* data, and details can be found at http://heasarc.gsfc.nasa.gov/docs/xte/recipes/rex.html. The emphasized text are the annotations to inform the user of what each tool does.

Script #1

#Written by Alyssa Moldowan, April 1st, 2004; script for data reduction of HEXTE Science Event (SE) data; #Step 1 of HEXTE reduction

#user sets $file (filename), $stat (FH53 or FH59 file) and $jj (cluster a (0) or b (1)) before running

```
#!/bin/csh
```

#separate background and source data

```
hxtback -b -i $file
```

#extract spectrum (saextrct) or lightcurve (seextrct)

```
for {set ii 0} {$ii <=1} {incr ii} {
if ($ii==0) {
set type src
} elseif ($ii==1) {
set type bkg
}
seextrct infile=${file}_${type} gtiorfile=APPLY gtiandfile=- outroot=${file}_${type} timecol=TIME
columns=Event binsz=16 printmode=BOTH lcmode=RATE spmode=SUM timemin=INDEF
```

```
timemax=INDEF timeint=INDEF chmin=INDEF chmax=INDEF chint=INDEF chbin=INDEF

}

#calculated the deadtime for cluster A and B

for {set ii 0} {$ii <=1} {incr ii} {

if ($ii==0) {

set type src

if ($jj==0) {

hxtdead

calvalf=/usr/local/alocal/ciao_2.30/CALDB/data/xte/hexte/bcf/deadtime/hxtdead_200002_pwa.fits

engvalf=$stat eventarcf=${file}_${type} phalcf=${file}_${type}.pha

hxtdead

calvalf=/usr/local/alocal/ciao_2.30/CALDB/data/xte/hexte/bcf/deadtime/hxtdead_200002_pwa.fits

engvalf=$stat eventarcf=${file}_${type} phalcf=${file}_${type}.lc

} elseif ($jj==1) {

hxtdead detector=013

calvalf=/usr/local/alocal/ciao_2.30/CALDB/data/xte/hexte/bcf/deadtime/hxtdead_200002_pwb.fits

engvalf=$stat eventarcf=${file}_${type} phalcf=${file}_${type}.pha

hxtdead detector=013

calvalf=/usr/local/alocal/ciao_2.30/CALDB/data/xte/hexte/bcf/deadtime/hxtdead_200002_pwb.fits

engvalf=$stat eventarcf=${file}_${type} phalcf=${file}_${type}.lc

}

} elseif ($ii==1) {

set type bkg

if ($jj==0) {
```

hxtdead

calvalf=/usr/local/alocal/ciao_2.30/CALDB/data/xte/hexte/bcf/deadtime/hxtdead_200002_pwa.fits

engvalf=$stat eventarcf=${file}_${type} phalcf=${file}_${type}.pha

hxtdead

calvalf=/usr/local/alocal/ciao_2.30/CALDB/data/xte/hexte/bcf/deadtime/hxtdead_200002_pwa.fits

engvalf=$stat eventarcf=${file}_${type} phalcf=${file}_${type}.lc

} elseif ($jj==1) {

hxtdead detector=013

calvalf=/usr/local/alocal/ciao_2.30/CALDB/data/xte/hexte/bcf/deadtime/hxtdead_200002_pwb.fits

engvalf=$stat eventarcf=${file}_${type} phalcf=${file}_${type}.pha

hxtdead detector=013

calvalf=/usr/local/alocal/ciao_2.30/CALDB/data/xte/hexte/bcf/deadtime/hxtdead_200002_pwb.fits

engvalf=$stat eventarcf=${file}_${type} phalcf=${file}_${type}.lc

} } }

Script #2

#!/bin/csh -f

#Written by Alyssa Moldowan, April 1st, 2004; #Step 2 of HEXTE reduction; #script for combining and creating net spectra and forms .rmfs

#user sets $jj (clustera (FS50 data) or clusterb (FS56 data))

#If there is only one FS50/FS56 file, then the summing of the .pha files does not take place, and the individual file names are used.

if ($jj==0) {

set cl FS50

} elseif ($jj==1) {

```
set cl FS56

}

#summing .pha files if there are more than one

for {set ii 0} {$ii <=1} {incr ii} {

if ($ii==0) {

set type src

} elseif ($ii==1) {

set type bkg

}

sumpha filelist=@${cl}_list_${type} outfile=${cl}_sum_${type}.pha clobber=yes }

#form appropriate rmf for background file

for {set ii 0} {$ii <=1} {incr ii} {

if ($ii==0) {

set type src

if ($jj==0) {

fparkey add=yes PWA ${cl}_sum_${type}.pha DETNAM

rddescr phafil=${cl}_sum_${type}.pha chanfil=${cl}_sum_${type}.bins

rbnrmf binfile=${cl}_sum_${type}.bins infile=../../../hexte_97mar20c_pwa.rmf

outfile=${cl}_sum_${type}.rmf

fparkey add=yes ${cl}_sum_${type}.rmf ${cl}_sum_${type}.pha RESPFILE

fparkey add=yes ${cl}_sum_bkg.pha ${cl}_sum_${type}.pha BACKFILE

} elseif ($jj==1) {

fparkey add=yes PWB013 ${cl}_sum_${type}.pha DETNAM

rddescr phafil=${cl}_sum_${type}.pha chanfil=${cl}_sum_${type}.bins
```

```
rbnrmf binfile=${cl}_sum_${type}.bins infile=../../../hexte_97mar20c_pwb013.rmf
outfile=${cl}_sum_${type}.rmf
fparkey add=yes ${cl}_sum_${type}.rmf ${cl}_sum_${type}.pha RESPFILE
fparkey add=yes ${cl}_sum_bkg.pha ${cl}_sum_${type}.pha BACKFILE
}
} elseif ($ii==1) {
set type bkg
if ($jj==0) {
fparkey add=yes PWA ${cl}_sum_${type}.pha DETNAM
rddescr phafil=${cl}_sum_${type}.pha chanfil=${cl}_sum_${type}.bins
rbnrmf binfile=${cl}_sum_${type}.bins infile=../../../hexte_97mar20c_pwa.rmf
outfile=${cl}_sum_${type}.rmf
fparkey add=yes ${cl}_sum_${type}.rmf ${cl}_sum_${type}.pha RESPFILE
} elseif ($jj==1) {
fparkey add=yes PWB013 ${cl}_sum_${type}.pha DETNAM
rddescr phafil=${cl}_sum_${type}.pha chanfil=${cl}_sum_${type}.bins
rbnrmf binfile=${cl}_sum_${type}.bins infile=../../../hexte_97mar20c_pwb013.rmf
outfile=${cl}_sum_${type}.rmf
fparkey add=yes ${cl}_sum_${type}.rmf ${cl}_sum_${type}.pha RESPFILE
} } }
```

Appendix D

Abbreviations

The following is a list of abbreviations used throughout this thesis.

ACIS	Advanced CCD Imaging Spectrometer; detector on *Chandra*
AGNs	Active Galactic Nuclei
ASCA	Advanced Satellite for Cosmology & Astrophysics; X-ray satellite
ASM	All Sky Monitor; detector on *RXTE*
AXAF	Advanced X-ray Astrophysics Facility (*Chandra*); X-ray satellite
AXP	Anomalous X-ray Pulsar
CALDB	Calibration Database; *Chandra* calibration files directory
CCD	Charged Coupled Device
CIAO	*Chandra* Interactive Analysis of Observations
CTI	Charge Transfer Inefficiency
CXB	Cosmic X-ray Background
CXC	*Chandra* X-ray Center
EDS	Experiment Data System; *RXTE* data system
FITS	Flexible Image Transport System
FWHM	Full Width at Half Maximum
GTI	Good Time Interval
HEASARC	High Energy Astrophysics Science Archive Research Center
HEXTE	High Energy X-ray Timing Experiment; detector on *RXTE*
HRC	High-Resolution Camera; detector on *Chandra*
HRMA	High-Resolution Mirror Assembly; *Chandra* mirrors
INTEGRAL	International Gamma-ray Astrophysics Laboratory; gamma-ray satellite
ISM	Interstellar Medium
ISOCAM	Infrared Space Observatory Camera; infrared satellite detector
JD	Julian Date
LOS	Line of Sight
MCP	Micro-Channel Plates
NASA	National Aeronautics & Space Administration
NRAO	National Radio Astronomy Observatory

PCA	Proportional Counter Array; *RXTE* detector
PCU	Proportional Counter Unit
PHA	Pulse Height Amplitude
PI	Pulse Invariant
RATAN-600	Radio Astronomy Telescope of the Academy of Science (Nank)
ROSAT	Röntgen Satellite; X-ray satellite
RXTE	Rossi X-ray Timing Explorer; X-ray satellite
S/N	Signal to Noise ratio
SAA	South Atlantic Anomaly
Σ-D	surface brightness to linear diameter relation
SNR	Supernova Remnant
VF	Very Faint; *Chandra* telemetry format
VLA	Very Large Array; radio telescope
XSPEC	X-ray Spectral fitting package

Appendix E

Glossary of Terms

Active Galactic Nuclei (AGNs): Galactic nuclei that give off much more energy than can be accounted for in terms of stellar content. Quasi-stellar objects (Quasars), are a subset of AGNs and are the most luminous objects in the Universe. They have variabilities on the order of days or months, are supermassive black holes, and often have observable jets and lobes.

Anomalous X-ray Pulsar (AXP): A slowly rotating X-ray pulsar with a period of 5-12 sec. Its X-ray emission can not be accounted for by rotation and is believed to be powered by magnetic field decay.

Cataclysmic Variable: Stellar binary systems that have short periods, and contain white dwarf components with cool M-type secondaries that fill their Roche Lobes (see below).

χ^2 Distribution: The following is from Bevington (1969). The probability distribution $P_x(x^2, \nu)$ for χ^2 is given by

$$P_x(x^2, \nu) = \frac{1}{2^{\nu/2}\Gamma(\nu/2)}(x^2)^{1/2(\nu-2)}e^{-x^2/2}. \tag{E.1}$$

The probability of observing a value of chi-square larger than χ^2 for a random sample of N observations with ν degrees of freedom is the integral of this probability

$$P_\chi(\chi^2, \nu) = \frac{1}{2^{\nu/2}\Gamma(\nu/2)}\int_{\chi^2}^{\infty}(x^2)^{1/2(\nu-2)}e^{-x^2/2}d(x^2). \tag{E.2}$$

Fluorescence: Atoms that do not return to their initial state after emitting a

photon. Since they drop to an interim state, the photon has lower energy that that of the incident photon.

Inferior & Superior Conjunction: When the object in question is between Earth and its companion, and when it is on the far side of the companion from Earth, respectively. For example, in Figure 2.5 of this thesis, when the compact object is eclipsed by the companion star, it is in superior conjunction. When the compact object is in front of the companion, this is known as inferior conjunction.

J2000 Coordinate System: Coordinates corresponding to the position of the north celestial pole on January 1st, 2000, at 12:00pm Terrestrial Time (TT) (equivalent to 2,451,545.0 JD).

Julian Date: A calendar that begins on January 1st, 4713 BC, at 12:00 noon TT.

Lense-Thirring Effect: (otherwise known as dragging of frames) The orbit of a small body orbiting around a rotating, massive one is slightly perturbed by the rotation of the massive body. This results in orbital precession of the X-ray gas near the compact object, and causes peaks in the X-ray emission.

Microquasar: A neutron star or a stellar mass black hole in a binary system ejecting relativistic jets. These objects share many properties with AGNs, such as strong emission from radio to X-ray wavelengths, rapid variabilities in X-rays, and jets. However, evolution in microquasars occur on a much shorter timescale ($\sim 10^5$ times faster).

P Cygni Absorption Lines: Characterized by a broad emission peak with a superimposed blueshifted absorption trough.

Relativistically Deep Potential Well: A gravitational well that is sufficiently deep that the particles need to have relativistic speeds in order to escape.

Roche-Filling Evolved Star: A star in a binary system that is filling its Roche lobe (see Figure E.1), and therefore allowing mass to be accreted by its companion. In the reference frame co-rotating with the center of mass of the binary system, the Roche lobes are surfaces of constant effective gravity (which included the net gravitational effect of the bodies in addition to the centrifugal force). The two Roche lobes meet at the L_1 Lagrange point. There are five Lagrange points in total, where the gravitational forces of the two bodies exactly balance the centrifugal force that would be felt by a small body if it were in the system.

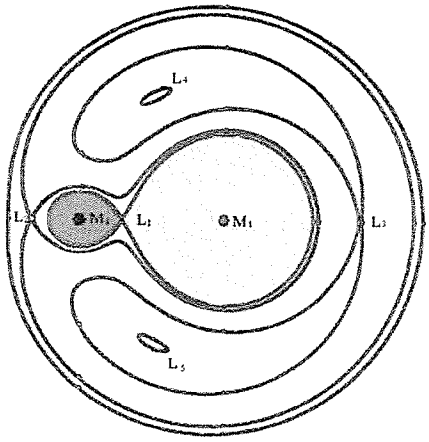

Figure E.1: A depiction of the Roche lobes in a binary stellar system.

Slaved Precession: The accretion disk is forced to align with the precessing spin axis of the normal companion star. The disk, in turn, forces the jets to be normal to the disk plane.

Spectral Index: See Appendix A.

Eddington Limit: The maximum luminosity a star can have and still remain in

hydrostatic equilibrium. This is given by

$$L_{edd} = 1.3 \times 10^{38} \frac{M}{M_{\odot}} \quad \text{(erg/s)}, \tag{E.3}$$

assuming that the opacity is mainly due to electron scattering and that the mass fraction of Hydrogen is 70%. If the star's luminosity exceeds this limit, then mass loss must occur (which is known as super-Eddington).

Supernova Remnant (SNR): The remnant of an exploded star. This is distinguished from an H II region by the relatively flat spectral index and non-thermal radio spectrum. An SNR is expected to have a limb-brightened morphology and to emit thermal X-rays. There are three main evolutionary phases: 1) the free expansion phase which ends when the swept-up mass exceeds the ejected mass, 2) the adiabatic expansion phase which is an energy-conservation phase, and 3) the radiative phase which is a momentum-conservation phase.

Telemetry: Space to ground data stream of measured values.

X-ray Binary System (XRB): A stellar binary system consisting of a normal star and a compact object, and emits strongly in X-ray wavelengths.

Bibliography

Abell, G., & Margon, B., A kinematic model for SS 433. Nature, 279, 701-703, 1979.

Anderson, S., Margon, B., & Grandi, S., Narrow-band photometric periods in SS 433. ApJ, 269, 605-612, 1983.

Band, D., *IRAS* observations of SS 433 and W50. PASP, 99, 1269-1276, 1987.

Begelman, M., Hatchett, S., McKee, C., et al., Beam models for SS 433. ApJ, 238, 722-730, 1980.

Begelman, M., & Cioffi, D., Overpressured cocoons in extragalactic radio sources. ApJ, 345, L21-L24, 1989.

Bevington, P., 1969, Data reduction and error analysis for the physical sciences, published by McGraw-Hill Book Company, USA.

Brinkmann, W., Kotani, T., & Kawai, N., *XMM-Newton* observations of SS 433 I. *EPIC* spectral analysis. A&A, 431, 575-586 (2005).

Carroll, B., & Ostlie, D., 1996, An introduction to modern astrophysics, published by Addison-Wesley Publishing Company, Inc., USA.

Charles, P., & Seward, F., 1995, Exploring the X-ray universe, published by Cambridge University Press, Great Britain.

Cherepashchuk, A., Sunyaev, R., Seifina, E., et al., *INTEGRAL* observations of SS 433, a supercritically accreting microquasar with hard spectrum. A&A, 411, L441-L445, 2003.

Clark, D., Green, A., & Caswell, J., Improved 408 MHz observations of some galactic supernova remnants. AuJPA, 37, 75-86, 1975.

Clark, D., Murdin, P., An unusual emission-line star/X-ray source/radio star, possibly associated with an SNR. Nature, 276, 45-46, 1978.

Crampton, D., Cowley, A., & Hutchings, J., The probable binary nature of SS 433. ApJL, 235, L131-135, 1980.

Dubner, G., Holdaway, M., Goss, M., et al., A high-resolution radio study of the W50-SS 433 system and the surrounding medium. AJ, 116, 1842-1855, 1998.

Durouchoux, P., Sood, R., Oka, T., et al., Jet interaction of SS 433 with the ambient medium. AdSpR, 25, 703-708, 2000.

Elston, R., & Baum, S., High-resolution radio observations of W50, the remnant associated with SS 433. AJ, 94, 1633-1640, 1987.

Fabian, A., & Rees, M., SS 433: a double jet in action? MNRAS, 189, 13-16, 1979.

Geldzahler, B., Pauls, T., & Salter, C., Continuum observations of the supernova remnants W50 and G74.9+1.2 at 2695 MHz. AA, 84, 237-244, 1980.

Gies, D., McSwain, M., Riddle, R., et al., The spectral components of SS 433. ApJ, 566, 1069-1083, 2002.

Goranskii, V., Esipov, V., & Cherepashchuk, A., Optical variability of SS 433 in 1978-1996. Astron. Reports, 42, No. 2, 209-228, 1998.

Green, D.A., 2005, Bulletin of the Astronomical Society of India, 32, in press (Astro-ph/0411083).

Hjellming, R., Johnston, K., An analysis of the proper motions of SS 433 radio jets. ApJ, 246, L141-L145, 1981.

Katz, J., Anderson, S., Margon, B., et al., Nodding motions of accretion rings and disks: a short-term period in SS 433. ApJ, 260, 780-793, 1982.

Königl, A., W50 - A stellar-wind bubble in a three-phase interstellar medium? MNRAS, 205, 471, 1983.

Kotani, T., X-ray observations of a galactic jet system SS 433 with *ASCA*. PhD Thesis, University of Tokyo, 1996.

Kotani, T., Trushkin, S., Denissyuk, E., et al., A massive jet-ejection from SS 433. Astro-ph/0208250, 2002.

Lang, K., 1974, Astrophysical formulae, published by Springer-Verlang, New York.

Liebert, J., Angel, J., Hege, E., et al., The moving emission features in SS 433: evidence requiring a dynamical interpretation. Nature, 279, 384-87, 1979.

Longair, M., 1992, High energy astrophysics, published by Cambridge University Press, Great Britain.

Marshall, F., Swank, J., Boldt, E., et al. X-ray observations of H1908+050 (=SS 433). ApJL, 230, L145-48, 1979.

Marshall, H., Canizares, C., & Schulz, N., The high-resolution X-ray spectrum of SS 433 using the *Chandra HETGS*. ApJ, 564, 941-952, 2002.

Margon, B., Observations of SS 433. ARAA, 22, 507-536, 1984.

Margon, B., Ford, H., Grandi, S., et al. Enormous periodic doppler shifts in SS433. ApJL, 233, L63-68, 1979.

Margon, B., Grandi, S., & Downes, R., The 164 and 13 day periods of SS 433: confirmation of the kinematic model. ApJ, 241, 306-315, 1980.

Martin, P., & Rees, M., A model for SS 433: precessing jets in an ultra-close binary system. MNRAS, 189, 19-22, 1979.

Milgrom, M., On the interpretation of the large variations in the line positions in SS433. AA, 76, L3-6, 1979.

Moldowan, A., Safi-Harb, S., Fuchs, Y., & Dubner, G., A multi-wavelength study of the western lobe of W50 powered by the galactic microquasar SS 433. AdSpR, 35, 1062-1065, 2005.

Raymond, J., & Smith, B., Soft X-ray spectrum of a hot plasma. ApJS, 35, 419-439, 1977.

Ryle, M., Caswell, J., Hine, G., et al., A new class of radio star. Nature, 276, 571-573, 1978.

Safi-Harb, S., An X-ray study of pulsars (PSR's) associated with unusual supernova remnants (SNR's). PhD Thesis, University of Wisconsin, Madison, USA, 1997.

Safi-Harb, S. 2005, High-energy emission from supernova remnants and associated compact objects, BAAA, vol. 47, in press (Eds. P. Cincotta, G. Dubner, et al.).

Safi-Harb, S., & Ögelman, H., *ROSAT* and *ASCA* observations of W50 associated with the peculiar source SS 433. ApJ, 483, 868-881, 1997.

Safi-Harb, S., & Petre, R., *Rossi X-ray Timing Explorer* observations of the eastern lobe of W50 Associated with SS 433. ApJ, 512, 784-792, 1999.

Safi-Harb, S., & Kotani, T., On the galactic microquasar SS433/W50. HEAD Meeting, Albequerque, New Mexico, 2002.

Safi-Harb, S., & Kotani, T., SS 433: Radio/X-ray anti-correlation and fast-time variability. Astro-ph/0210396, 2002.

Seaquist, E., Garrison, R., Gregory, P., et al., Radio and optical observations of SS 433, AJ, 84, 1037-1041, 1979.

Seward, F., Grindlay, J., Seaquist, E., et al., Diffuse X-ray emission from the jets of SS 433. Nature, 287, 806-808, 1980.

Seward, F., Page, C., Turner, M., et al., X-ray sources in the Aquila-Serpens-Scutum region. MNRAS, 175, 39-46, 1976.

Stephenson, C. B. and Sanduleak, N., New H-alpha emission stars in the Milky Way. Astrophysical Journal (Supplement), 33, 459, 1977.

Trushkin, S., Bursov, N., & Nizhelskij, N., The multifrequency monitoring of microquasars. SS 433. Bull. Spec. Astrophys. Obs., 56, 57-90, 2003.

Velusamy, T., & Kundu, M., Observations of intensity and linear polarization in supernova remnants at 11 CM wavelength. AA, 32, 375-390, 1974.

Vermeulen, R., Multi-wavelength studies of SS 433. PhD Thesis, Leiden: Rijksuniversiteit, 1989.

Watson, M., Willingale, R., Grindlay, J. et al., The X-ray lobes of SS 433. ApJ, 273, 688-696, 1983.

Yamauchi, S., Kawai, N., & Aoki, T., A non-thermal X-ray spectrum from the supernova remnant W50. PASJ, 46, L109-L113, 1994.

Zwitter, T., Calvani, M., Bodo, G., et al., SS 433: an up-to-date review. Fund. of Cos. Phys., 13, 309-355, 1989.